PERFORMANCE IMPROVEMENT OF ANODE IN ZINC-AIR BATTERY BASED ON METALLURGY TECHNOLOGY

By
Mr. Chen SHUNHONG

A Thesis Submitted in Partial Fulfillment of the Requirements
for Doctor of Philosophy ENERGY ENGINEERING
Department of MECHANICAL ENGINEERING
Silpakorn University
Academic Year 2025

Performance Improvement of Anode in Zinc-air Battery based on Metallurgy Technology

โดย
Mr.Chen Shunhong

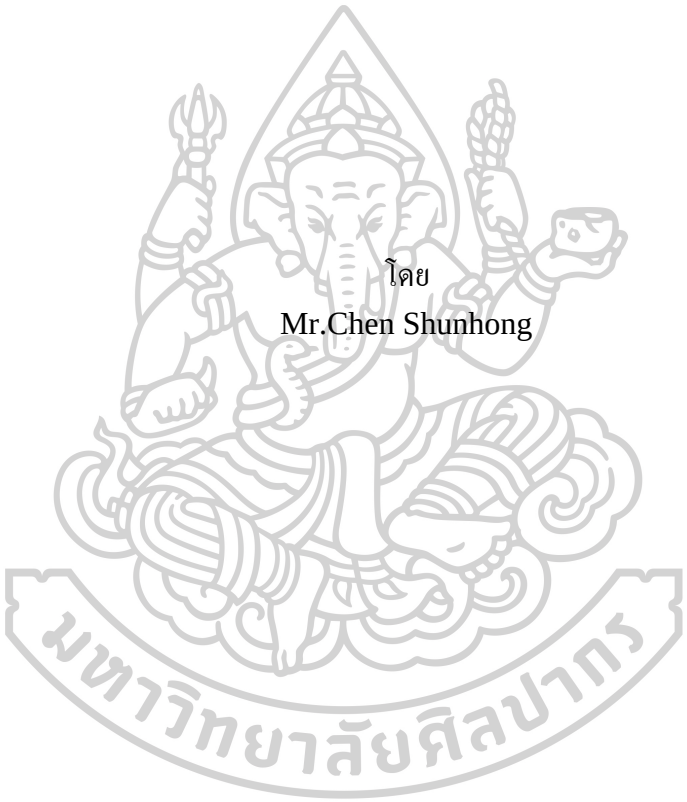

วิทยานิพนธ์นี้เป็นส่วนหนึ่งของการศึกษาตามหลักสูตรปรัชญาดุษฎีบัณฑิต
สาขาวิชาวิศวกรรมพลังงาน แบบ 1.1
ภาควิชาวิศวกรรมเครื่องกล
มหาวิทยาลัยศิลปากร
ปีการศึกษา 2568

PERFORMANCE IMPROVEMENT OF ANODE IN ZINC-AIR BATTERY BASED ON METALLURGY TECHNOLOGY

By
Mr. Chen SHUNHONG

A Thesis Submitted in Partial Fulfillment of the Requirements
for Doctor of Philosophy ENERGY ENGINEERING
Department of MECHANICAL ENGINEERING
Academic Year 2025

Title	Performance Improvement of Anode in Zinc-air Battery based on Metallurgy Technology
By	Mr. Chen SHUNHONG
Field of Study	ENERGY ENGINEERING
Advisor	Associate Professor Dr. Saroj Pullteap

Faculty of Engineering and Industrial Technology, Silpakorn University in Partial Fulfillment of the Requirements for the Doctor of Philosophy

.....
(Assistant Professor Dr. Arunsri Leejeerajumnian) Dean of Faculty of Engineering and Industrial Technology

Approved by

.....
(Assistant Professor Dr. Chaowalit Hamontree) Chairperson

.....
(Associate Professor Dr. Saroj Pullteap) Advisor

.....
(Assistant Professor Dr. Teerasak Hudakorn) Committee

.....
(Assistant Professor Dr. Chatthanon Bhothikhun) Committee

.....
(Assistant Professor Dr. Nopporn Patcharaprakiti) External Examiner

630930005 : Major ENERGY ENGINEERING

Keyword : zinc–air battery; electrodeposition; Ni foam; three-dimensional current collector zinc anode

Mr. Chen SHUNHONG : Performance Improvement of Anode in Zinc-air Battery based on Metallurgy Technology Thesis advisor : Associate Professor Dr. Saroj Pullteap

Zinc–air batteries (ZABs) are regarded as promising next-generation energy storage systems owing to their high theoretical energy density, earth-abundant zinc resources, and intrinsic safety. However, conventional planar zinc anodes in alkaline electrolytes suffer from severe ZnO passivation, dendritic growth, and “dead zinc” formation, which lead to increased polarization, capacity fading, and poor cycling stability. To address these critical issues, this dissertation systematically investigates the construction of Zn anodes by electrochemical deposition on three-dimensional (3D) Ni foam and their application in zinc–air batteries. First, the thermodynamic and kinetic processes of alkaline ZABs are analyzed. The discharge/charge mechanisms involving the “Zn → $Zn(OH)_4^{2-}$ → ZnO” dissolution–precipitation pathway of zinc, as well as the intrinsic correlation between local current density, 3D current collectors, and dendrite formation, are clarified. Based on this understanding, a design strategy is proposed that employs 3D porous Ni foam to disperse local current density, delay the continuous densification of ZnO, and suppress non-uniform zinc deposition. Subsequently, a complete experimental framework is established, including Ni foam pre-treatment, electrochemical deposition, Zn–air cell assembly, physical characterization, and electrochemical evaluation. Commercial Ni foam (thickness 1.5 mm, 100 PPI) is pre-treated by acid pickling, multi-step rinsing, ethanol cleaning, and drying. Zinc is then electrodeposited from 0.5 $mol \cdot L^{-1}$ $ZnSO_4$ solution at a constant current density of 0.11 $A \cdot cm^{-2}$ for 3, 4, and 5 h to obtain composite anodes Zn3, Zn4, and Zn5. These anodes are assembled into Zn–air cells Zn3B, Zn4B, and Zn5B, while a cell with a pure Zn plate anode (StZnB) is used as the reference (6 $mol \cdot L^{-1}$ KOH electrolyte, ambient air as the oxygen source). Multi-scale characterizations reveal that the electrodeposited Zn forms a continuous coating on the Ni foam skeleton, mainly in the metallic state with only a thin surface layer of adsorbed oxygen/hydroxyl species. With increasing deposition time, the average electrode thickness increases from about 0.80 mm (Zn3) to 0.93 mm (Zn4) and 1.00 mm (Zn5), and the Zn mass fraction reaches up to ~84 wt%. SEM observations show that Zn3 exhibits a loose, flocculent morphology with incomplete coverage; Zn4 develops uniform, continuous flake-like or flake–particle composite structures while preserving open pores; Zn5 presents pronounced block-like agglomeration and partial pore blockage. Electrochemical impedance spectroscopy (EIS) fitting indicates that Zn4 exhibits the lowest solution resistance and charge-transfer resistance, with Rs of about 0.55 Ω, suggesting the most favorable interfacial kinetics. Zn–air cell tests demonstrate that all cells possess initial open-circuit voltages (OCVs) higher than 1.37 V, among which Zn4B shows the highest OCV of ~1.396 V. Under continuous LED load for 6 h, Zn4B delivers an average load voltage of approximately 1.17 V and exhibits the most stable voltage and current output. Although Zn5B provides the highest initial current (~5.7 mA), it suffers from rapid current decay due to structural degradation and aggravated polarization caused by over-deposition. By correlating structural characterizations, EIS results, and cell performance, it is concluded that the Zn4 anode obtained after 4 h electrodeposition achieves an optimal balance among Zn loading, microstructure, and interfacial kinetics, and the corresponding Zn4B cell delivers the best overall performance. This work demonstrates that combining 3D Ni foam current collectors with well-controlled electrochemical deposition is an effective strategy to construct high-loading and stable Zn anodes and to improve the performance of zinc–air batteries. Future efforts may focus on broadening electrolyte systems, finely tuning deposition parameters, introducing in situ characterization techniques, and co-optimizing air electrodes, in order to further enhance the energy density and cycling life of rechargeable ZABs and promote their practical deployment in clean energy storage.

ACKNOWLEDGEMENTS

This dissertation represents the culmination of my doctoral studies and would not have been possible without the support, guidance, and encouragement of many individuals.

First and foremost, I would like to express my deepest gratitude to Associate Professor Dr. Saroj Pullteap, my dissertation advisor, for his unwavering support, insightful guidance, and exceptional patience throughout this work. His expertise, profound academic perspective, and invaluable life lessons have shaped not only my research but also my personal development. His broad vision in the academic field has significantly expanded my own viewpoints.

I am also sincerely grateful to Assistant Professor Dr. Chaowalit Hamontree, the chairperson, Assistant Professor Dr. Teerasak Hudakorn, Assistant Professor Dr. Chatthanon Bhothikhun, the internal dissertation committee members, as well as Assistant Professor Dr. Nopporn Patcharaprakiti, the external committee member. Their constructive comments and thoughtful suggestions during my dissertation defense have greatly enhanced the quality and relevance of this work for the research and academic community.

My heartfelt thanks also go to my family for their steadfast encouragement and unconditional support, especially during the most challenging moments of my doctoral journey. I would also like to thank all my laboratory members for their camaraderie, and the staff of the Department of Mechanical Engineering, Silpakorn University, along with all other personnel, for their technical and administrative assistance.

Chen SHUNHONG

TABLE OF CONTENTS

Page

LIST OF SYMBOLS

SymBol	Meaning
ZABs	Zinc–air batteries
ZnO	Zinc oxide
Zn	Zinc
3D	Three-dimensional
Ni	Nickel
$Zn(OH)_4^{2-}$	Tetrahydroxozincate(II) ion
mm	Millimetre
PPI	Pores per inch
$mol \cdot L^{-1}$	Moles per litre
$ZnSO_4$	Zinc sulfate
$A \cdot cm^{-2}$	Ampere per square centimetre
h	Hour
Zn3	Zn-deposited Ni foam sample with 3 h deposition
Zn4	Zn-deposited Ni foam sample with 4 h deposition
Zn5	Zn-deposited Ni foam sample with 5 h deposition
Zn3B	zinc–air battery assembled with Zn3 anode
Zn4B	zinc–air battery assembled with Zn4 anode
Zn5B	zinc–air battery assembled with Zn5 anode
StZnB	Standard Zn–air battery
KOH	Potassium hydroxide
wt%	Weight percent
SEM	Scanning electron microscopy / microscope
EIS	Electrochemical impedance spectroscopy
Rs	Solution resistance
Ω	Ohm
V	Volt
LED	Light-emitting diode
mA	Milliampere
IEA	International Energy Agency
CO_2	carbon dioxide
ESSs	electrochemical energy storage systems
ORR	oxygen reduction reaction
OER	oxygen evolution reaction
OH	hydroxide ion (OH^-)
Zn^2	zinc ion (Zn^{2+})
MOF	metal–organic framework
PbO	lead oxide
CTAB	cetyltrimethylammonium bromide
$CaCO_3$	calcium carbonate
MESL	Mechanical Embedded System Laboratory
AML	Advanced Materials Laboratory

SymBol	Meaning
NaOH	sodium hydroxide
GDL	gas diffusion layer
O_2	oxygen gas
SHE	standard hydrogen electrode
a_H_2O	activity of water
H_2O	water
CO_3^2	carbonate ion (CO_3^{2-})
K_2CO_3	potassium carbonate
Fe^3	ferric ion (Fe^{3+})
Fe^2	ferrous ion (Fe^{2+})
H_2	hydrogen gas
PVA	poly(vinyl alcohol)
TEAOH	tetraethylammonium hydroxide
Al_2	aluminum species (e.g., Al_2O_3 fragment)
SO_4	sulfate ion (SO_4^{2-})
KAl	potassium aluminum salt (e.g., $KAl(SO_4)_2 \cdot 12H_2O$)
XRD	X-ray diffraction
XPS	X-ray photoelectron spectroscopy
MnO_2	manganese dioxide
Br_2	bromine
NC	nitrogen-doped carbon
AR	analytical reagent grade
GF	glass fiber
HCl	hydrochloric acid
WE	working electrode
CE	counter electrode
EDS	energy-dispersive X-ray spectroscopy
TEM	transmission electron microscopy
F200S	JEOL JEM-F200S TEM model
OCV	open-circuit voltage
HRTEM	high-resolution transmission electron microscopy
Zn^o	metallic zinc (Zn^o)
ZnO_2^2	zincate species (ZnO_2^{2-})
OCVs	open-circuit voltages
X-CT	X-ray computed tomography
CT	computed tomography
GITT	galvanostatic intermittent titration technique
MgMn	magnesium–manganese mixed oxide
MXene	2D transition-metal carbide/nitride (MXene)
2D	Two-Dimensional
E^o	Standard Electrode Potential
ΔG	Gibbs Free Energy Change

SymBol	Meaning
n	Number of Electrons Transferred
F	Faraday Constant
E_cell	Cell Electromotive Force
R	Gas Constant
T	Temperature
a	Activity
E_work	Working Cell Voltage
E_eq	Thermodynamic Equilibrium Voltage
η_anode	Anode Overpotential
η_cathode	Cathode Overpotential
I	Current
R_ohmic	Ohmic Resistance
j_local	Local Current Density
A	Electrochemically Active Area
m	Deposited Mass
M	Molar Mass
t	Time
h	Average Film Thickness
ρ	Density
PVA	Polyvinyl Alcohol
NC	Nitrogen-Doped Carbon
Rct	Charge-Transfer Resistance

CHAPTER 1
INTRODUCTION

1.1 Motivation

The continuous development of human society has driven a rapid increase in global energy demand, while traditional fossil fuels can no longer meet the ever-growing consumption needs. [1] Long-term dependence on fossil fuels not only exacerbates the energy crisis, but also leads to severe environmental pollution and climate change, placing the global energy system under profound pressure for transformation. According to data from the International Energy Agency (IEA), global energy-related CO_2 emissions reached a new record high in 2024, highlighting the urgency of energy transition. [2] Meanwhile, renewable energy sources such as wind, solar, tidal, and biomass are experiencing unprecedented growth. [3, 4] However, these clean energy sources are inherently intermittent and fluctuating—electricity is available only when the wind blows or the sun shines, and unavailable otherwise—which severely constrains their ability to provide stable power. [3 , 5 , 6] Therefore, the development of efficient, large-scale, low-cost, and highly reliable electrochemical energy storage systems (battery energy storage systems, ESSs) is essential for smoothing the grid integration of renewable energy, building smart grids, and promoting clean energy utilization in end-use sectors such as electric vehicles. [7-11]

Among various electrochemical energy storage technologies, lithium-ion batteries have achieved tremendous commercial success over the past three decades. With a highly mature industrial chain, they are widely used in consumer electronics, electric vehicles, and stationary energy storage. [5, 7-13] Nevertheless, their further development faces several bottlenecks. First, the key raw materials (such as lithium, cobalt, and nickel) are geographically concentrated, relatively scarce, and subject to drastic price fluctuations, which raises concerns regarding cost control and supply-chain security. Second, the energy density of state-of-the-art lithium-ion batteries is approaching its theoretical limit [14-18], restricting further improvement and making it increasingly difficult to meet the growing demand for longer driving ranges in electric vehicles. Finally, safety issues arising from thermal runaway or internal short circuits, which may trigger fires, remain a serious challenge for lithium-ion batteries. [14-21]

To address these issues associated with lithium-ion batteries, various alternative battery systems have been proposed and developed. Among the candidates for next-generation batteries, metal–air batteries have attracted extensive attention due to their ultrahigh theoretical energy density and environmental friendliness. In metal–air batteries, oxygen from ambient air is used as the cathode reactant, which not only reduces the battery weight but also significantly enhances the overall energy density. This greatly promotes further improvement in battery energy density. Typical metal–air batteries include lithium–air, sodium–air, potassium–air, zinc–air, magnesium–air, aluminum–air, and iron–air batteries. [22-28] Among all these metal–air systems, lithium–air batteries possess the highest theoretical energy density, as illustrated in Fig. 1.1.

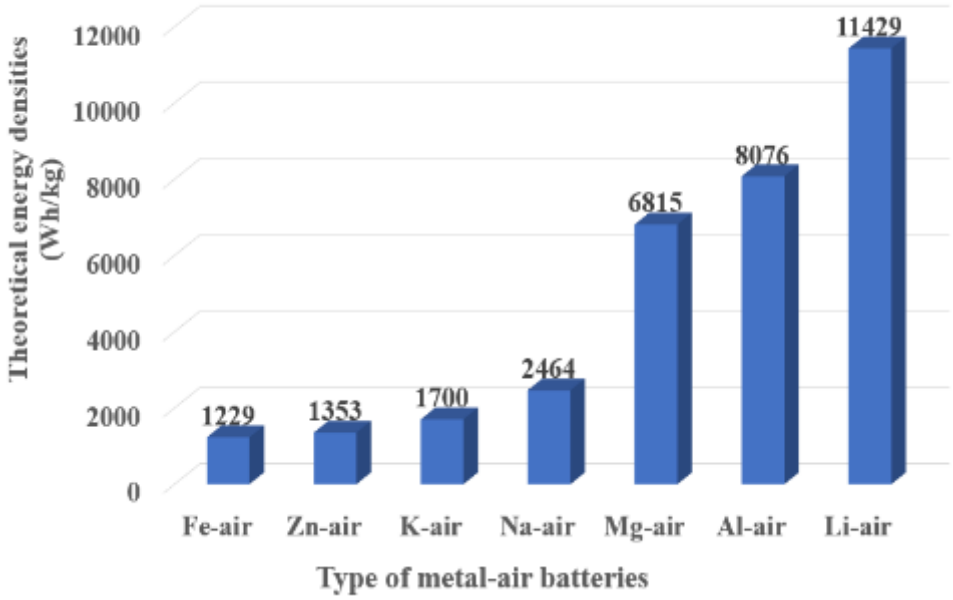

Fig. 1.1 Theoretical energy densities of metal–air batteries [29]

However, lithium–air batteries themselves also face numerous challenges. For example, the discharge process generates by-products that readily accumulate on the cathode surface, leading to electrode blockage and incomplete discharge. [26] In addition, the charging overpotential is significantly higher than the discharging overpotential, resulting in low energy efficiency. [30] These issues severely limit the practical application of lithium–air batteries. Moreover, magnesium–air and aluminum–air batteries suffer from relatively low reduction potentials and generally severe self-discharge, while iron–air batteries are difficult to meet high–energy-density storage demands due to their relatively low energy density (763 Wh kg^{-1}) and open-circuit voltage (1.28 V).

By contrast, zinc–air batteries (ZABs) have emerged as a research hotspot in recent years owing to their unique advantages. First, zinc is the fourth most abundant metal element in the Earth's crust, with widespread resource distribution and well-established mining and smelting technologies. Compared with lithium, cobalt, and nickel, zinc is much cheaper and exhibits long-term price stability, which endows ZABs with a significant cost advantage for large-scale energy storage applications. Second, ZABs possess a high theoretical energy density of up to 1086 Wh kg^{-1}, which is about 3–5 times that of current commercial lithium-ion batteries (250–300 Wh kg^{-1}), and a high volumetric energy density of 6163 Wh L^{-1} [3]. Finally, benefiting from the use of aqueous electrolytes, ZABs offer pronounced safety advantages, fundamentally eliminating the flammability and explosion risks associated with solid-state or organic electrolytes. Meanwhile, zinc is non-toxic and environmentally benign, and the battery components are easy to recycle, in line with the concept of green and

sustainable development. Overall, ZABs, which simultaneously feature high energy density, enhanced safety, and low cost, are regarded as one of the most promising next-generation energy storage technologies. In Table 1.1, we compare the performance and other key parameters of zinc–air batteries with those of other commercial batteries.

Table 1.1 Comparison of performance parameters of zinc–air batteries with other types of commercial batteries [3, 31-35]

Performance parameter	Zinc–air battery (theoretical)	Zinc–air battery (typical commercial)	Lithium-ion battery (NMC)	Lead–acid battery
Energy density (Wh kg^{-1})	1086	300 - 500	150 - 300	30 - 50
Power density (W kg^{-1})	Moderate	50 - 200	250 - 1000	75 - 300
Raw material cost	Very low	low	High	low
Safety	High	High	Medium/low	High
Environmental friendliness	Excellent	Excellent	Medium (contains heavy metals)	Poor (contains lead)

The development of zinc–air batteries can be regarded as a technological evolution from primary chemical power sources to highly efficient rechargeable systems, as illustrated in Fig. 1.2.

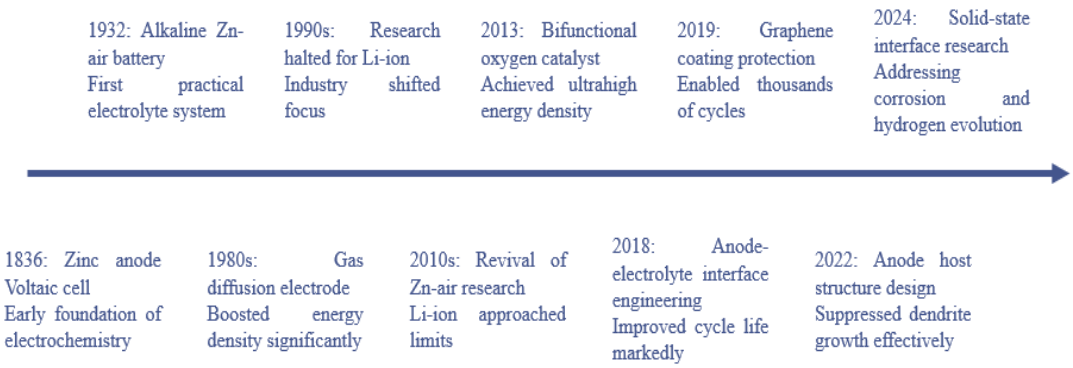

Fig. 1.2 Development history of zinc–air batteries [36-41]

As shown in Fig. 1.2, the early concept of zinc–air batteries can be traced back to 1878. In 1932, the French engineer Georges L. Ferrysh first introduced an alkaline electrolyte in combination with a sintered carbon air electrode, thereby establishing the basic structural prototype of modern zinc–air batteries. In the mid-20th century, owing to their high theoretical energy density, excellent safety, and low cost, primary zinc–air batteries were rapidly commercialized and widely used in applications requiring long-term stable discharge, such as hearing aids, railway signal power supplies, and navigation beacons. [30, 42-44] Entering the 1980s, the rapid development of portable electronic devices and electric vehicles led to a surge in demand for high–energy-density rechargeable batteries, driving the transition of zinc–air battery research from primary systems toward reversible charge–discharge systems. However, this transition was long constrained by two major bottlenecks associated with the air cathode and the zinc anode: the former lacked efficient, durable, and cost-effective bifunctional catalysts capable of simultaneously promoting the oxygen reduction reaction (ORR) and oxygen evolution reaction (OER), while the latter was prone to dendrite formation, shape change, and side reactions during cycling, resulting in electrode failure and capacity degradation.

In the 21st century, advances in nanomaterials and structural engineering have injected new vitality into this field. Nanocarbon materials such as carbon nanotubes and graphene, when used as supports for single-atom catalysts or transition-metal-based compounds, have significantly improved the catalytic performance of air cathodes. Meanwhile, the adoption of three-dimensional porous current collectors (e.g., carbon fibers) has been shown to promote more uniform zinc deposition and effectively suppress dendrite growth, thereby markedly extending the cycling lifetime. [45-48] At present, research on rechargeable zinc–air batteries is rapidly moving toward practical applications in flexible wearable electronics and large-scale energy storage systems. Their development trajectory clearly reflects a continuous evolution and technological integration from fundamental chemical systems to engineering-oriented structural optimization.

A typical rechargeable zinc–air battery usually consists of a porous air cathode, a metal zinc anode, and an alkaline electrolyte, as shown in Fig. 1.3. Its energy conversion process involves two stages, namely discharge and charge:

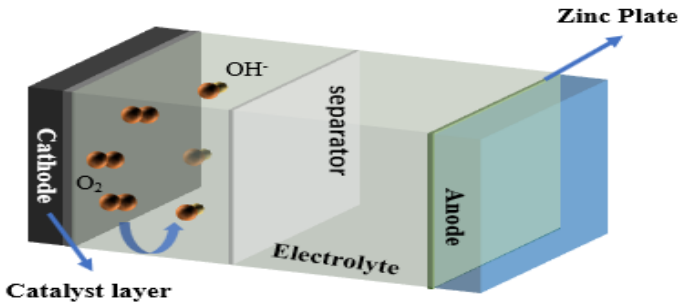

Fig. 1.3 Schematic diagram of the structure of a rechargeable zinc–air battery [49]

During discharge, oxygen from ambient air diffuses into the air cathode and undergoes the oxygen reduction reaction (ORR) on the catalyst surface to generate hydroxide ions (OH^-). Meanwhile, metallic zinc at the anode is oxidized, losing electrons to form zincate ions ($Zn(OH)_4^{2-}$), which are subsequently converted into zinc oxide (ZnO). Electrons flow from the anode to the cathode through the external circuit, thereby delivering electrical energy.

During charge, driven by an applied voltage, the reaction proceeds in the reverse direction: the air cathode undergoes the oxygen evolution reaction (OER), releasing oxygen gas, while Zn^{2+} species at the zinc anode are reduced and redeposited as metallic zinc, thus achieving energy storage.Despite their broad application prospects, the large-scale commercialization of zinc–air batteries, especially in rechargeable systems, is still hindered by three key scientific and technological challenges.

First, the reaction kinetics at the air cathode are intrinsically sluggish. Both the oxygen reduction reaction (ORR) and the oxygen evolution reaction (OER) involve complex multi-electron transfer processes with very slow kinetics, which severely limit the energy efficiency and power density of the battery. At present, commercial systems mainly rely on noble-metal-based catalysts, such as platinum for ORR and iridium- or ruthenium-based oxides for OER. However, these catalysts are extremely expensive and resource-limited, making them unsuitable for large-scale applications. Therefore, the development of efficient, durable, and low-cost bifunctional oxygen catalysts is a crucial direction for promoting the commercialization of zinc–air batteries.

Second, the reversibility of the zinc anode has not yet been fundamentally resolved. In alkaline electrolytes, the zinc anode suffers from multiple adverse reactions and structural degradations, including dendrite growth, shape change, surface passivation, and hydrogen evolution corrosion, as illustrated in Fig. 1.4. These issues significantly deteriorate the cycling lifetime and Coulombic efficiency.

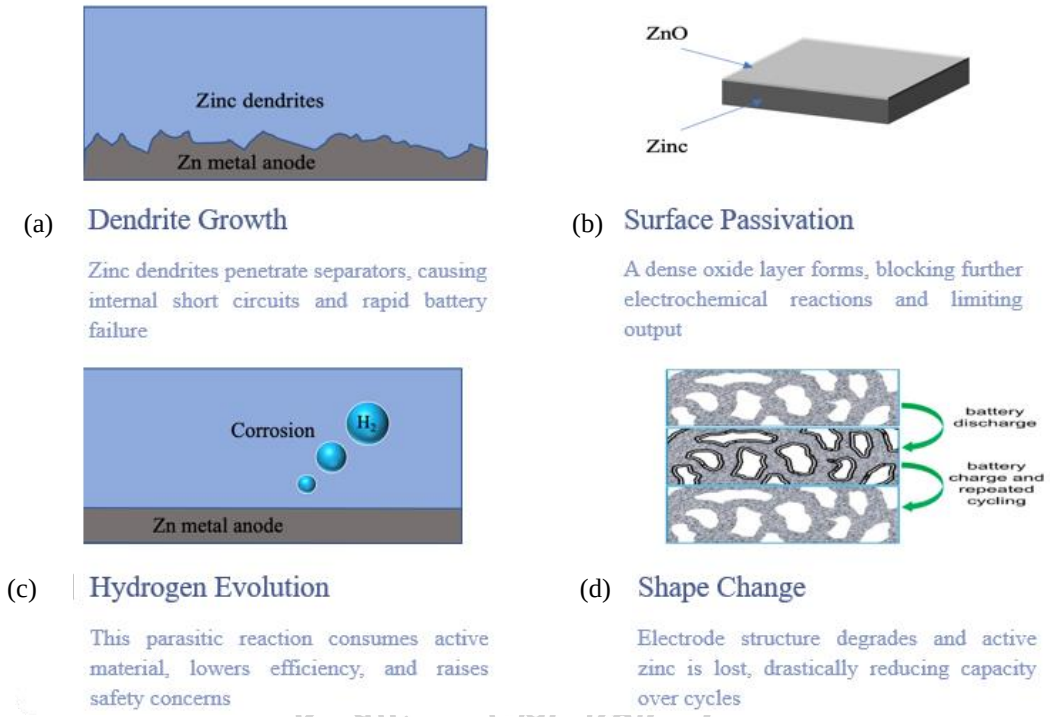

Fig. 1.4 Challenges facing the zinc anode in zinc–air batteries:(a) Dendrite Growth, (b) Surface Passivation, (c) Hydrogen Evolution, (d) Shape Change [50]

Fig. 1.4 (a) schematically illustrates the formation of zinc dendrites during zinc deposition (charging). Owing to the non-uniform distribution of the electric field and the limited number of nucleation sites, zinc ions tend to nucleate and deposit preferentially at protrusions on the electrode surface, where the local current density is further intensified, giving rise to a “tip effect.” This positive feedback process drives the continuous growth of zinc in dendritic or mossy morphologies. The resulting dendrites may pierce the separator and cause internal short circuits, or detach from the current collector to form “dead zinc,” leading to loss of active material and capacity fading. Fig. 1.4 (b) shows a schematic illustration of surface passivation caused by discharge products on the zinc anode. The discharge product ZnO has limited solubility in alkaline electrolytes and readily precipitates as a dense insulating layer once the solution becomes supersaturated. This passivation layer blocks the contact between the electrolyte and the electrode, increases the reaction resistance, and induces severe polarization. Consequently, the operating voltage of the battery decreases, the actual discharge capacity falls far below the theoretical value, and the discharge process is prematurely terminated. Fig. 1.4 (c) depicts hydrogen evolution corrosion of the zinc anode in alkaline electrolytes. Since the standard electrode potential of zinc is lower than that of hydrogen evolution, zinc can spontaneously react with water in alkaline media to generate hydrogen gas. This parasitic reaction consumes active zinc and lowers the Coulombic efficiency. Meanwhile, the accumulation of hydrogen gas may increase the

internal pressure of the cell, posing safety risks such as swelling and even explosion. Fig. 1.4 (d) presents a schematic of macroscopic shape change of the zinc anode during repeated charge–discharge cycling. Under the combined influence of non-uniform current density distribution, electric field effects, and concentration gradients of zincate ions, the dissolution and redeposition of zinc do not proceed in a spatially reversible manner. Active material migrates and redeposits in new regions, causing edge thickening, central corrosion, or overall distortion of the electrode. Such shape changes destroy the structural integrity of the electrode, increase the internal resistance, accelerate capacity decay, and ultimately impose severe limitations on the cycling life of the battery.The main causes of efficiency loss in zinc–air batteries associated with the zinc anode are summarized in Table 1.2.

Table 1.2 Main issues of zinc anodes in alkaline electrolytes and their consequences

Issue type	Cause	Consequences
Zinc dendrites	Non-uniform zinc-ion deposition and locally excessive current density	Short-circuit failure, low Coulombic efficiency, shortened cycling life
Hydrogen evolution corrosion	Thermodynamic instability of zinc in alkaline electrolytes and parasitic reaction with water	Self-discharge, capacity fading, electrolyte dry-out, safety risks
Shape change	Macroscopic migration and redistribution of zinc during charge–discharge cycling	Decreased utilization of active material, electrode deformation, increased internal resistance
Surface passivation	Low solubility of ZnO discharge products and formation of a dense insulating layer on the electrode surface	Increased electrode polarization, unreleased capacity, premature termination of discharge

In response to the aforementioned challenges, researchers worldwide are actively exploring solutions from multiple perspectives, including materials design, structural optimization, and interfacial regulation.

For the air cathode, current research mainly focuses on the development of non-precious bifunctional catalysts. Transition-metal-based materials (such as oxides, sulfides, nitrides, and carbon composites of cobalt, manganese, iron, and nickel) have become research hotspots due to their low cost, abundant resources, and tunable activity. In particular, anchoring active nanoparticles onto high–specific-surface-area and porous carbon supports (e.g., graphene and carbon nanotubes) can significantly increase the exposure of active sites and facilitate electron transport as well as reactant diffusion (see Fig. 1.5). In recent years, novel systems such as metal–organic framework (MOF)-

derived carbon materials and single-atom catalysts have also exhibited outstanding catalytic activity and structural stability, providing new directions for constructing high-performance air cathodes.

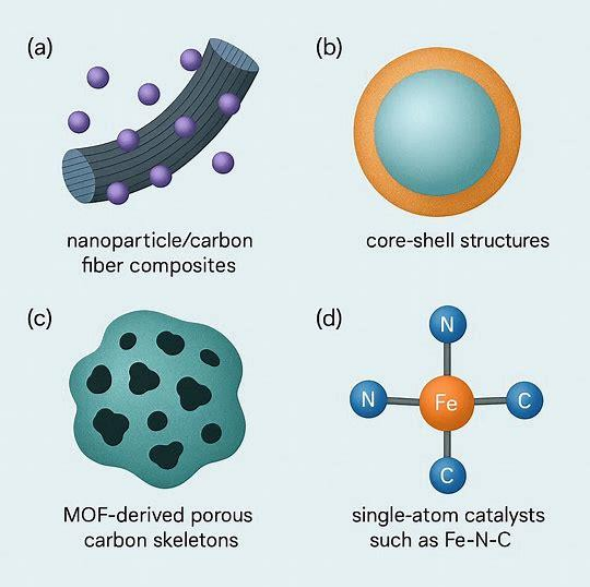

Fig. 1.5 Structural schematics of various advanced bifunctional oxygen catalysts: (a) Nanoparticle/carbon fiber composite, (b) core–shell structure, (c) MOF-derived porous carbon framework, (d) ball-and-stick model of a single-atom catalyst (e.g., Fe–N–C) [51, 52]

For the zinc anode, optimization strategies mainly focus on three aspects: electrolyte modification, interfacial engineering, and structural design. In terms of electrolyte modification, the introduction of corrosion inhibitors (such as PbO, $In(OH)_3$, CTAB, etc.) can effectively suppress hydrogen evolution corrosion. Meanwhile, by tailoring the electrolyte system (for example, using ionic liquids, deep eutectic solvents, or solid-state electrolytes), the zinc deposition behavior and interfacial stability can be fundamentally improved. From the perspective of interfacial engineering, constructing artificial protective layers (such as ZnO, $CaCO_3$, or polymer coatings) on the zinc surface can physically isolate the electrode from the electrolyte and regulate the interfacial electric field distribution, thereby guiding uniform zinc deposition and enhancing cycling reversibility. With respect to structural design, the use of three-dimensional (3D) porous current collectors is considered one of the most effective approaches for anode optimization. Compared with conventional two-dimensional (2D) metal foils (such as zinc foil or copper foil), 3D porous substrates (e.g., copper foam) possess a much higher specific surface area, which can significantly reduce the local current density and provide abundant nucleation sites. As a result, zinc tends to deposit uniformly and densely within the porous framework, effectively suppressing dendrite growth and electrode deformation. as illustrated in Fig. 1.4.

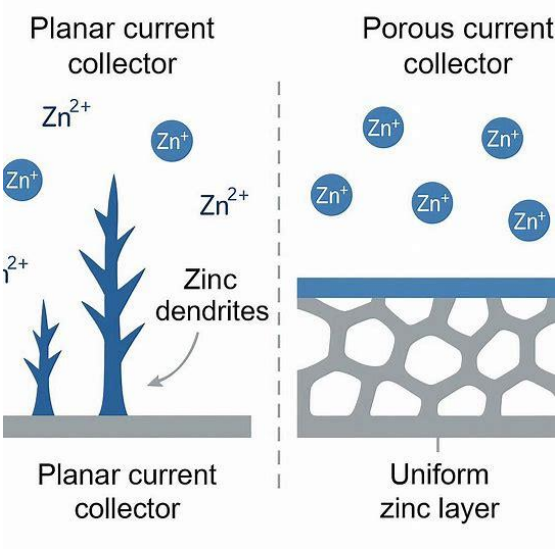

Fig. 1.6 Schematic illustration of the influence of two-dimensional planar current collectors and three-dimensional porous current collectors on zinc deposition behavior [47, 53]

In summary, the development of high-performance, long-life rechargeable zinc–air batteries is of great significance for realizing the energy transition. Among the various factors, addressing the irreversibility of the zinc anode is key to improving the cycling stability of the battery. To conclude, the present study adopts a structural optimization strategy—electrodepositing zinc on three-dimensional (3D) porous current collectors—to enhance anode performance. Among the different types of 3D current collectors, nickel foam is considered a highly promising substrate for zinc anodes owing to its excellent electrical conductivity, high porosity, good mechanical strength, and well-established industrial foundation. Meanwhile, electrodeposition, as a mature surface-engineering technique, offers the advantages of simple equipment, convenient operation, fast deposition rate, low cost, and easy scalability. By precisely regulating the electrodeposition parameters (such as current density, deposition time, electrolyte composition, and types of additives), the morphology, grain structure, crystallographic orientation, and adhesion strength of the deposited zinc can be effectively controlled.

This work aims to develop a high-performance zinc–air battery anode to enhance the output stability and cycling life of the battery. Specifically, zinc is electrodeposited on nickel foam substrates, and the structure–property relationships among electrodeposition parameters, the microstructure of the zinc deposit layer, and the resulting electrochemical performance are systematically investigated. The ultimate goal is to obtain an ideal zinc anode that can effectively suppress dendrite formation, reduce the corrosion rate, and improve cycling stability, thereby comprehensively enhancing the overall performance of zinc–air batteries. The research mainly consists of two stages: (1) fabricating electrodeposited zinc anodes on nickel foam and evaluating the performance of the corresponding

zinc–air batteries; and (2) preparing a series of samples by tuning the electrodeposition parameters, systematically comparing their structural and electrochemical characteristics, and elucidating the influence of these parameters on electrode behavior. The results of this study will provide experimental evidence and theoretical guidance for the optimization of anodes in rechargeable zinc–air batteries, and offer new design concepts for the development of high-performance energy storage devices.

1.2 Objective of dissertation

To develop a high-performance anode for zinc–air batteries by electrodepositing zinc onto nickel foam, thereby enhancing the overall performance of zinc–air batteries.

1.3 Scopus of research

This study is dedicated to developing a nickel-foam-based zinc anode prepared by electrodeposition for application in zinc–air batteries. The research mainly investigates the effects of deposition parameters and surface modification on the microstructure and electrochemical performance of the anode.

The scope of the work includes:

(1) Electrodepositing zinc on nickel foam to obtain a new anode and evaluating the performance of the corresponding zinc–air batteries.

(2) Preparing zinc anodes with different deposition times in order to elucidate the influence of deposition time on the performance of zinc–air batteries.

(3) Conducting electrochemical characterization by cyclic voltammetry, galvanostatic charge–discharge testing, and electrochemical impedance spectroscopy.

All experiments are carried out under laboratory conditions, using aqueous electrolytes and small-scale cell configurations.

1.4 Expected benefits

1) To acquire practical knowledge of applying electrodeposition technology for depositing zinc on nickel foam.

2) To master electrochemical characterization methods for zinc anodes.

3) To master the assembly procedures of zinc–air batteries and the corresponding battery performance testing methods.

1.5 Location of research

- Mechanical Embedded System Laboratory (MESL), Department of Mechanical Engineering, Faculty of Engineering and Industrial Technology, Silpakorn University (Sanam Chandra Palace Campus), Nakhon Pathom 73000, Thailand.

- Advanced Materials Laboratory (AML), School of Mechanical Engineering, Chengdu University.

1.6 Founding sources

Department of Mechanical Engineering, Faculty of Engineering and Industrial Technology Silpakorn University.

1.7 Dissertation period

This dissertation has been conducted from the academic year 2021-2025

Operation Steps	2023						2024												2025											
	7	8	9	10	11	12	1	2	3	4	5	6	7	8	9	10	11	12	1	2	3	4	5	6	7	8	9	10	11	12
1. Literature reviews																														
2. Prepare for topic defense																														
3. Equipment configuration and experimental design																														
4. Battery material development and battery fabrication																														
5. Battery performance testing																														
6. Analyze and discuss experimental results																														
7. Summarize and prepare a report on results of research																														
8. Accuracy of report																														
9. Deliver dissertation report book to graduate school																														

CHAPTER 2
RELATED THEORIES

This chapter provides an in-depth discussion of the core theories involved in this study, which can be divided into two main parts: (1) the basic structure and working mechanism of zinc–air batteries, with particular emphasis on their thermodynamic and kinetic processes; and (2) the fundamental principles of electrodeposition, the process kinetics, and the key factors affecting the quality of the deposited layer. A thorough understanding of these theoretical aspects is a prerequisite for designing and optimizing high-performance zinc–air batteries based on electrodeposited Zn/Ni foam composite anodes.

2.1 Overall structure and " semi – open " operating characteristics of zinc – air batteries

Zinc–air batteries are a typical class of metal–air batteries, in which metallic zinc or zinc alloys are used as the anode, while oxygen from ambient air serves as the cathodic reactant, enabling the direct conversion of the chemical energy of zinc into electrical energy. Compared with conventional sealed secondary batteries, a distinctive feature of zinc–air batteries lies in the fact that the active material of the cathode is oxygen from air, and the battery exhibits a "semi-open" configuration. On the one hand, this design significantly increases the theoretical specific energy (with zinc bearing most of the mass contribution); on the other hand, it introduces complex multiphase mass transfer and side reactions that are strongly coupled with the ambient atmosphere (especially CO_2 concentration and humidity).

A typical alkaline zinc–air battery consists of a zinc anode, an alkaline electrolyte, a separator, and an air cathode (gas diffusion electrode), as illustrated in Fig. 2.1.

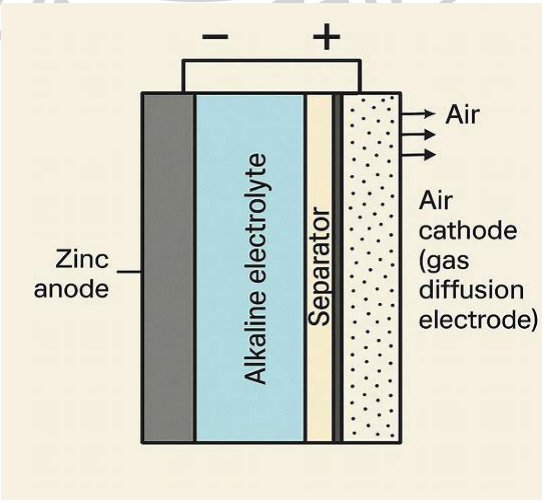

Fig. 2.1 Schematic illustration of a typical zinc–air battery structure [2]

The functions of each component can be summarized as follows:

- Zinc anode (usually composed of zinc powder, zinc plates, or zinc alloys): this is the site that provides oxidizable metallic zinc. In alkaline electrolytes, metallic zinc undergoes a series of complex processes during discharge, including dissolution, redeposition, and bulk-phase transformation. The interfacial structure and morphological evolution of the zinc anode directly determine the reversibility, capacity utilization, and cycling life of the battery.

- Electrolyte (most commonly concentrated alkaline solutions such as KOH or NaOH; in recent years, neutral or near-neutral buffered electrolytes have also been developed): (1) provides OH^- ions that participate in both the anode and cathode reactions, thereby enabling ionic conduction; (2) regulates the dissolution–deposition behavior of zinc through the formation and dissolution of $Zn(OH)_4^{2-}$; and (3) its conductivity, viscosity, and CO_2 absorption capacity significantly influence ohmic polarization, mass-transport polarization, and the formation of carbonate by-products.

- Separator/separating layer: the separator physically isolates the zinc anode from the gas diffusion cathode to prevent direct contact and short circuit, while still allowing OH^- and other ions to migrate freely. The pore structure, hydrophobic/hydrophilic balance, and chemical stability of the separator affect electrolyte wetting, the precipitation sites of ZnO, and the risk of dendrite penetration.

- Gas diffusion cathode (air cathode): one side of the air electrode is exposed to air and responsible for oxygen intake; the other side is in contact with the electrolyte, where the oxygen reduction reaction (ORR) and oxygen evolution reaction (OER) take place. A typical air cathode consists of a current collector, a gas diffusion layer (GDL), and a catalyst layer. The catalyst layer provides interconnected ORR/OER active sites and a conductive network, while the GDL maintains stable gas–liquid–solid three-phase interfaces and ensures efficient gas transport. Essentially, the energy conversion during charge–discharge cycling of zinc–air batteries arises from the coupling between the reversible oxidation/reduction of zinc at the anode and the ORR/OER electrocatalytic processes at the air cathode.

2.2 Electrochemical reactions and thermodynamic analysis during discharge

During discharge, the zinc anode acts as the electron donor and is oxidized, while the air cathode captures oxygen from the environment and drives the oxygen reduction reaction (ORR). These two electrodes work cooperatively to complete the closed-loop transport of electrons and hydroxide ions.

Anode (discharge): In an alkaline electrolyte, the zinc anode first reacts with hydroxide ions in the electrolyte to form soluble tetrahydroxozincate $Zn(OH)_4^{2-}$ and release electrons. The fundamental reaction can be expressed as: [7, 54]

$$Zn + 4OH^- \rightarrow Zn(OH)_4^{2-} + 2e^- (E^0 = -1.25\ V\ vs.\ SHE) \qquad (2-1)$$

As discharge proceeds, the concentration of $Zn(OH)_4^{2-}$ near the electrode/electrolyte interface gradually increases. Once the local concentration reaches supersaturation, $Zn(OH)_4^{2-}$ decomposes and precipitates to form sparingly soluble ZnO:

$$Zn(OH)_4^{2-} \rightarrow ZnO + H^2O + 2OH^- \quad (2-2)$$

By combining Eqs. (2-1) and (2-2), the overall discharge reaction at the anode can be written as:

$$Zn + 2OH^- \rightarrow ZnO + H_2O + 2e \quad (2-3)$$

Cathode (discharge, ORR): Oxygen molecules from air diffuse into the gas diffusion electrode and, under the action of the catalyst, participate in the reduction reaction at the electrode–electrolyte interface to generate hydroxide ions:

$$O_2 + 2H_2O + 4e^- \rightarrow 4OH^- \ (E^0 = +0.40\ \text{V vs. SHE}) \quad (2-4)$$

Accordingly, the overall cell reaction during discharge can be written as:

$$2Zn + O_2 \rightarrow 2ZnO \ (E^0\_cell = 1.65\ \text{V}) \quad (2-5)$$

To provide a more intuitive understanding of the relationship between the anodic and cathodic half-reactions and the overall reaction, as well as the associated mass transport pathways, the electrochemical behavior of the discharge process can be summarized as illustrated in Fig. 2-2.

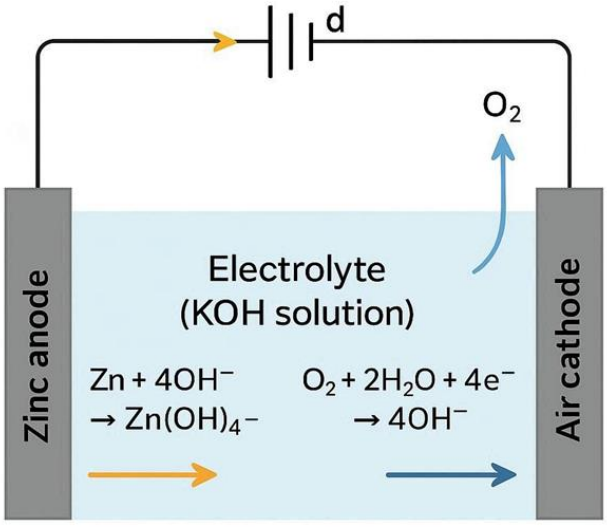

Fig. 2.2 Schematic illustration of the discharge process in a zinc–air battery [8]

From Fig. 2.2, it can be seen that during discharge metallic Zn at the zinc electrode reacts with OH^- ions to form soluble $Zn(OH)_4^{2-}$ while releasing electrons. The electrons flow through the external circuit toward the air electrode. Meanwhile, the air electrode continuously takes up O_2 from the gas phase; at the catalyst layer, oxygen undergoes reduction to generate OH^-, which then migrates back to the zinc electrode through the electrolyte, thus completing the ionic circuit. When the locally generated $Zn(OH)_4^{2-}$ becomes supersaturated near the interface, it further decomposes and precipitates as ZnO, forming a surface product layer that evolves continuously as discharge proceeds.

Under standard conditions, the standard electrode potentials of the Zn/ZnO and O_2/OH^- half-cells are approximately −1.25 V and +0.40 V (vs. SHE), respectively, corresponding to a theoretical open-circuit voltage of about 1.65 V. As shown in Fig. 2.3, the thermodynamic energy levels of the Zn/ZnO and O_2/OH^- couples can be visualized more intuitively.

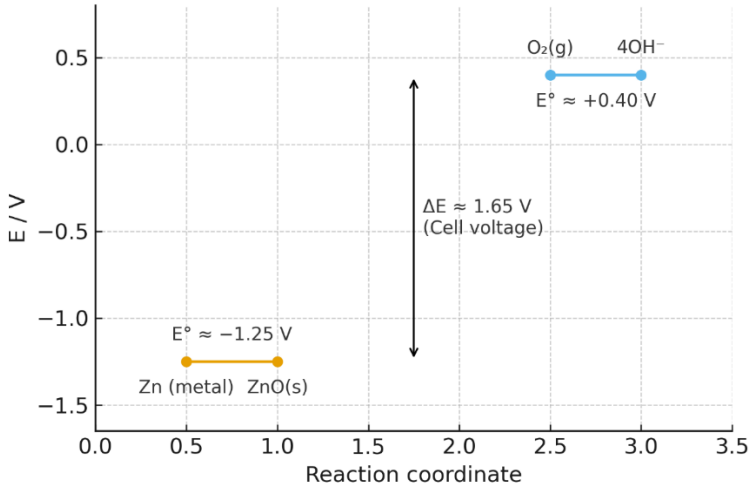

Fig. 2.3 Thermodynamic potentials and energy diagram of a zinc–air battery [55]

The change in Gibbs free energy can be expressed as:

$$\Delta G = -nFE\_cell \qquad (2-6)$$

where n is the number of electrons transferred (n = 4), F is the Faraday constant, and E_cell is the cell electromotive force. According to Eq. (2-6), the zinc–air system theoretically possesses a very high specific energy (with theoretical values exceeding 1000 $Wh \cdot kg^{-1}$), which is one of its major advantages over conventional lithium-ion batteries.

Under practical operating conditions, the electrode potentials are also influenced by the activities of reactants and products, solution pH, O_2 partial pressure, and other factors, which can be described by the Nernst equation. Taking the oxygen reduction reaction as an example:

$$E\_ORR = E\_ORR^{0} + (RT/4F)\ln(a\_OH^{-4} / (a\_O_2 \cdot a\_H_2O^2)) \quad (2-7)$$

In the presence of excess water, $a\_H_2O \approx 1$. An increase in pH (i.e., higher OH^- activity) and elevated O_2 partial pressure both tend to increase the ORR potential and thus raise the discharge voltage. This indicates that, by rationally controlling the electrolyte concentration, gas transport, and electrode structure, the practical operating potential of zinc–air batteries can be optimized to a certain extent.

2.3 Charging process and limitations in reversibility and kinetics

For a rechargeable zinc–air battery, when an external power supply applies a reverse voltage, the aforementioned discharge reactions proceed in the opposite direction, thereby converting electrical energy back into chemical energy. In this case, the roles of the electrodes are interchanged: the air electrode serves as the anode (positive electrode) where the oxygen evolution reaction (OER) occurs, while the zinc electrode acts as the cathode (negative electrode) where zinc is reduced and electrodeposited.

During charging, the discharge reactions are reversed. The battery extracts electrical energy from the external power source and converts the discharge products back into the original reactants, thus achieving energy storage. The air electrode switches from the oxygen reduction reaction (ORR) to the oxygen evolution reaction (OER), whereas the zinc electrode reduces ZnO formed during discharge back to metallic zinc, regenerating the active material. The effectiveness of this process directly determines the rechargeability and cycling life of zinc–air batteries. The fundamental processes are illustrated in Fig. 2.4.

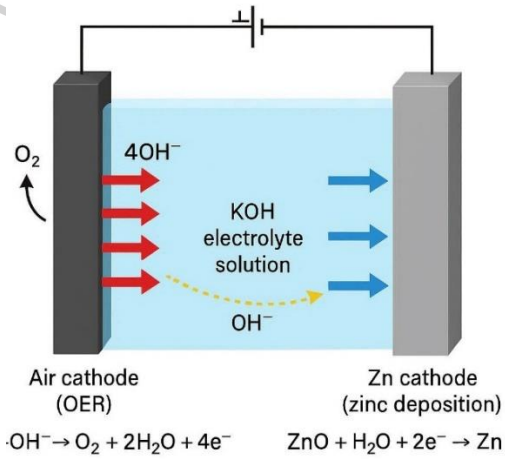

Fig. 2.4 Schematic illustration of the charging process of a zinc–air battery [56]

As shown in Fig. 2.4, during charging, the polarity of the air electrode is reversed and it becomes the anode where the OER takes place; OH^- ions are oxidized on its surface to produce O_2 and H_2O. The zinc electrode functions as the cathode, where ZnO generated during discharge is reduced and redeposited as metallic Zn in the alkaline environment, while OH^- is regenerated. Electrons flow through the external circuit from the air electrode to the zinc electrode, whereas OH^- migrates from the zinc side toward the air electrode. The degree of reversibility of the charge–discharge processes, together with the kinetic mismatch between the two electrodes, jointly determines the charge–discharge voltage gap and the overall energy efficiency of the battery.

The main half-reactions can be written as follows:

Anodic reaction (oxygen evolution reaction, OER):

$$4OH^- \rightarrow O_2 + 2H_2O + 4e^- \qquad (2-8)$$

Cathodic reaction (zinc reduction and deposition):

$$ZnO + H_2O + 2e^- \rightarrow Zn + 2OH^- \qquad (2-9)$$

From the reversibility implied by Eqs. (2-3) and (2-4), it can be seen that, in an ideal case, the charge and discharge processes should constitute a pair of perfectly reversible redox reactions. However, in practical systems, the electrode kinetics are often sluggish due to the complex multi-electron transfer steps coupled with bond breaking and formation (particularly in the OER), leading to significant electrode polarization and a pronounced charge–discharge voltage gap.

Qualitatively, the operating cell voltage can be expressed as:

$$E\_work \approx E\_eq - \eta\_anode - \eta\_cathode - I \cdot R\_ohmic \qquad (2-10)$$

where E_eq is the thermodynamic equilibrium voltage, η_anode and η_cathode are the overpotentials at the anode and cathode, respectively, and I·R_ohmic represents the ohmic drop associated with the electrolyte, electrodes, and current collectors. To qualitatively understand the contributions of various polarization sources to the operating voltage, the actual E–j curve at a given operating point can be decomposed into different loss components, as illustrated in Fig. 2.5.

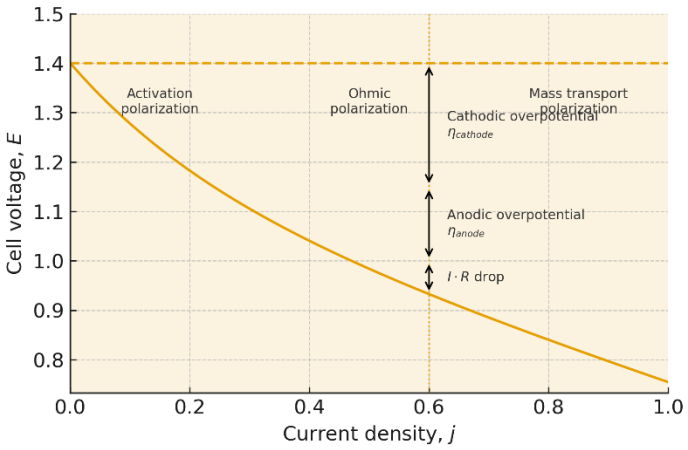

Fig. 2.5 Schematic illustration of the operating voltage and various polarization losses in a practical zinc–air battery [56]

In Fig. 2.5, the theoretical equilibrium voltage E_eq is determined by thermodynamics, whereas the actual working voltage E_work decreases as the current density increases. The difference between them can be further decomposed into several components, including the activation polarization at the anode and cathode, ohmic polarization, and mass-transport polarization in the high-current-density region. For zinc–air batteries, in addition to the ohmic losses originating from the electrolyte and current collectors, the sluggish multi-electron ORR/OER kinetics at the oxygen electrode and the charge-transfer resistance of the zinc electrode under the coverage of a ZnO passivation layer are the primary causes of the pronounced charge–discharge voltage gap. Therefore, reducing ORR/OER polarization and ohmic polarization is crucial for narrowing the charge–discharge voltage gap and improving the energy efficiency.

2.4 Electrode/electrolyte interface and mass transport processes

The electrochemical behavior of zinc–air batteries is not only governed by thermodynamics, but more fundamentally constrained by the coupling between interfacial charge transfer and mass transport in the electrolyte. Taking the zinc anode as an example, a complete electrochemical process generally involves the following steps: [57-60]

(1) Migration of $Zn(OH)_4^{2-}$ from the bulk electrolyte to the electrode surface (including migration, diffusion, and convection);

(2) Desolvation and adsorption of ions at the electrode/electrolyte interface;

(3) Interfacial electron transfer accompanied by the breaking and formation of Zn–O bonds;

(4) Nucleation and growth of metallic zinc grains, or precipitation/dissolution of ZnO;

(5) Interfacial morphological and compositional evolution induced by deposition/dissolution.

Under high current densities or mass-transport-limited conditions, the ion concentration near the interface deviates significantly from that in the bulk electrolyte, leading to concentration polarization, which further amplifies the potential shift and local non-uniformity in nucleation. Under different pH values and electrode potentials, the thermodynamic stability regions of Zn, Zn^{2+}, and $ZnO/Zn(OH)_2$ species differ markedly; their relationships can be qualitatively described using a simplified Pourbaix diagram, as shown in Fig. 2.6. [61]

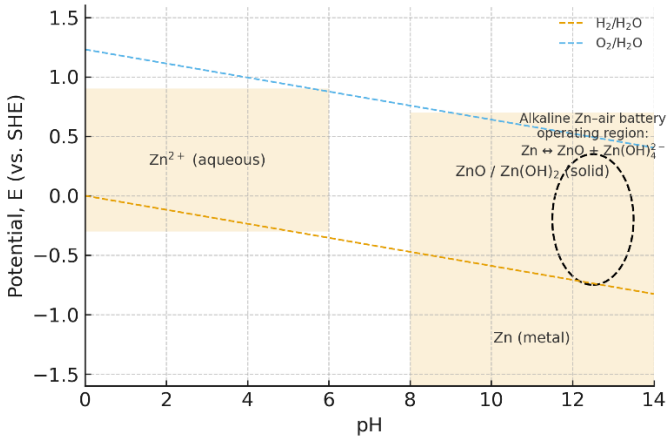

Fig. 2.6 Simplified Pourbaix diagram illustrating the stability regions of zinc species in the $Zn–H_2O–OH^-$ system [56]

As shown in Fig. 2.6, dissolved Zn^{2+} species occupy the main stability region at relatively low pH values and appropriate electrode potentials. Under strongly alkaline conditions, more negative potentials favor the stability of metallic Zn, whereas relatively more positive potentials promote the formation of $ZnO/Zn(OH)_2$ solid phases. The typical operating window of zinc–air batteries using concentrated alkaline electrolytes lies in the region of pH ≈ 13–14 with relatively negative potentials. In this region, the Zn ↔ ZnO transformation is strongly coupled with the dissolution–deposition behavior of $Zn(OH)_4^{2-}$, which jointly governs the interfacial structural evolution of the zinc anode during cycling.

For the air electrode, the diffusion and dissolution of O_2 within the electrode, as well as its reaction behavior at the solid–liquid–gas three-phase interfaces, are of critical importance. In a porous gas diffusion electrode (GDE), the gas channels, electrolyte-filled regions, and solid backbone together form a complex three-phase network. The configuration of the gas diffusion electrode and the associated mass transport pathways can be simplified as illustrated in Fig. 2.7.

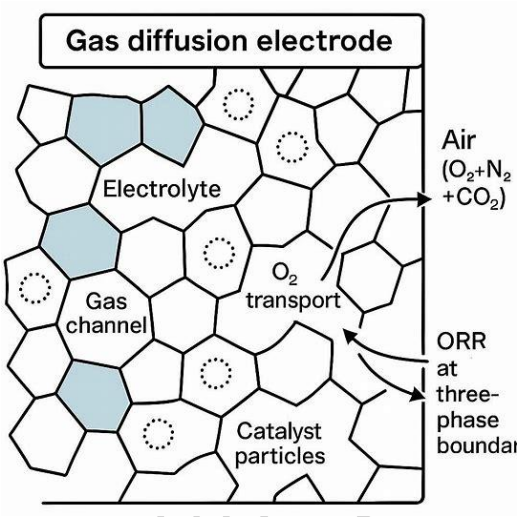

Fig. 2.7 Schematic illustration of gas–liquid–solid three-phase interfaces and O_2 transport pathways in a gas diffusion electrode [62]

As shown in Fig. 2.7, both gas channels that are not wetted by the electrolyte and liquid-filled pores coexist within the porous carbon framework, while catalyst particles loaded on the solid surface provide the active sites for ORR/OER. Oxygen first diffuses along the gas channels inside the gas diffusion layer (GDL), then dissolves into the electrolyte at the gas–liquid interface, and further diffuses to the solid–liquid interface to participate in the electrode reactions. The stability and continuity of the three-phase interfaces directly affect the effective reaction area and mass-transfer resistance, whereas phenomena such as carbonate deposition, electrode flooding, or dry-out can disrupt this structure and lead to a sharp increase in polarization.

In addition, when the alkaline electrolyte is exposed to air, it continuously absorbs CO_2 to form CO_3^{2-}, which combines with K^+ to produce K_2CO_3 that gradually deposits in the electrode and separator. This “carbonate poisoning” process decreases the ionic conductivity of the solution, blocks pores and three-phase interfaces, and thereby increases both ohmic and mass-transport polarization, representing a major challenge for the long-term operation of alkaline zinc–air batteries in open environments.

2.5 Failure mechanisms and structural evolution of the zinc anode during cycling

Although zinc–air batteries theoretically offer high energy density and low material cost, the zinc anode often undergoes pronounced structural degradation and loss of activity during practical electrochemical cycling. The main issues include ZnO passivation, non-uniform deposition, dendrite growth, formation of “dead zinc,” and self-corrosion.

(1) Formation and densification of the ZnO passivation layer

During discharge, as indicated by (2-1) and (2-2), zinc is first converted into soluble $Zn(OH)_4^{2-}$, which subsequently decomposes and precipitates as ZnO in locally supersaturated regions. The initially deposited ZnO usually exhibits a loose and porous morphology, imposing only a limited impact on ion and electron transport. However, as the depth of discharge increases, ZnO continuously accumulates on the surface and gradually becomes denser, forming a "passivation layer" with certain mechanical strength and electrical insulating properties. From the perspective of interfacial morphological evolution, the process from the initial formation to the gradual densification of ZnO on the zinc surface can be divided into several typical stages, as illustrated in Fig. 2.8.

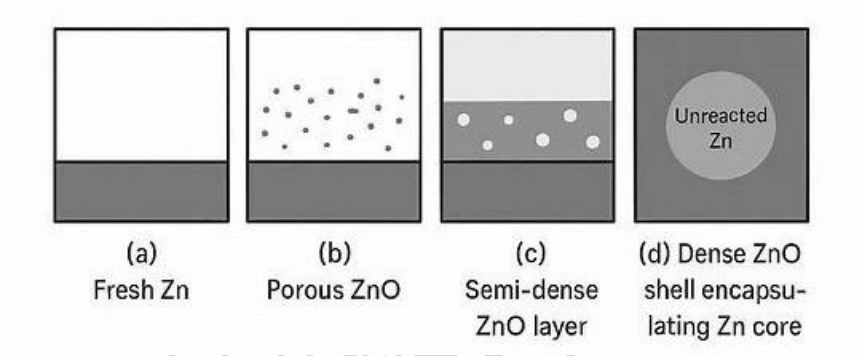

Fig. 2.8 Staged schematic illustration of the formation and densification of the ZnO passivation layer on the zinc anode during discharge [63]

In Fig. 2.8, the zinc surface is initially (a) relatively smooth, with only a few isolated ZnO nuclei. As discharge proceeds, a porous ZnO network gradually forms (b), which still has a limited impact on ion and electron transport. With further discharge, the ZnO layer continues to thicken and its pores are progressively filled (c), eventually evolving into an almost continuous and dense passivation layer (d). On the one hand, this dense layer encapsulates unreacted metallic zinc to form a "core–shell" structure; on the other hand, owing to its low electronic conductivity and poor ionic permeability, it significantly increases the interfacial charge-transfer resistance and induces severe polarization.

The formation of this passivation layer has two main consequences: [64, 65]

a) It reduces the effective contact area between zinc and the electrolyte and increases the interfacial charge-transfer resistance, leading to a pronounced negative shift in potential and aggravated polarization.

b) It hinders the diffusion of $Zn(OH)_4^{2-}$ and OH^-, enlarging the ionic concentration gradients near the interface and further deteriorating the mass-transport conditions.

When the ZnO passivation layer reaches a certain thickness, discharge may terminate prematurely even though unreacted zinc remains inside the electrode, resulting in low capacity utilization and insufficient "apparent capacity."

(2) Local current-density imbalance and uncontrolled deposition morphology

During charging, the redeposition of metallic zinc also exhibits pronounced non-uniformity. Owing to the non-uniform distribution of the interfacial electric field, differences in surface roughness, and the presence of microscopic defects, certain local regions more readily become preferential nucleation sites. This leads to rapid zinc growth at these locations, forming needle-like or dendritic structures and even large, dense deposits of "dead Zn". [10, 66] Such structures not only consume reversibly active material and reduce the effective anode area, but may also, in extreme cases, pierce the separator and cause internal short circuits.

This behavior can also be understood quantitatively from the perspective of local current density. The local current density j_local is related to the total current I and the electrochemically active area A by:

$$j\_local = I / A \qquad (2-11)$$

where j_local (local current density) is the local current density, I (current) is the total current, and A (electrochemically active area) is the effective area participating in the electrochemical reactions (Newman and Balsara, 2021). When a planar current collector is used or the interface is gradually covered by dense ZnO/dead zinc, the effective area actually involved in the reactions is significantly reduced. Under a constant total current, this leads to an increase in the local current density per unit area. A high j_local has two consequences: (1) it causes an excessive negative shift of the interfacial potential, promoting preferential nucleation of $Zn(OH)_4^{2-}$ at local sites and accelerating morphological instability; (2) it greatly increases the local ion-consumption rate, resulting in concentration polarization and steep ion concentration gradients, which further bias zinc deposition toward a few regions and thus lead to dendritic tips and blocky "island-like" deposits.

(3) Volume changes and mechanical damage

There is a significant difference in density and molar volume between metallic zinc and ZnO. During repeated discharge (Zn → ZnO) and charge (ZnO → Zn) processes, the interior of the anode undergoes cyclic volume expansion and contraction. This periodic volume change causes localized mechanical stress concentration and the formation of microcracks, leading to:

a) progressive loosening of the contact between zinc and the current collector, and an increase in interfacial contact resistance;

b) detachment or pulverization of ZnO, with some particles losing their electronic pathways and further evolving into "dead zinc";

c) gradual loosening and powdering of the overall electrode structure, making it difficult to maintain a stable three-dimensional conductive network.

(4) Self-corrosion and side reactions

In alkaline electrolytes, zinc undergoes significant self-corrosion, which essentially involves its reaction with water and the synergistic effects of dissolved oxygen and impurity ions. For example:

$$Zn + 2H_2O \rightleftharpoons Zn(OH)_2 + H_2\uparrow \qquad (2-12)$$

Self-corrosion not only consumes active zinc and generates hydrogen gas, posing safety hazards, but also disrupts the original electrochemical uniformity of the anode surface, inducing local current concentration and further aggravating non-uniform deposition and dendrite formation. In addition, heterogeneous metallic impurities and Fe^{3+}/Fe^{2+} ions can act as micro-galvanic corrosion centers, accelerating the self-discharge rate. The self-corrosion and hydrogen evolution processes of the zinc anode in alkaline electrolyte are schematically illustrated in Fig. 2.9.

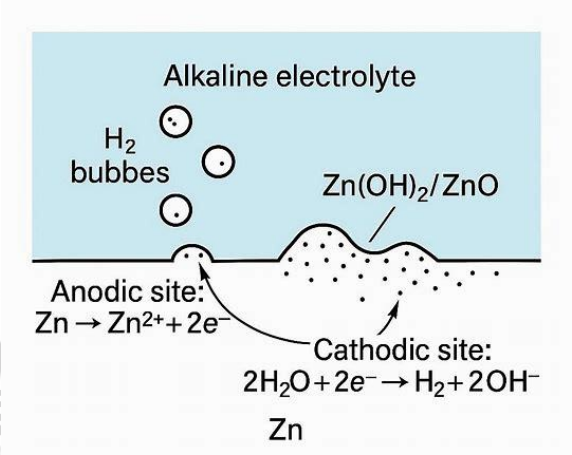

Fig. 2.9 Schematic illustration of self-corrosion and hydrogen evolution on the zinc anode in alkaline electrolyte [10]

As shown in Fig. 2.9, numerous micro-galvanic cells are formed on the zinc surface during self-corrosion. Some local regions act as anodic sites where zinc dissolves to generate Zn^{2+}, while other regions serve as cathodic sites where water is reduced and H_2 bubbles are produced. The resulting $Zn(OH)_2$/ZnO particles tend to deposit locally, rendering the surface rough and heterogeneous. At the same time, the periodic attachment and detachment of gas bubbles further disturb the interfacial electric field and local concentration distribution. These effects not only reduce the effective utilization of active zinc, but also lay the groundwork for non-uniform nucleation and dendrite growth of zinc during subsequent charging. Considering the combined influences of passivation, self-corrosion, dendrite formation, and volume changes, the morphological evolution of the zinc anode over multiple charge–discharge cycles can be summarized by the typical pathway illustrated in Fig. 2.10.

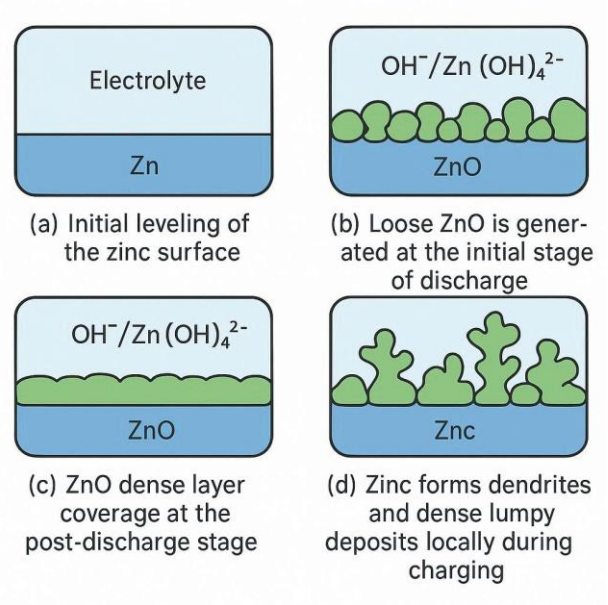

Fig. 2.10 Schematic illustration of interfacial structural evolution of the zinc anode during cycling [58]

In summary, the failure of the zinc anode is a complex, coupled process jointly driven by thermodynamic, kinetic, and mechanical factors. The multiscale structural evolution that the anode undergoes during repeated charge–discharge cycles constitutes one of the key bottlenecks limiting the long-term cycling stability of rechargeable zinc–air batteries.

2.6 Mechanistic advantages of 3D Ni foam/electrodeposited zing composite anodes

To address the aforementioned issues of non-uniform deposition and structural degradation, introducing a three-dimensional (3D) porous conductive framework and constructing a high–specific-surface-area electrodeposited zinc layer on it is regarded as an effective strategy. Compared with conventional planar current collectors, Ni foam/Zn composite anodes exhibit several fundamental advantages, which are mainly reflected in the following aspects:

(1) Significantly enlarged electrochemically active area and reduced local current density

Three-dimensional Ni foam possesses high porosity and a complex network of interconnected pores, giving it a real specific surface area far greater than its geometric projected area. Under the same total current, the effective area A is greatly increased, thereby markedly reducing the average local current density j_local (Eq. (2-11)), which in turn:

a) mitigates the accumulation of local overpotential and suppresses extremely fast nucleation and dendrite growth at a few preferential sites;

b) delays the formation of a continuous and dense ZnO layer and the onset of the “coverage–blocking” process, allowing more internal zinc to participate in the reactions and thus improving capacity utilization. [47, 53]

(2) Optimized transport pathways for ions and reactants

The 3D porous structure provides abundant channels for electrolyte penetration and for the migration of $Zn(OH)_4^{2-}/OH^-$, which helps alleviate concentration polarization inside the electrode. During charge–discharge cycling, the foam structure can distribute current and ion flux more uniformly on the micrometer-to-hundred-micrometer scale, thereby reducing deposition segregation caused by local mass-transport limitations and enabling more homogeneous zinc deposition/dissolution.

(3) Enhanced mechanical support and buffering of volume changes

The Ni foam framework itself has high mechanical strength and good plasticity, serving as a "skeleton support" during zinc deposition and dissolution. Throughout repeated volume expansion/contraction, Ni foam can effectively buffer stress concentration, slowing down the cracking, delamination, and pulverization of the zinc layer and thus stabilizing the anode structure. Meanwhile, the nickel surface generally shows good wettability and affinity toward zinc, which facilitates the formation of a tightly adhered zinc layer and reduces the formation of "dead zinc." [67, 68]

(4) Electric-field homogenization and regulation of nucleation sites

In a 3D conductive network, current is distributed along multiple pathways, making it easier to homogenize the local electric field. By rationally designing the pore-size distribution, ligament thickness, and surface microstructure of Ni foam, and by tuning the electrodeposition parameters (such as current density, deposition time, electrolyte composition, and additives), it is possible to engineer the nucleation density and preferential nucleation sites of zinc. This enables the formation of fine and uniform grains and a continuous, dense yet porous zinc layer. Such a structure is beneficial not only for uniform $Zn \rightarrow Zn(OH)_4^{2-}/ZnO$ formation during discharge, but also for uniform redeposition of metallic zinc during charging. [69]

The differences in local current-density distribution between planar current collectors and 3D Ni foam current collectors can be qualitatively compared using the schematic illustration shown in Fig. 2.11.

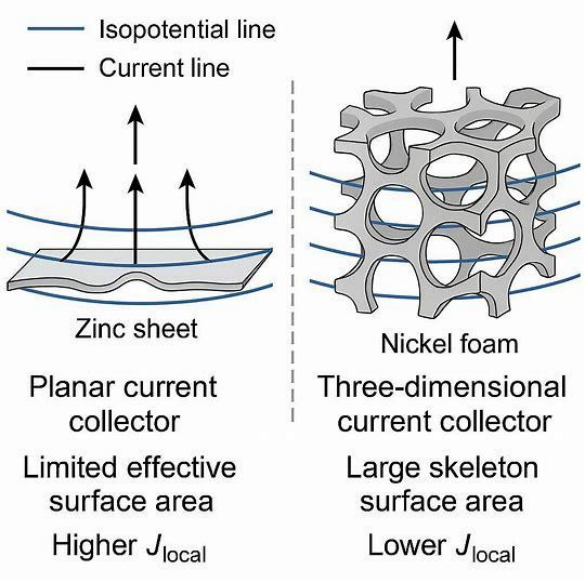

Fig. 2.11 Schematic comparison of local current distribution between planar and three-dimensional current collectors [62]

In Fig. 2.11 (a), the local current density on the surface of a planar current collector is clearly concentrated at the edges or minor protrusions, as indicated by the uneven arrow lengths. This implies that, under a fixed total current, the electrochemically active area actually involved in the reaction is limited, making it easy to generate regions with very high j_local and excessively negative interfacial potentials at only a few sites. In contrast, as shown in Fig. 2.11 (b), the three-dimensional Ni foam current collector, owing to its high specific surface area and interconnected porous network, can greatly increase the effective area A_eff and uniformly distribute the current pathways, thereby making the local current density much more homogeneous in space. Such current-homogenization effects are beneficial for suppressing uncontrolled zinc nucleation and dendrite growth and for delaying the continuous densification of the ZnO passivation layer. They constitute an important structural basis for constructing highly stable zinc anodes.

2.7 Relationship with electrodeposition theory and quantitative description

From the viewpoint of electrochemical reactions, the redeposition of zinc on the anode during charging is highly analogous to a conventional electrodeposition process and can be quantitatively described by Faraday's law. For the Zn^{2+}/Zn system, the half-reactions can be written as: [18, 70]

Cathode (deposition):

$$Zn^{2+} + 2e^{-} \rightarrow Zn(s) \qquad (2-13)$$

Anode (dissolution):

$$Zn(s) \rightarrow Zn^{2+} + 2e^{-} \qquad (2-14)$$

Under galvanostatic conditions, the electric charge Q passing through the electrode per unit time is given by Q = I·t, and its relationship with the amount of deposited zinc can be described by Faraday's law:

$$m = M\,I\,t\,/\,(nF) \qquad (2-15)$$

where m is the deposited mass, M is the molar mass of zinc, n = 2 is the number of electrons transferred for the Zn^{2+}/Zn couple, F is the Faraday constant, I is the current, and t is the deposition time (in seconds or hours). The average film thickness h can then be expressed as:

$$h = m\,/\,(\rho \cdot A) \qquad (2-16)$$

where ρ is the density of zinc and A is the plated area of the substrate. It is thus evident that, under constant current and fixed geometric conditions, the deposition time t is approximately linearly correlated with the zinc loading/average thickness. [67]

Based on the above principles, this study adopts a simple and well-controlled two-electrode electrodeposition configuration: three-dimensional Ni foam is used as the cathode as well as the supporting substrate, a high-purity metallic zinc sheet is employed as the consumable anode, and an aqueous $ZnSO_4 \cdot 7H_2O$ solution is used as the electrolyte, as illustrated in Fig. 2-12

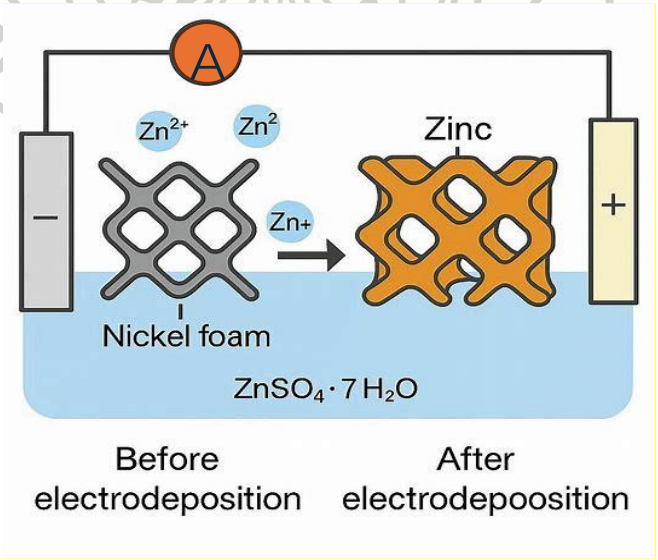

Fig. 2.12 Schematic illustration of zinc electrodeposition on Ni foam in $ZnSO_4 \cdot 7H_2O$ electrolyte [34]

As shown in Fig. 2.12, in this relatively mild, compositionally simple, and Zn^{2+}-concentration-stable $ZnSO_4$ system, zinc at the anode continuously dissolves into Zn^{2+}, while Zn^{2+} is

electrochemically reduced and deposited onto the Ni foam cathode, thereby constructing a continuous metallic zinc layer on the three-dimensional framework. By precisely adjusting the plating time under constant current and fixed geometric conditions, the deposition mass and average film thickness of zinc can be tuned in an approximately linear manner, enabling the preparation of a series of samples ranging from low to high loading. On this basis, the effects of different zinc loadings on the discharge capacity, rate performance, and cycling stability of zinc–air batteries can be systematically evaluated [14]

In such a mild $ZnSO_4$ electrolyte, controllable electrodeposition of zinc on Ni foam can thus be achieved, and by varying the deposition time under galvanostatic conditions and fixed geometry, the deposited amount and average thickness can be effectively regulated, allowing a systematic investigation of how different zinc loadings influence the electrochemical performance of zinc–air batteries.

2.8 Literature reviews on zinc-air battery anodes

The overall performance of zinc–air batteries is largely governed by the behavior of the anode, and thus research focusing on the structural design and failure mechanisms of zinc anodes has become one of the core topics in this field. According to the existing literature, anode systems can be broadly classified into several categories: conventional planar anodes represented by zinc foil and pressed zinc powder; self-supporting zinc structures such as porous zinc and zinc sponge; and composite zinc anodes that employ three-dimensional current collectors (e.g., Ni foam, Cu foam, porous carbon frameworks) as substrates.

To address typical issues such as morphological evolution during discharge, ZnO passivation, dendrite growth, and the accumulation of “dead zinc,” researchers have proposed modification strategies from multiple perspectives. These include regulating the zinc dissolution/deposition behavior through alloying (e.g., Zn–Al, Zn–Bi, Zn–In), constructing protective interfaces using polymer or electrolyte membranes, inorganic oxides, or carbon-based coatings, introducing organic/inorganic electrolyte additives to suppress corrosion and side reactions, and employing three-dimensional porous current collectors to disperse local current density and guide uniform zinc deposition within the scaffold. Overall, three-dimensionally structured anodes and electrodeposited zinc composite anodes have gradually become research hotspots for suppressing dendrites, enhancing reversibility, and extending cycle life.

In the following sections, the material systems, structural characteristics, and application performance of different types of zinc anodes in zinc–air batteries will be systematically reviewed and discussed.

Wang et al. [71] addressed a key bottleneck of flexible zinc–air batteries—namely the mismatch between anode structure and electrolyte form—by proposing a synergistic design strategy based on a “3D foam zinc anode + PVA–TEAOH–KOH hydrogel electrolyte.” The authors first used three-dimensional porous Cu foam as the substrate and deposited zinc by galvanostatic electroplating in an

electrolyte containing $ZnSO_4$, $Al_2(SO_4)_3$, and $KAl(SO_4)_2$, thereby obtaining Zn-coated foam electrodes with different pore densities (130, 40, and 25 PPI). In this way, they constructed three-dimensional foam anodes with high specific surface area, high zinc loading, and a continuous conductive backbone. Subsequently, they prepared a PVA–TEAOH–KOH composite hydrogel electrolyte and optimized the TEAOH/KOH mass ratio to balance ionic conductivity and water retention: TEAOH improved the water-holding capability and chemical stability of the hydrogel, while KOH provided high ionic conductivity. A composition with TEAOH:KOH = 2:1 was finally identified as the optimal compromise, achieving an ionic conductivity on the order of 10^2 $mS \cdot cm^{-1}$ together with good dimensional stability.

In terms of cell configuration, the authors used the Zn-coated foam as the anode and a Co_3O_4/carbon cloth electrode as the air cathode, with an in situ cross-linked hydrogel electrolyte sandwiched between them, thereby constructing a flexible zinc–air battery that can be bent and rolled. Under ambient conditions, they systematically evaluated its polarization curves, specific capacity, energy density, and charge–discharge cycling stability. The results show that the 130 PPI foam anode delivers the best discharge power density and rate performance; the hydrogel maintains its structural integrity after repeated bending and prolonged cycling, and the battery can still output stably under mechanical deformation. These findings indicate that the good matching between the three-dimensional foam anode and the gel electrolyte not only improves interfacial contact and ionic transport efficiency, but also significantly enhances device flexibility and environmental adaptability, providing a valuable integrated materials–structure design strategy for high-performance flexible zinc–air batteries.

Qu *et al.* [72] significantly enhanced the cycling stability and lifetime of zinc–air batteries by employing an air electrode with an inverted configuration. Conventional zinc–air batteries often suffer from zinc dendrite growth, coverage of the air-electrode catalyst layer by zinc oxide, electrode flooding, and catalyst loss during charge–discharge cycling, all of which hinder their commercial viability. In this work, the authors innovatively oriented the Ni foam side of the air electrode toward the zinc anode. By exploiting the hydrogen evolution reaction induced at the Zn–Ni contact, they effectively suppressed zinc dendrite growth and prevented zinc-containing discharge products from contaminating the oxygen-reduction catalyst layer.

Experimental results show that a primary zinc–air battery using this inverted air electrode can deliver more than 1000 h of stable discharge at a current density of 0.1 mA cm^{-2}, with the discharge voltage maintained above 1.35 V. Under these conditions, the capacity and specific energy reach 728 mA h g^{-1} and 874 W h kg^{-1}, respectively. In the rechargeable configuration, the same electrode architecture also exhibits excellent cycling stability: at 10 mA cm^{-2}, the cell operates for over 700 h without short-circuit, with a Coulombic efficiency close to 100% and a round-trip efficiency exceeding 70%. Furthermore, the study demonstrates the potential of this inverted-air-electrode design in solid-state zinc–air batteries; by optimizing the interfacial contact between the electrodes and gel electrolyte, the authors further extend its applicability to flexible electronic devices.

Xu *et al*. [73] proposed an anode-free zinc battery design strategy based on a "zinc-affinitive three-dimensional nano-copper host (ZA@3D-nanoCu) + zero initial metallic zinc." In their work, $Cu(OH)_2$ nanowires were grown in situ on a copper foil and then subjected to calcination–reduction and rapid thermal shock treatment to construct a mechanically robust three-dimensional nano-copper framework. Subsequently, antimony nanoparticles were loaded onto this framework via pulse electrodeposition, yielding a ZA@3D-nanoCu current collector that combines a three-dimensional conductive network with uniformly distributed zinc-affinitive sites. Structural and compositional characterizations (SEM, XRD, XPS) show that Sb nanoparticles are homogeneously dispersed on the nano-copper skeleton and form alloys with Zn, which helps reduce the nucleation overpotential and strengthen Zn–substrate adhesion.

Based on COMSOL multiphysics simulations, the authors compared the electric-field distribution and morphological evolution of zinc deposition on bare Cu foil and on ZA@3D-nanoCu. On planar Cu, the local current density is highly concentrated and evolves into severe dendritic growth over time, whereas on ZA@3D-nanoCu the current distribution remains uniform and zinc deposition stays dense and smooth, achieving dendrite-free electrodeposition. Electrochemical tests reveal that, at an areal capacity of 2 $mAh \cdot cm^{-2}$, ZA@3D-nanoCu|Zn half-cells can cycle stably for more than 1100 h at 4 $mA \cdot cm^{-2}$, and they still maintain stable operation for 600 h at a higher areal capacity of 5 $mAh \cdot cm^{-2}$, which is markedly superior to bare Cu|Zn systems. Furthermore, by pairing ZA@3D-nanoCu with bromine and MnO_2 cathodes to construct anode-free full cells, the Zn–Br_2 battery achieves 1000 cycles at 10 $mAh \cdot cm^{-2}$ with nearly 99% capacity retention, and a 200 mAh pouch cell maintains a Coulombic efficiency above 96%. These results demonstrate the strong application potential of this zinc-affinitive 3D host in high-energy-density, long-lifetime anode-free zinc batteries.

Deckenbach *et al*. [53] prepared a ZnO/C composite anode material by pyrolyzing the metal–organic framework MOF-5, in which nanosized ZnO particles are uniformly embedded in a carbon matrix with a hierarchical pore structure. In 4 M KOH electrolyte, this composite anode exhibits excellent electrochemical performance: the peak discharge capacity reaches 267 $mAh\ g^{-1}$ and the average discharge capacity is 207 $mAh\ g^{-1}$, corresponding to a zinc utilization of 25.3%, which is much higher than that of conventional zinc foil and zinc powder anodes. The cell remains stable over 60 cycles without observable zinc dendrite formation, and the overall Coulombic efficiency reaches 83%. The study indicates that the carbon matrix not only provides electronic conduction pathways and ion-transport channels, but also effectively suppresses ZnO dissolution and electrode passivation.

In addition, the authors developed an easy-to-assemble zinc–air test cell that enables precise evaluation of zinc utilization and cycling performance. By means of structural design, the ZnO/C composite anode realizes highly efficient utilization and reversible transformation of zinc species, offering a new approach for the development of high-energy-density, long-lifetime rechargeable zinc–air batteries.

He *et al*. [74] employed magnetron sputtering to introduce nitrogen doping (NC) onto carbon cloth, thereby constructing a three-dimensional host material with high zinc affinity to direct uniform

zinc nucleation and suppress dendrite growth. The study shows that nitrogen doping, especially pyrrolic nitrogen, can significantly enhance the interaction between the carbon matrix and zinc atoms, with the binding energy increasing from −0.87 eV to −3.30 eV. This effectively reduces the zinc nucleation overpotential (to 49.3 mV) and increases the exchange current density (to 0.50 mA cm^{-2}). Theoretical calculations further confirm that the NC surface can accelerate the desolvation of Zn^{2+}, lower the ion migration energy barrier, and promote uniform distribution and rapid deposition of zinc ions.

Electrochemical tests demonstrate that zinc symmetric cells based on NC can cycle stably for more than 220 cycles with an overpotential of only 11 mV, while Zn||NC half-cells maintain a Coulombic efficiency of 98.8% after 500 cycles at 0.2 mA cm^{-2}. The assembled zinc–air full cells also exhibit excellent cycling stability (>430 cycles) and a high specific capacity of 429 mAh g^{-1}. This work not only elucidates the mechanistic role of surface chemical regulation in zinc deposition kinetics, but also provides a new strategy for developing high-performance, flexible zinc–air batteries.

Yuan *et al.* [46] proposed a rather unique dendrite-suppression strategy from the perspective of interfacial energy anisotropy: by introducing Mg, Ce, and Yb into zinc anodes via alloying, they tuned both the anisotropy modulus and intensity of the interfacial energy at the Zn electrode, thereby weakening the driving force for sustained dendrite growth at the level of crystal-growth thermodynamics. The authors first established a 2D phase-field model, in which the interfacial energy anisotropy (IEA) parameters were incorporated into the phase-field equation, the Zn^{2+} diffusion equation, and the potential-evolution equation. They systematically simulated the evolution of dendrite morphology, potential distribution, and Zn^{2+} concentration gradients during charging, and showed that dendrite height increases monotonically with charging time, while the concentration and potential gradients at the dendrite tip constitute the key driving forces governing its growth.

On this basis, the authors prepared a series of Zn–Mg, Zn–Ce, and Zn–Yb alloy anodes and carried out galvanostatic charging and SEM characterization in 7 mol·L^{-1} KOH + saturated ZnO electrolyte. The results indicate that the introduction of Ce and Mg increases the anisotropy modulus of the interfacial energy; when the modulus is raised to 6, the suppression rate of dendrite height can reach 35%, and the dendrites evolve from a single main trunk into multi-directional branches, leading to a significant reduction in overall height. In contrast, the introduction of Yb reduces the IEA intensity and refines the grain size, rendering the anode surface denser and smoother; the dendrite morphology gradually transforms from a network-like structure into spherical/particulate deposits, again with a notable decrease in height. The optimal compositions were identified as 98%Zn–2%Mg and 93.5%Zn–6.5%Yb.

By tightly integrating phase-field simulations with alloy-experiment studies and establishing a clear correlation between “interfacial anisotropy” and “dendrite morphology,” this work provides a quantitative mechanism for dendrite suppression. It offers valuable theoretical guidance and materials-design strategies for engineering alloyed zinc anodes for zinc–air batteries to achieve dendrite-free, long-lifetime cycling through trace alloying.

CHAPTER 3
EXPERIMENTAL SETUP

In the previous chapter, the working mechanism of zinc–air batteries, the theoretical aspects of the electrodeposition process, and the mechanistic advantages of three-dimensional Ni foam/electrodeposited zinc composite anodes were systematically discussed. In the present chapter, the focus shifts to the experimental aspects. Specifically, the materials and reagents used in this study, the pretreatment procedures for the Ni foam substrates, the setup and operating steps for electrochemically depositing zinc anodes, the assembly process of zinc–air batteries, as well as the detailed conditions for physical characterization and electrochemical performance testing are described in detail.

To establish a complete logical chain from "theoretical analysis → sample preparation → cell assembly → performance testing → result discussion," this chapter first presents a schematic diagram of the experimental workflow adopted in this study, and then provides a step-by-step description in the order of materials selection, substrate treatment, electrodeposition, cell assembly, and testing procedures. The overall experimental workflow is illustrated in Fig. 3.1.

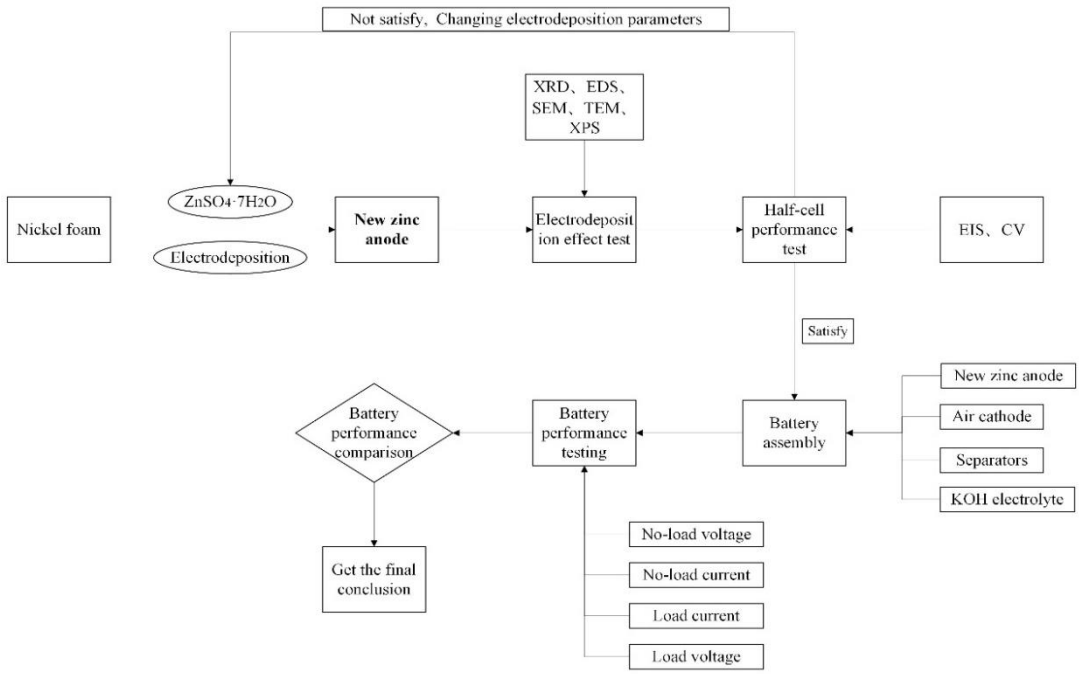

Fig. 3.1 Schematic flowchart of the electrodeposition process

As shown in Fig. 3.1, the experimental procedure consists sequentially of Ni foam substrate pretreatment, electrochemical deposition of the zinc layer, sample drying and weighing, battery assembly, and physical characterization combined with electrochemical performance testing. The subsequent sections will elaborate on these key steps in accordance with this workflow.

To provide an intuitive overview of the main instruments and equipment used in this study, Fig. 3.2 presents photographs of the electrochemical workstation, ultrasonic cleaner, vacuum drying oven, magnetic stirrer, and digital multimeter/data acquisition system.

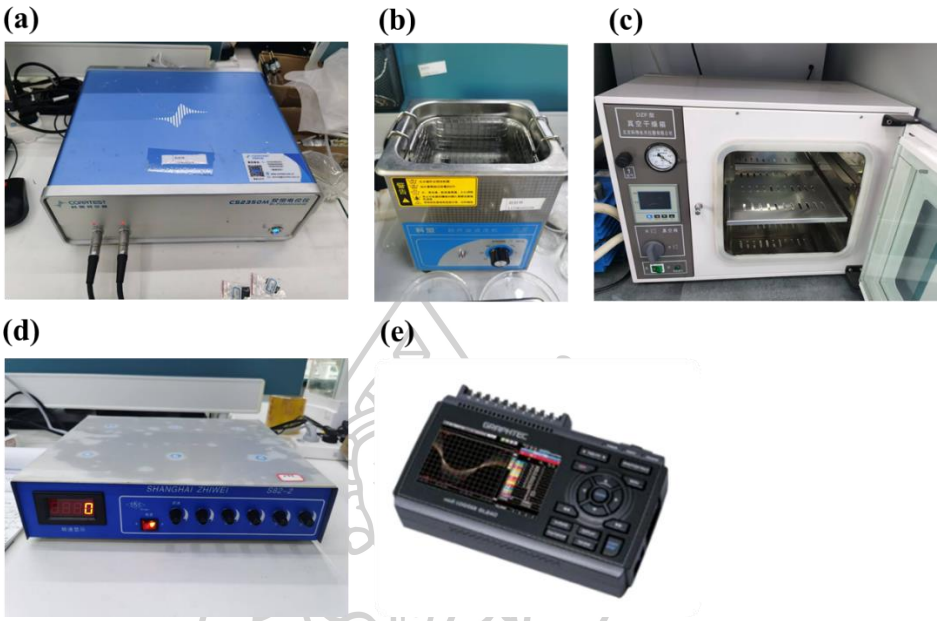

Fig. 3.2 Photographs of the main experimental instruments and equipment used in this study. (a) electrochemical workstation; (b) ultrasonic cleaner; (c) vacuum drying oven; (d) magnetic stirrer; (e) digital multimeter and data acquisition system

3.1 Materials

All reagents used in this study were of analytical grade (AR) and were used as received without further purification. Deionized water (resistivity > 18.2 MΩ·cm) was prepared in situ by an ultrapure water system and used freshly to minimize the risk of secondary contamination. The main materials and their uses are summarized as follows:

(1) Ni foam substrate

Commercial nickel foam (thickness 1.5 mm, 100 PPI, Kunshan Xingzhenghong Battery Materials Co., Ltd.) was used as the three-dimensional porous current collector. Since the as-received Ni foam surface contained a small amount of oxides and oily contaminants, a pretreatment process was required for their removal.

(2) Metallic zinc counter electrode and reference anode

A high-purity zinc sheet (mass fraction ≥ 99.9%, thickness ≈ 2 mm) was used as the counter electrode during electrodeposition. For the control cells, a pure zinc plate with dimensions of 35 × 60 mm and a thickness of 2 mm was employed as the anode to compare the performance differences between pure Zn anodes and Zn/Ni foam composite anodes.

(3) Components of the electrodeposition electrolyte

The electrodeposition electrolyte consisted of an aqueous solution of 0.5 mol L^{-1} zinc sulfate heptahydrate ($ZnSO_4 \cdot 7H_2O$, analytical grade, purity ≥ 98.5%) prepared with deionized water. During preparation, the calculated amount of $ZnSO_4 \cdot 7H_2O$ was first dissolved in approximately 80% of the final water volume; after complete dissolution, the solution was diluted to the desired volume and then left to stand at room temperature to remove air bubbles before use.

(4) Components of the zinc–air battery electrolyte

A 6 mol L^{-1} KOH aqueous solution was used as the electrolyte for zinc–air batteries. It was prepared by dissolving KOH pellets (mass fraction 85%, analytical grade) in deionized water. An ice-water bath was employed during preparation to control the temperature rise of the solution and avoid local overheating.

(5) Air electrode materials

A high–specific-surface-area carbon plate (10 × 60 mm, purity 99%) was used as the support for the air electrode, onto which a commercial Pt catalyst (e.g., 20 wt% Pt/C) was loaded. The catalyst ink was uniformly applied by conventional spraying or doctor-blading methods, and a continuous catalyst layer was obtained after drying.

(6) Separator material

A glass fiber filter membrane (GF/C, diameter 47 mm) was used as the separator. Before cell assembly, the separator was soaked in the 6 mol L^{-1} KOH electrolyte for at least 30 min to ensure full wetting.

(7) Cleaning and auxiliary materials

Absolute ethanol (purity 99.8%, analytical grade) was used for degreasing and to accelerate drying. Hydrochloric acid (HCl, mass fraction 35 wt%) was used for acid pickling and activation of the Ni foam. Neutral detergent and lint-free wipes were used to remove machining oils. In addition, customized acrylic plates (60 × 70 × 15 mm), 0.5 mm thick silicone gaskets, stainless-steel bolts and nuts, electrical insulation gaskets, wires, and clamps were employed to construct the cell housing and to achieve external electrical connections.

The key materials involved in this study are shown in Fig. 3.3.

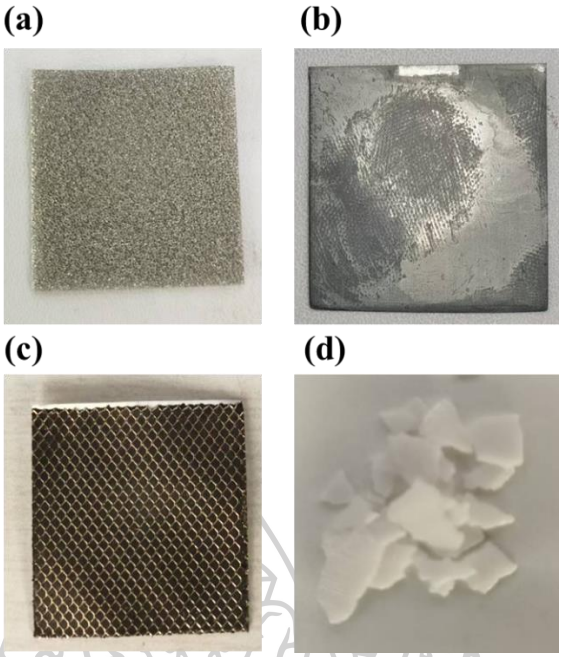

Fig. 3.3 Photographs of selected key materials used in this study. (a) Ni foam substrate; (b) pure zinc plate and zinc counter electrode; (c) carbon plate support for the air electrode; (d) glass fiber separator and KOH pellets

3.2 Pretreatment of Ni foam substrate

To obtain a clean, active, and reproducible three-dimensional current collector substrate, a standardized pretreatment procedure was applied to the commercial Ni foam. The main steps included cutting, acid pickling with ultrasonication, multi-step rinsing with deionized water, ultrasonic degreasing with ethanol, drying, and initial weighing.

3.2.1 Mechanical cutting and initial cleaning

First, the commercial Ni foam was cut into pieces with dimensions of 35 × 60 mm using stainless-steel scissors or a mini cutting machine. During cutting, mechanical compression was minimized to avoid severe collapse of the porous structure. The cut samples were then placed in a beaker containing deionized water and gently shaken to remove visible metallic debris and powders from the surface, while samples showing obvious deformation or severely clogged pores were discarded.

3.2.2 Acid activation and multi-step rinsing

Hydrochloric acid (35 wt%) and deionized water were mixed at a volume ratio of 1:2 to prepare the pickling solution in a beaker. The Ni foam pieces were fully immersed in the acid solution and subjected to ultrasonication at a frequency of about 40 kHz for 15 min. The acid pickling process effectively removed the native oxide layer and part of the metallic impurities from the surface, and slightly etched the Ni foam to increase its surface roughness and activity. The actual state of the Ni foam in the acid solution during pickling is shown in Fig. 3.4.

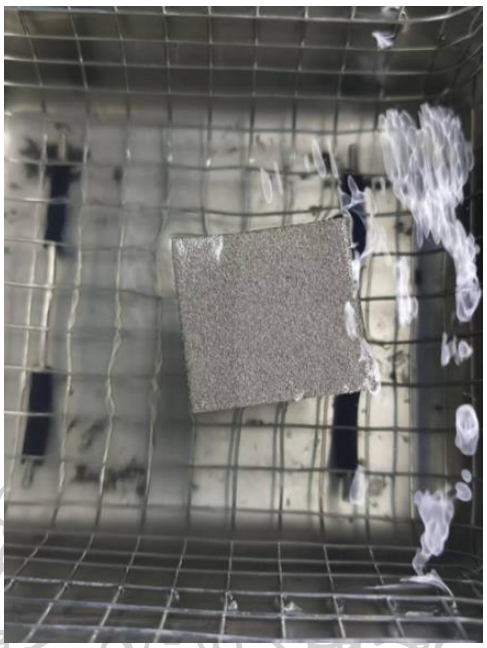

Fig. 3.4 Photograph of Ni foam undergoing ultrasonic acid pickling in an HCl/water mixed solution

After acid pickling, the samples were immediately transferred with tweezers into deionized water for thorough rinsing. They were then placed successively into three fresh deionized-water baths, in each of which they were gently agitated or ultrasonically cleaned for 5 min to completely remove residual acid and dissolved metal ions attached to the Ni foam surface, until the pH of the rinsing solution approached neutrality.

3.2.3 Ethanol degreasing, drying, and weighing

The water-rinsed samples were transferred into a beaker containing absolute ethanol and ultrasonically treated for 15 min to remove residual oils and organic contaminants, while also taking advantage of the high volatility of ethanol to accelerate subsequent drying.

Thereafter, the pretreated Ni foam samples were placed on filter paper or lint-free wipes to drain off surface solvent naturally, and then laid flat in an oven and dried at 60 °C for 12 h. After drying, the samples were taken out, allowed to cool to room temperature (approximately 30 min), and weighed using a precision balance (accuracy ±0.0001 g). The mass of each sample was recorded as m_0. During weighing, direct hand contact with the samples was avoided; plastic tweezers were used to prevent recontamination.

The individual steps and key parameters involved in the Ni foam pretreatment process are summarized in the flowchart shown in Fig. 3.5.

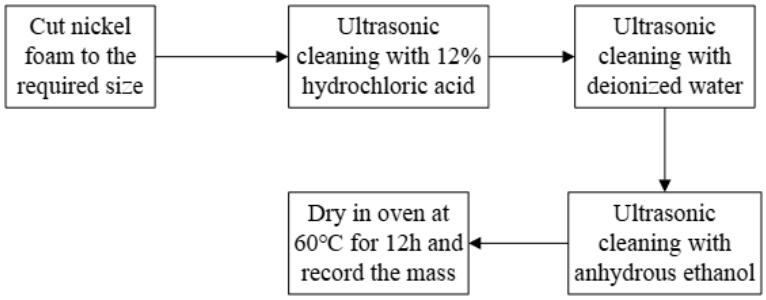

Fig. 3.5 Flowchart of the pretreatment procedure for Ni foam substrates

3.3 Electrodeposition of Zn Anodes

In this study, metallic zinc was deposited onto three-dimensional Ni foam substrates by a galvanostatic electrodeposition method to construct Zn/Ni foam composite anodes. The electrodeposition setup consisted of an electrochemical workstation, a beaker containing the electrolyte, electrode holders, and a magnetic stirrer.

3.3.1 Configuration of the electrodeposition system and electrode connections

Electrodeposition was carried out using a CS2350 electrochemical workstation in an aqueous solution of 0.5 mol L^{-1} $ZnSO_4 \cdot 7H_2O$. A two-electrode configuration was employed:

Working electrode (WE): pretreated Ni foam sheet with dimensions of 35 × 60 mm and a thickness of 1.5 mm.

Counter electrode (CE): high-purity zinc sheet with an area slightly larger than that of the Ni foam, in order to avoid premature polarization.

The electrodes were mounted opposite each other in the beaker with an inter-electrode distance of approximately 20–30 mm. The electrodes were connected to the leads via alligator clips or custom clamps and then connected to the WE and CE terminals of the electrochemical workstation. The beaker was placed on a magnetic stirrer, and the electrolyte volume was controlled in the range of 200–300 mL to ensure that the Zn^{2+} concentration remained relatively stable during deposition. The overall physical layout of the electrodeposition setup is shown in Fig. 3.6.

Fig. 3.6 Photograph of the electrodeposition setup used for preparing Zn/Ni foam composite anodes.

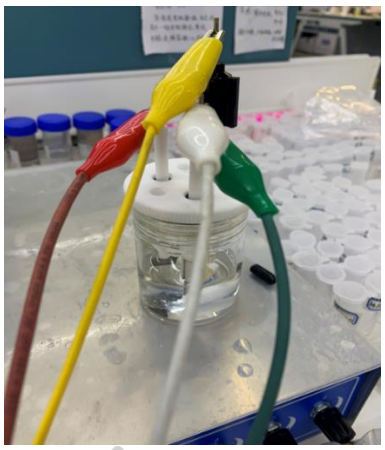

Fig. 3.6 Photograph of the experimental setup for electrodepositing Zn/Ni foam composite anodes

The specific arrangement of the electrodes in the electrolyte and their immersion depth are shown in Fig. 3.7.

Fig. 3.7 Photograph showing the geometric arrangement of the Ni foam working electrode and zinc counter electrode in the electrolyte

3.3.2 Stirring conditions and mass-transport control

To mitigate interfacial concentration polarization and to promptly remove gas bubbles generated during the electrochemical process, magnetic stirring was employed during electrodeposition, with the stirring speed set to 60 rpm. The stir bar was placed at the center of the bottom of the beaker so that the entire electrode region was exposed to a relatively uniform flow field. The fluid streamlines and Zn^{2+} mass transport toward the electrode surface during electrodeposition can be illustrated by a conceptual schematic, as shown in Fig. 3.8.

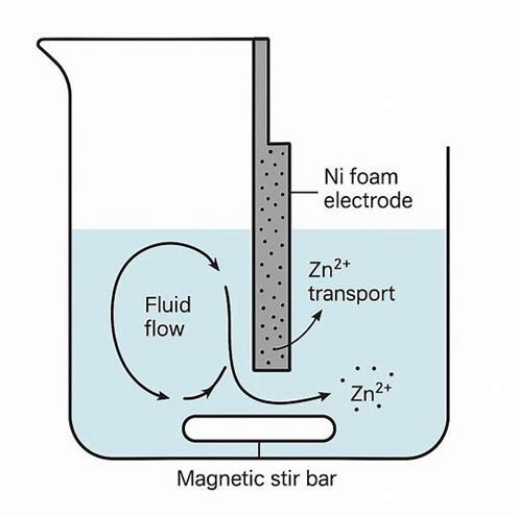

Fig. 3.8 Schematic illustration of fluid streamlines and Zn^{2+} mass transport near the Ni foam surface during electrodeposition [34]

As shown in Fig. 3.8, stirring reduces the thickness of the diffusion layer and promotes the migration of Zn^{2+} toward the surface of the Ni foam skeleton, while also facilitating the detachment of gas bubbles from the electrode surface and preventing the formation of local “dry” regions.

3.3.3 Galvanostatic deposition program and potential response

Electrodeposition was performed at a constant current density of 0.11 A cm^{-2}, calculated with respect to the geometric projected area of the Ni foam. Before initiating deposition, the working electrode was left to stand in the electrolyte for approximately 5 min to ensure full wetting of the interface and the establishment of a stable open-circuit potential. Subsequently, the galvanostatic mode was started, and the variation of the electrode potential with time during deposition was recorded.

A typical potential–time response curve can be divided into an initial nucleation stage, a growth stage with slowly varying potential, and a relatively steady deposition stage, as conceptually illustrated in Fig. 3.9.

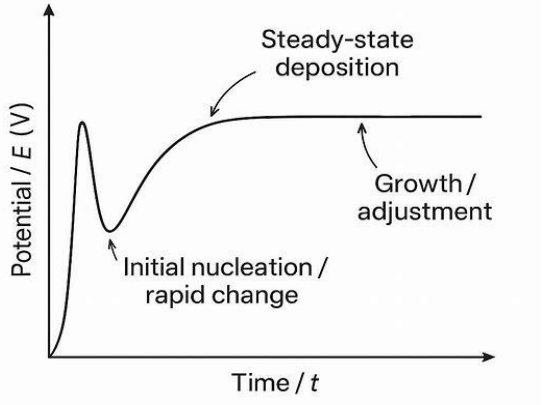

Fig. 3.9 Conceptual schematic of the potential–time curve during galvanostatic electrodeposition

3.3.4 Deposition time gradients and sample nomenclature

To investigate the influence of deposition time on the thickness, morphology, and battery performance of the zinc coating, three deposition-time gradients of 3 h, 4 h, and 5 h were set, and the corresponding samples were denoted as Zn3, Zn4, and Zn5, respectively. For each set of conditions, six parallel samples were prepared to improve statistical reliability. At the end of deposition, the current was immediately switched off, and the Ni foam working electrode was removed from the electrolyte, rinsed thoroughly with deionized water to remove residual electrolyte from the surface, and then rapidly rinsed with absolute ethanol to displace surface water. Thereafter, the samples were placed in a vacuum oven and dried at 60 °C for 12 h. After cooling to room temperature, the mass m_1 of each sample was measured, and the deposited zinc mass was calculated as $\Delta m = m_1 - m_0$. The schematic comparison of the zinc filling degree within the Ni foam skeleton corresponding to the three deposition times is shown in Fig. 3.10.

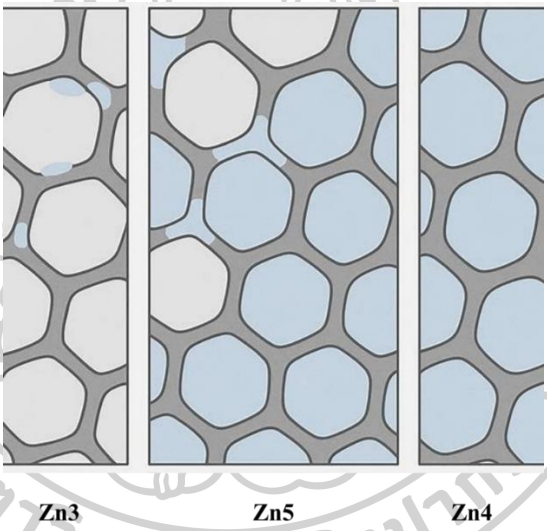

Fig. 3.10 Schematic comparison of zinc filling degrees in the Ni foam skeleton at different deposition times (Zn3, Zn4, and Zn5)

The corresponding macroscopic appearance of the samples can be illustrated by photographs, as shown in Fig. 3.11.

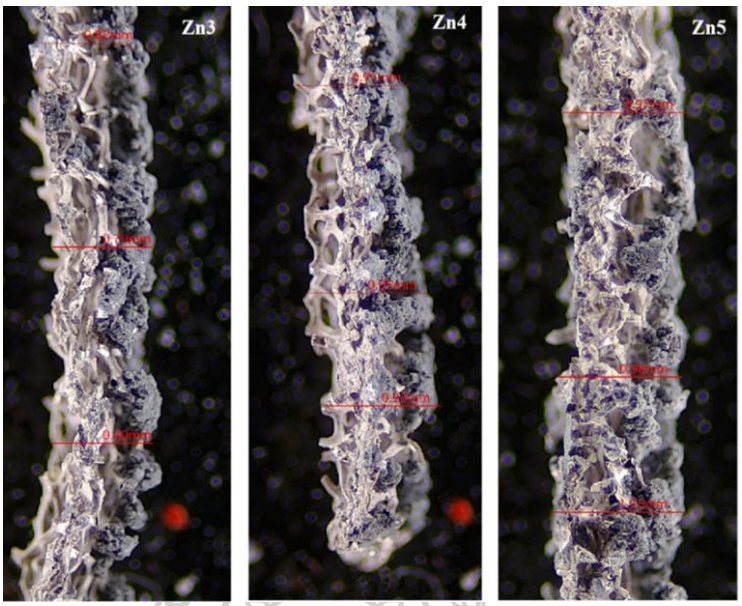

Fig. 3.11 Photographs comparing the macroscopic appearance of Zn3, Zn4, and Zn5 electrodes obtained at different electrodeposition times

3.4 Assembly of Zn–air batteries

In this study, Zn/Ni foam composite anodes prepared at three different electrodeposition times (Zn3, Zn4, and Zn5) were used as the anodes, a high–specific-surface-area carbon plate loaded with a Pt catalyst served as the air cathode, 6 mol L^{-1} KOH aqueous solution was used as the electrolyte, and a glass fiber filter membrane was employed as the separator to assemble zinc–air batteries. For comparison, a control battery (StZnB) was assembled using a pure zinc plate as the anode.

3.4.1 Preparation of cell components

Before assembly, the dried Zn3, Zn4, and Zn5 electrodes were taken out from the vacuum oven and allowed to cool naturally to room temperature. The excess edges of the electrodes were trimmed or adjusted according to the structure of the cell housing to ensure that the effective reaction area was essentially the same, while reserving a reliable region for electrical connection.

For the air electrode, a 10 × 60 mm carbon plate was used, on which a Pt/C catalyst ink was pre-coated and then dried to form a uniform catalytic layer. One side of the air electrode was directly exposed to the ambient air, while the other side was in contact with the electrolyte.

The glass fiber separator was cut into strips or pieces matching the electrode dimensions and soaked in 6 mol L^{-1} KOH electrolyte for at least 30 min to expel air from the pores and ensure complete wetting by the electrolyte.

To provide an intuitive view of the cell components prior to assembly, Fig. 3.12 presents a flat lay photograph of the key parts used in the zinc–air batteries.

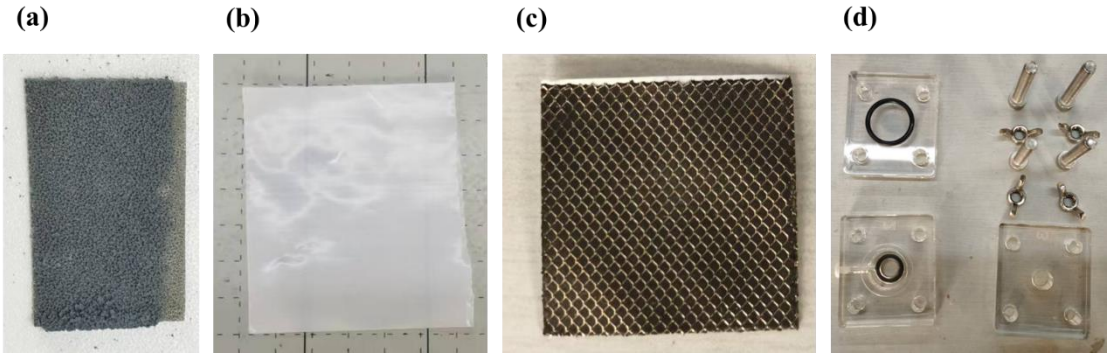

Fig. 3.12 Photographs of the components of the zinc–air battery before assembly. (a) Zn/Ni foam anode; (b) glass fiber separator; (c) Pt/C@carbon plate air cathode; (d) silicone gaskets and acrylic plates; (e) bolts, terminals, and other accessories

3.4.2 Cell housing structure and assembly sequence

The cell housing consisted of three customized acrylic plates (60 × 70 × 15 mm), with a window opened in the middle plate to accommodate the electrodes and electrolyte. A 0.5 mm thick silicone gasket was mounted on the inner side to enhance sealing and prevent electrolyte leakage. During assembly, the components were placed from the bottom upward in the following order: bottom plate silicone gasket, anode, separator pre-wetted with electrolyte, electrolyte, air cathode, and top plate silicone gasket. Stainless-steel bolts were then used to fasten the assembly uniformly around the periphery, ensuring good contact between each layer without excessively crushing the porous structures.

The assembly sequence and spatial arrangement of each component can be illustrated in an exploded-view diagram, as shown in Fig. 3.13.

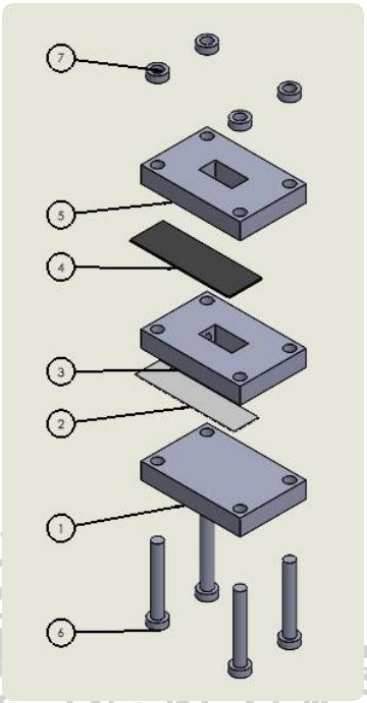

Fig. 3.13 Exploded-view schematic of the zinc–air battery housing structure and assembly sequence.

The macroscopic appearance of the assembled cell is shown in Fig. 3.14.

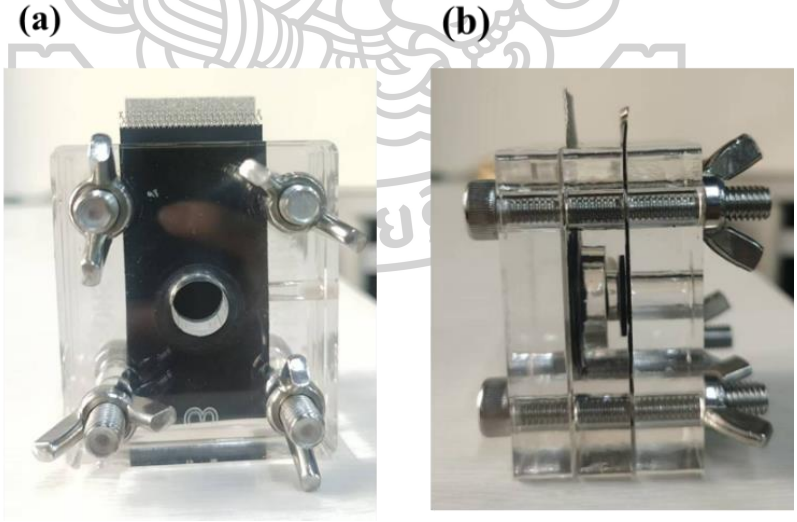

Fig. 3.14 Photographs of the assembled zinc–air battery: (a) front view; (b) side view (indicating the air side and electrolyte side).

The assembled batteries were designated as Zn3B, Zn4B, and Zn5B, corresponding to the Zn3, Zn4, and Zn5 anodes, respectively. Meanwhile, a control battery assembled with a pure zinc plate as the anode and identical other components was denoted as StZnB. After assembly, all cells were left to

stand for approximately 10 min to ensure full penetration of the electrolyte into the electrodes and separator and to allow the interfacial states to reach a relatively stable condition before electrochemical measurements were carried out.

3.5 Physical Characterization and Electrochemical Measurements

3.5.1 Physical characterization methods

To systematically characterize the phase composition, microstructure, elemental distribution, and surface chemical states of the electrodeposited zinc layers, four main techniques were employed in this study: XRD, SEM/EDS, TEM, and XPS.

(1) X-ray diffraction (XRD)

A Rigaku Ultima IV X-ray diffractometer was used to analyze the phases and crystal structures of the samples. The measurement conditions were as follows: Cu Kα radiation (λ = 1.5406 Å), tube voltage 40 kV, tube current 40 mA, scanning range 5°–80°, and scanning rate 8°·min^{-1}. For testing, appropriate portions of the electrode were cut and placed flat on the sample holder, with the zinc layer facing upward and the surface kept as flat as possible.

(2) Scanning electron microscopy (SEM) and energy-dispersive X-ray spectroscopy (EDS)

A Thermo Scientific Apreo 2 SEM was used to observe the surface and cross-sectional morphologies of the zinc coatings, and the attached EDS system was employed to analyze elemental distributions. The typical operating voltage was about 5 kV, and the beam current was about 50 pA. Cross-sectional samples were prepared by cold mounting in resin followed by mechanical polishing.

(3) Transmission electron microscopy (TEM)

A Talos F200S TEM was used to investigate the local nanostructure and crystal defects. TEM specimens were prepared by gently scraping off part of the electrodeposited zinc layer, dispersing the fragments in ethanol, and then dropping the suspension onto carbon-coated copper grids, followed by natural drying.

(4) X-ray photoelectron spectroscopy (XPS)

A Thermo Scientific K-Alpha XPS instrument was used to analyze the surface valence states of elements. All binding energies were calibrated with respect to the C 1s peak at 284.8 eV. To minimize surface contamination caused by exposure to air, the exposure time after removal from the drying oven was kept as short as possible, and mild Ar^+ ion sputtering was applied when necessary to clean the surface. Photographs of the above characterization instruments are shown in Fig. 3.15.

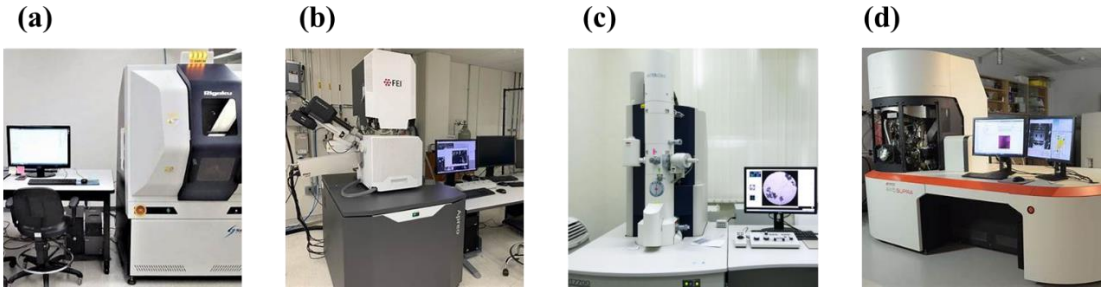

Fig. 3.15 Photographs of the physical characterization instruments: (a) XRD; (b) SEM/EDS; (c) TEM; (d) XPS

3.5.2 Electrochemical testing of zinc–air batteries

The electrochemical performance tests of the zinc–air batteries mainly included measurements of open-circuit voltage (OCV), load voltage, time-dependent load current, and voltage decay behavior.

(1) Open-circuit voltage test

After assembly, the cells were left to stand for 10 min. Then, under ambient air and at room temperature, the open-circuit voltages of the StZnB, Zn3B, Zn4B, and Zn5B zinc–air batteries were recorded over a period of 6 h without any external load, and the results were compared to evaluate the influence of different anode structures on the thermodynamic performance of the cells. The circuit diagram and a photograph of the test setup are shown in Fig. 3.16.

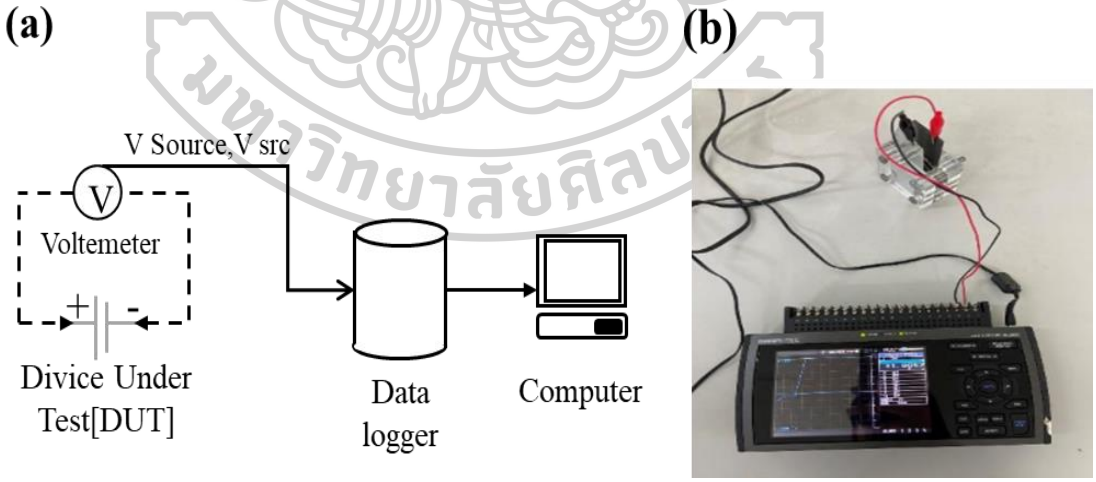

Fig. 3.16 Open-circuit voltage test scheme for zinc–air batteries: (a) schematic circuit diagram of the OCV test; (b) photograph of the OCV test setup

(2) Load performance test

In the load test, a light-emitting diode (LED) was used as the external load. The anode and air cathode of the battery were connected to the LED via wires to simulate a constant-resistance load under practical application conditions. A digital multimeter and data acquisition system were employed to continuously record the variations of load voltage and load current over 6 h, in order to analyze the voltage decay rate, current stability, and sustained discharge capability of cells with different anodes. The circuit diagram and a photograph of the test setup are shown in Fig. 3.17.

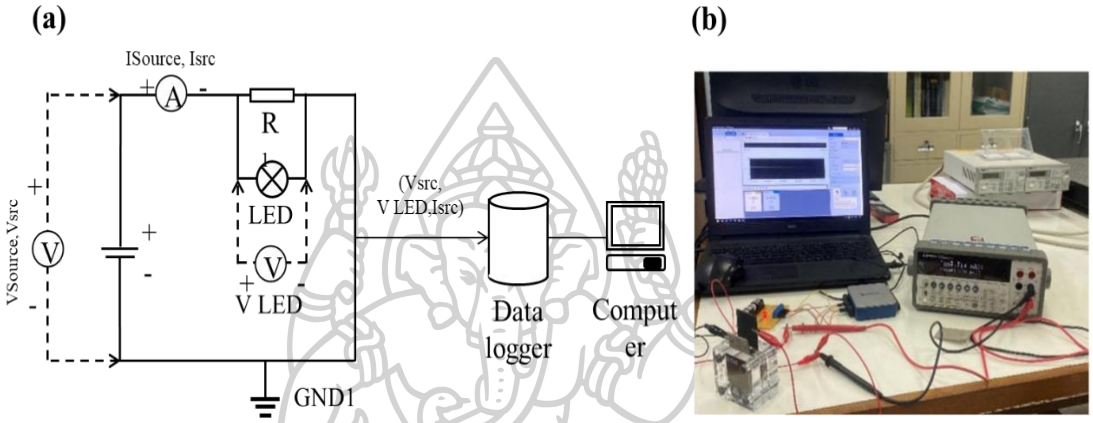

Fig. 3.17 Load performance test scheme for zinc–air batteries: (a) schematic circuit diagram of the load test; (b) photograph of the load test setup

3.6 Summary

This chapter has systematically introduced the experimental system employed in this study, including the pretreatment method for three-dimensional Ni foam substrates, the setup and operating conditions for electrochemically depositing zinc anodes, the assembly procedure of zinc–air batteries, and the main techniques for physical characterization and electrochemical testing. In terms of materials and process parameters, the specifications of Ni foam, the conditions for acid pickling and ultrasonic cleaning, the composition of the electrodeposition electrolyte, and the galvanostatic deposition protocol (including stirring conditions and deposition time gradients) were clearly defined, and a consistent nomenclature was established for the Zn3, Zn4, and Zn5 electrodes, their corresponding batteries Zn3B, Zn4B, Zn5B, and the control battery StZnB.

With respect to the experimental setup and testing platform, photographs and schematic diagrams were provided to illustrate the electrodeposition apparatus, the cell housing structure, and the load-testing circuit, thereby helping to ensure the reproducibility of the experimental procedures and the comparability of the results. On the basis of the experimental framework constructed in this chapter, the next chapter will present a systematic analysis and discussion of the structural and compositional characteristics of the electrodeposited zinc layers, as well as the discharge performance and cycling stability of the corresponding zinc–air batteries.

CHAPTER 4
EXPERIMENT RESULTS

4.1 Structural and compositional characterization of electrodeposited Zn/Ni foam anodes

4.1.1 Electrodeposition process and macroscopic morphology

To gain a clearer understanding of the formation process of the electrodeposited Zn/Ni foam composite anodes and to provide an intuitive background for the subsequent discussion of results, a schematic illustration of the electrodeposition process was first constructed in this study, as shown in Fig. 4.1.

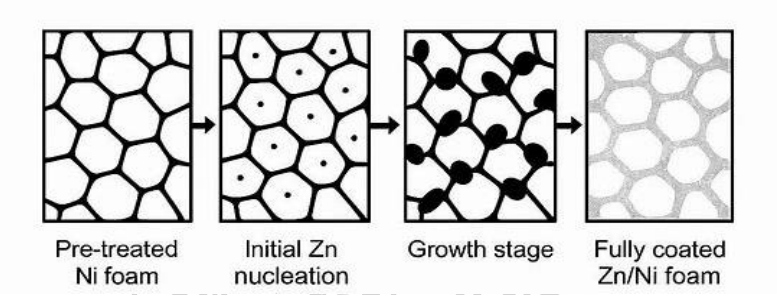

Fig. 4.1 Schematic illustration of the synthesis process of zinc electrodeposition on Ni foam

As shown in Fig. 4.1, during galvanostatic electrodeposition, Zn^{2+} ions nucleate and grow on the surface of the Ni foam skeleton, eventually forming a continuous zinc layer coating the three-dimensional porous Ni framework. Benefiting from the high specific surface area and open-pore structure of Ni foam, the deposition process can proceed relatively uniformly in space, laying the foundation for constructing zinc anodes with high loading and large electrochemically active surface area.

To visually demonstrate the macroscopic morphological evolution at different deposition stages, magnified optical images of samples after 1 h and 4 h of electrodeposition, as well as a SEM overview of the 4 h sample, are presented in Fig. 4.2.

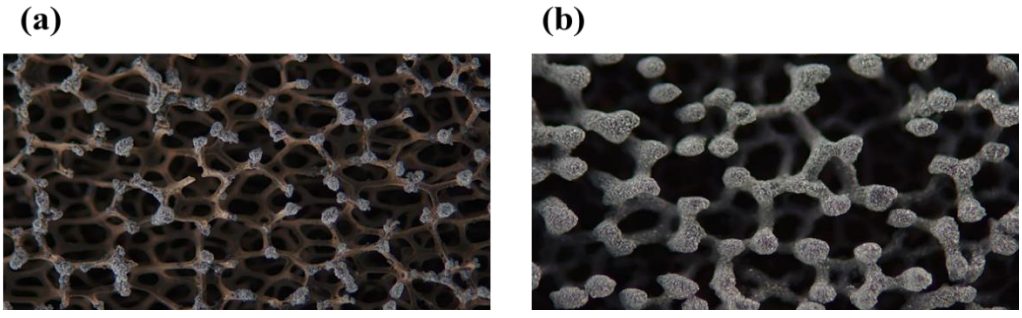

Fig. 4.2 Macroscopic and surface morphologies of zinc electrodeposited on Ni foam: (a) magnified image after 1 h of electrodeposition; (b) magnified image after 4 h of electrodeposition

As shown in Fig. 4.2(a), after 1 h of electrodeposition, bright regions appear only at local tips and edges of the Ni foam, indicating that zinc preferentially nucleates at sites with higher local electric fields and protruding regions at this early stage. When the deposition time is extended to 4 h (Fig. 4.2(b)), the overall color of the Ni foam becomes markedly more silvery white, and the surface of the skeleton appears glossier, suggesting that zinc has been deposited over a large area on the porous framework. No obvious peeling or large uncovered regions are observed, indicating that the electrodeposition conditions employed in this work can yield Zn/Ni foam composites with good interfacial adhesion.

4.1.2 Phase-structure analysis (XRD)

The phase composition of the electrodeposited zinc layers was characterized by X-ray diffraction (XRD), and the results are shown in Fig. 4.3.

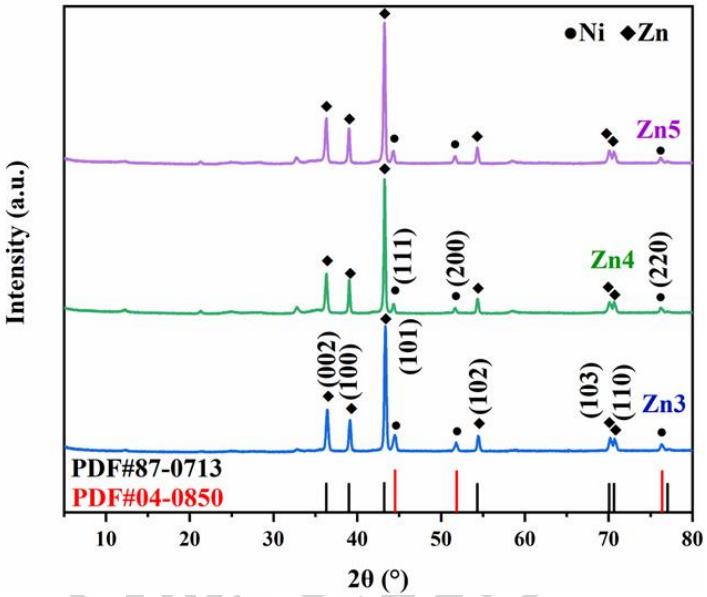

Fig. 4.3 XRD patterns of Zn3, Zn4, and Zn5 electrodes

As shown in Fig. 4.3, distinct diffraction peaks can be observed at around 36.4°, 39.1°, 43.4°, 54.4°, 70.2°, and 70.6°, which can be indexed to the (002), (100), (101), (102), (103), and (110) planes of metallic zinc (PDF#87-0713), respectively. Meanwhile, the diffraction peaks at 44.5°, 51.2°, and 76.3° are consistent with the (111), (200), and (220) planes of Ni (PDF#04-0850), indicating that the diffraction contribution of the Ni foam substrate is still present in the samples. It is noteworthy that no obvious characteristic peaks of ZnO are detected within the tested range, suggesting that under the optimized electrodeposition and post-treatment conditions, the deposited zinc layer predominantly remains in the metallic state, thereby avoiding the negative impact of excessive oxidation on electrical conductivity and the reversibility of electrochemical reactions.

The overall XRD peak profiles of Zn3, Zn4, and Zn5 are similar, and the peak positions nearly coincide, indicating that the crystal structure of the zinc layer remains unchanged with increasing

deposition time, without any detectable phase transformation on the macroscopic level. The variations in peak intensity are mainly related to differences in zinc-layer thickness, grain orientation, and the relative proportions of zinc and nickel.

4.1.3 Elemental distribution and quantitative analysis (EDS)

To further confirm the spatial distribution of zinc on the Ni foam skeleton, EDS elemental mapping was performed on the representative sample Zn4, and the results are shown in Fig. 4.4.

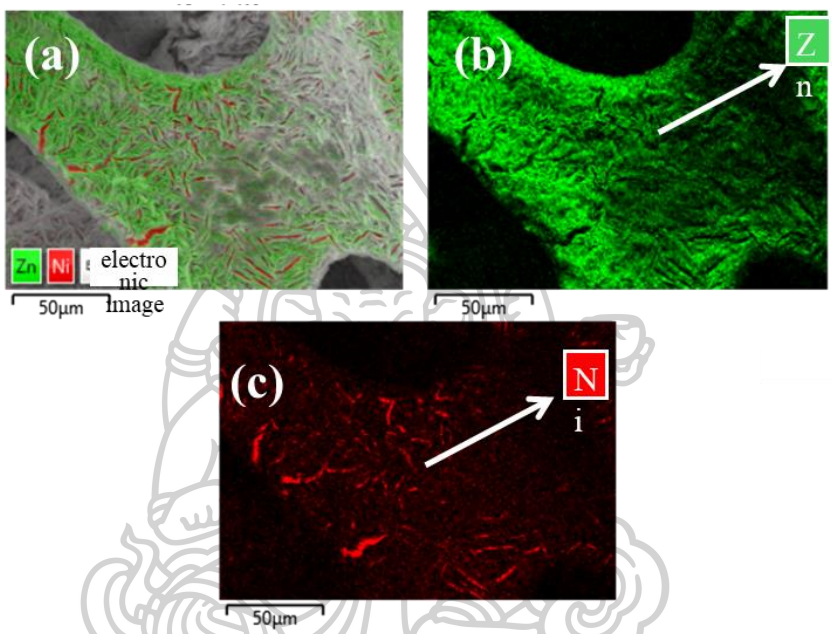

Fig. 4.4 EDS elemental mapping of sample Zn4 after 4 h of electrodeposition: (a) EDS composite elemental map; (b) EDS map of Zn; (c) EDS map of Ni

As shown in Fig. 4.4(b), Zn is uniformly distributed over the entire field of view and almost completely covers the Ni foam skeleton. The Ni signal (Fig. 4.4(c)) is mainly concentrated in the inner regions of the skeleton and becomes slightly weaker in areas where the Zn layer is relatively thick. The overlapped map (Fig. 4.4(d)) further demonstrates that the Ni framework is coated by a continuous zinc layer, and the two elements exhibit a typical “core–shell” spatial distribution. This indicates that Zn^{2+} can be reduced and deposited relatively uniformly on the three-dimensional framework during electrodeposition, without large exposed Ni regions or severe segregation.

To quantitatively analyze the elemental composition of Zn4, EDS point/area quantification was carried out on representative regions. The results are summarized in Table 4.1 and are visually presented as a bar chart in Fig. 4.5.

Table 4.1 EDS quantitative results of Zn and Ni mass fractions in sample Zn4

Total distribution map of spectrograms			
Element	**Signal type**	**Wt%**	**Wt% Sigma**
Ni	EDS	15.99	0.12
Zn	EDS	84.01	0.12
Total		100.00	

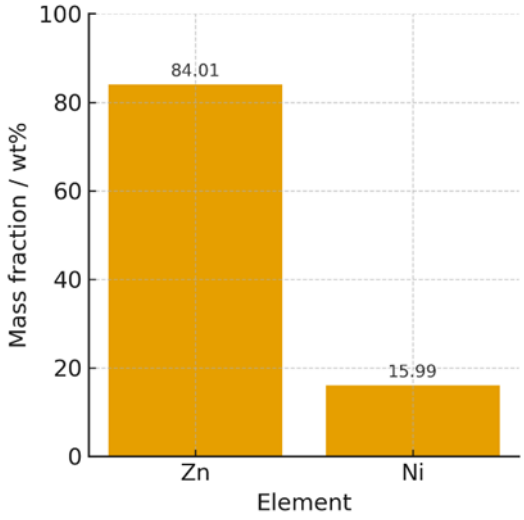

Fig. 4.5 EDS quantitative mass fractions of Zn and Ni in sample Zn4

The quantitative analysis shows that the mass fraction of Zn in Zn4 is about 84.01 wt%, while that of Ni is about 15.99 wt%. This indicates that, under the 4 h deposition condition, a large amount of zinc is successfully loaded onto the Ni foam skeleton, which is consistent with the design objective of constructing a “high-loading Zn/three-dimensional current collector composite anode.”

4.1.4 Microstructure and lattice information (TEM)

To further analyze the crystal structure of the electrodeposited zinc layer at the nanoscale, TEM and high-resolution TEM (HRTEM) characterizations were performed on the Zn4 sample, and the results are shown in Fig. 4.6.

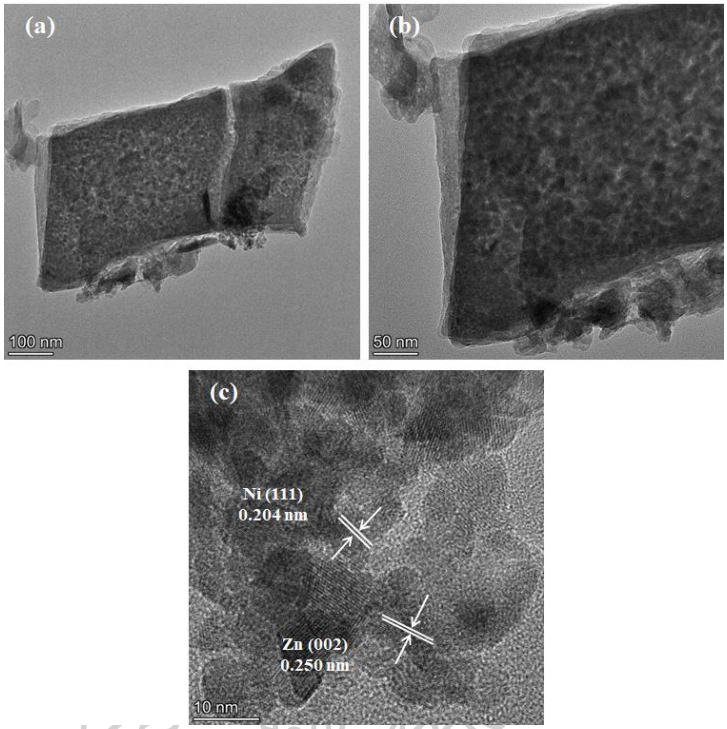

Fig. 4.6 TEM and HRTEM images of sample Zn4 after 4 h of electrodeposition: (a, b) TEM images of flake-like zinc structures in Zn4; (c) HRTEM image of Zn4 and the corresponding lattice spacings

As shown in Fig. 4.6(a) and (b), zinc in Zn4 mainly exists in the form of flakes or flake–particle aggregates, with characteristic sizes ranging from several hundred nanometers to the micrometer scale. Such structures are beneficial for providing a relatively large specific surface area and for constructing a hierarchical conductive network within the pores. In the HRTEM image (Fig. 4.6(c)), the measured lattice spacings of approximately 0.250 nm and 0.204 nm can be indexed to the (002) plane of Zn and the (111) plane of Ni, respectively, further confirming that the zinc layer is successfully deposited on the nickel substrate. These observations are consistent with the XRD and EDS results.

4.1.5 Surface chemical-state analysis (XPS)

The chemical valence states of surface elements were analyzed by XPS, and typical high-resolution spectra are shown in Fig. 4.7.

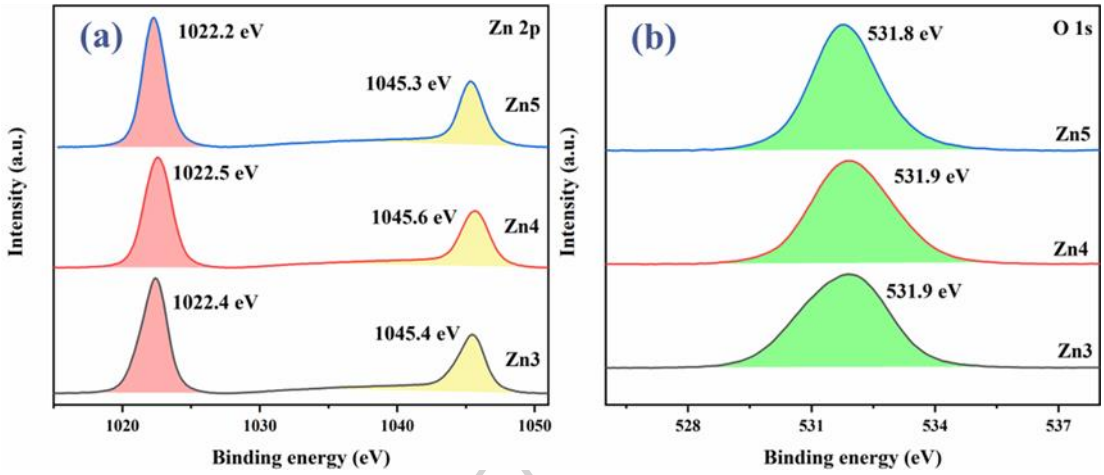

Fig. 4.7 High-resolution XPS spectra of samples obtained at different electrodeposition times: (a) Zn 2p spectra; (b) O 1s spectra

As shown in Fig. 4.7(a), the Zn 2p spectra of Zn3, Zn4, and Zn5 all exhibit a pair of characteristic peaks at approximately 1022.4 eV and 1045.4 eV, corresponding to Zn $2p_{3/2}$ and Zn $2p_{1/2}$, respectively. The binding energies are close to those of metallic zinc (Zn^0), and no obvious shift toward higher binding energy is observed, indicating that zinc predominantly exists in the metallic state. In the O 1s spectra (Fig. 4.7(b)), all three samples show a characteristic peak at around 531.8 eV, which can be attributed to adsorbed oxygen or surface hydroxyl species. These are likely related to a thin surface oxide/hydroxide layer formed during short-term exposure of the electrodes to air and alkaline electrolyte. Combined with the XRD results, where no distinct ZnO diffraction peaks are detected, it can be inferred that this surface oxidized/hydroxylated layer is relatively thin and has a limited impact on the overall phase structure, although it may play a certain regulatory role in interfacial stability and wettability.

4.2 Influence of electrodeposition time on electrochemical properties and zinc–air battery performance

4.2.1 Evolution of mass and thickness

To systematically investigate the effect of electrodeposition time on zinc loading and the geometric structure of the electrodes, the mass of all samples was accurately measured before and after deposition. In addition, cross-sectional observations combined with multi-point measurements were used to estimate the average thickness of the electrodes. The quantitative results are summarized in Table 4.2.

Table 4.2 Thickness of samples after electrodeposition

	Zn3	Zn4	Zn5
Measurement position 1	0.82	0.91	0.97
Measurement position 2	0.79	0.95	0.98
Measurement position 3	0.8	0.93	1.05
Average thickness	0.80	0.93	1.00

The results show that, as the electrodeposition time increases from 3 h to 5 h, both the sample mass and the average thickness exhibit a monotonic increase. The average thicknesses of Zn3, Zn4, and Zn5 are approximately 0.80 mm, 0.93 mm, and 1.00 mm, respectively. This behavior is consistent with the linear growth characteristics of electrodeposition under galvanostatic conditions, indicating that, under the applied current density, electrolyte composition, and stirring conditions, the deposition process operates within a relatively stable regime governed by mass transport and interfacial reactions. A moderate increase in thickness is beneficial for enhancing zinc loading; however, an excessively thick deposited layer may lead to pore blockage and extended diffusion paths, which will reduce the effective utilization of zinc. These effects will be further reflected in the subsequent discussion of electrochemical performance.

4.2.2 Impedance spectroscopy analysis and interfacial kinetics

Fig. 4.8 shows the Nyquist plots of the electrochemical impedance spectra (EIS) of Zn3, Zn4, and Zn5 measured in 6 mol L^{-1} KOH solution at room temperature.

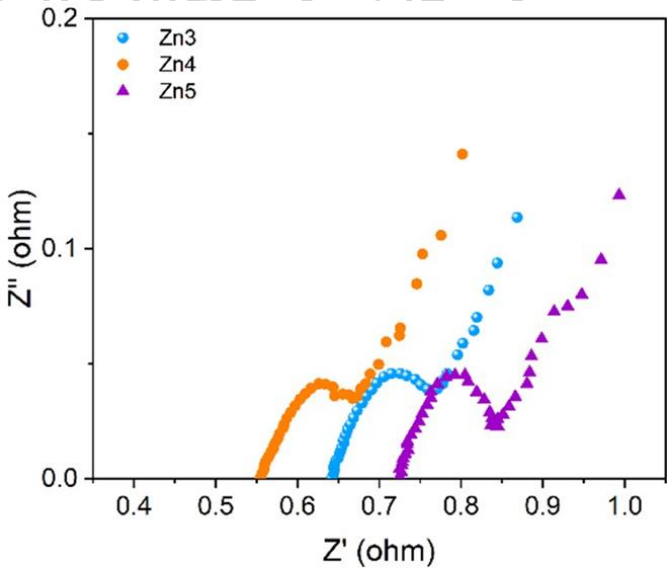

Fig. 4.8 Nyquist plots of Zn3, Zn4, and Zn5 electrodes in 6 mol L^{-1} KOH

According to the features of the EIS spectra, the corrosion/reaction process of the electrodes in the electrolyte can be simplified into two main stages:

(1) The high-frequency semicircle corresponds to the charge-transfer process of zinc at the electrode/electrolyte interface, i.e., the electron transfer from metallic Zn to the external circuit during the Zn → ZnO_2^{2-} or $Zn(OH)_4^{2-}$ formation process.

(2) The low-frequency tail is related to diffusion processes and corresponds to the diffusion of ZnO_2^{2-} or $Zn(OH)_4^{2-}$ from the electrode surface into the bulk electrolyte.

To further quantify these processes, the solution resistance Rs and charge-transfer resistance Rct were extracted by fitting the EIS data with an equivalent circuit model. The equivalent circuit used for fitting is shown in Fig. 4.9.

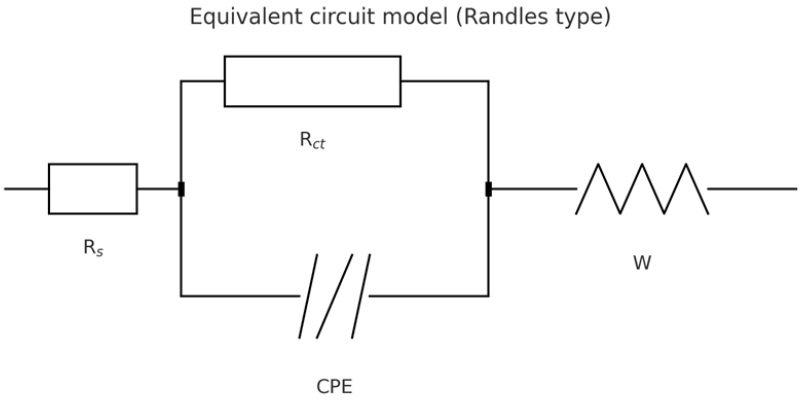

Fig. 4.9 Equivalent circuit model used for fitting the EIS data

For a more intuitive comparison, the fitted Rs and Rct values for the different samples are summarized in bar-chart form in Fig. 4.10.

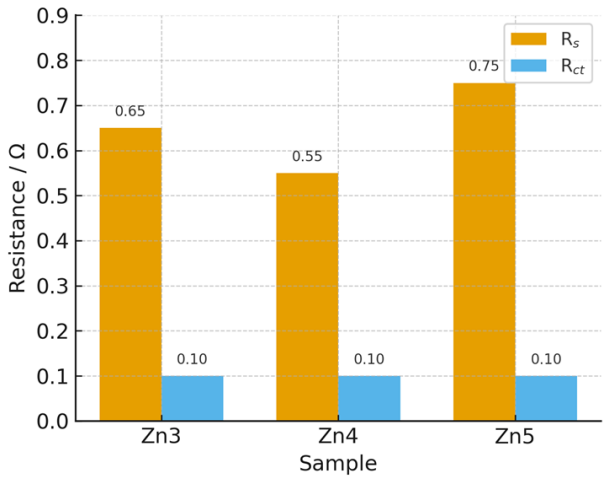

Fig. 4.10 Comparison of solution resistance Rs and charge-transfer resistance Rct for different samples

It can be seen that, as the deposition time increases from 3 h to 4 h, Rs decreases, indicating that an appropriately thick and more continuous zinc layer improves the effective reaction area and electrical contact quality at the electrode/electrolyte interface. When the deposition time is further extended to 5 h, Rs shows a slight increase, which may be related to partial pore blockage by the overly thick zinc layer, the lengthening of transport pathways, and the fact that the locally effective area does not increase proportionally. Overall, Zn4 exhibits the most favorable electrochemical kinetic characteristics among the three samples.

4.2.3 Open-circuit voltage and load performance

To evaluate the influence of different anode structures on the performance of zinc–air batteries, four types of cells were assembled: a control cell (StZnB) using a pure zinc plate as the anode, and three cells (Zn3B, Zn4B, Zn5B) using Zn3, Zn4, and Zn5 as the anodes, respectively. The open-circuit voltage (OCV) of each cell was recorded over 6 h, and, under an LED load, the load voltage and load current were also monitored for 6 h. The time-dependent OCV curves of the four cells are shown in Fig. 4.11.

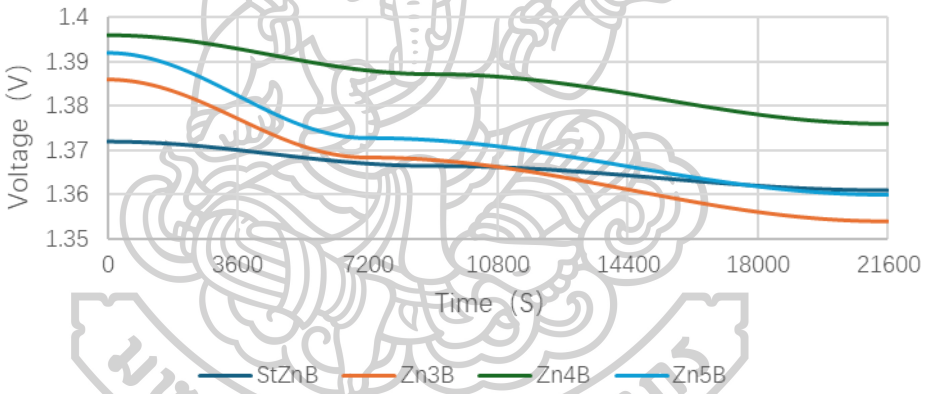

Fig. 4.11 Time-dependent open-circuit voltage curves of different zinc–air batteries

As shown in Fig. 4.11, the initial open-circuit voltage of all cells is higher than 1.37 V. Among them, Zn4B exhibits the highest initial OCV of about 1.396 V, whereas StZnB shows a relatively lower value. With increasing time, the OCV of Zn3B decreases most significantly, which is related to its lower zinc loading and insufficient reserve of active material: spontaneous corrosion and side reactions rapidly intensify polarization, leading to a pronounced decay in open-circuit voltage. In contrast, Zn4B and Zn5B show relatively slower OCV decay, and Zn4B maintains the highest average OCV over 6 h, indicating that the anode obtained with a 4 h deposition time is thermodynamically closer to the ideal state.

After connecting the LED load, the time-dependent load voltage and load current of the different cells are shown in Fig.s 4.12 and 4.13, respectively.

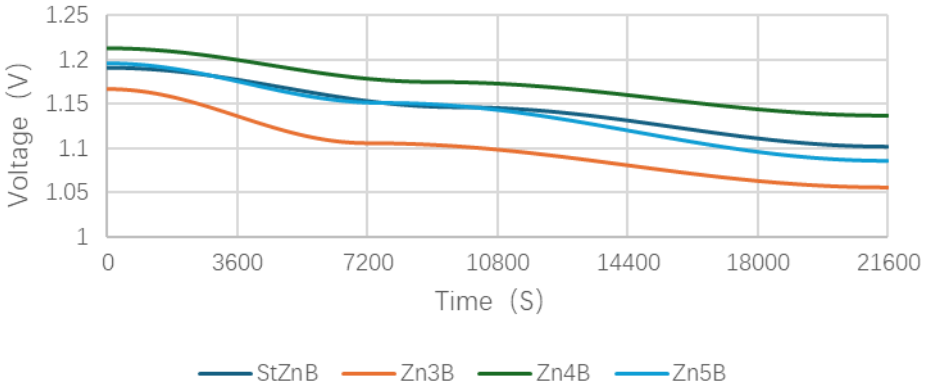

Fig. 4.12 Time-dependent load voltage curves of different zinc–air batteries over 6 h

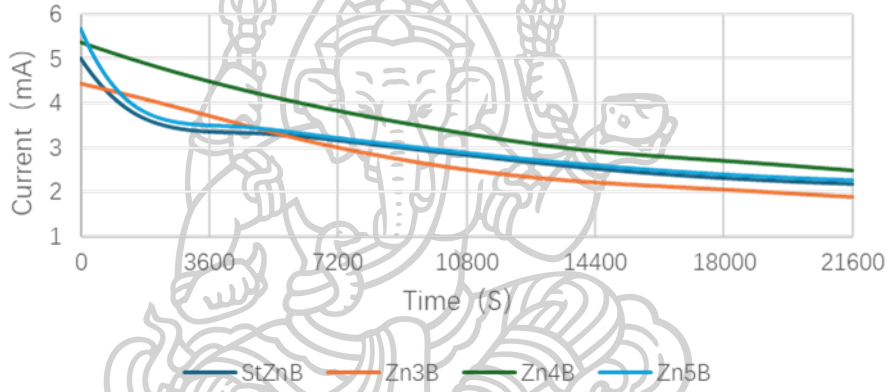

Fig. 4.13 Time-dependent load current curves of different zinc–air batteries over 6 h

As can be seen from Fig. 4.12, once the load is applied, the initial working voltage of all cells is lower than their corresponding OCV, which is an inevitable result of increased polarization under external load. Nevertheless, Zn4B consistently maintains the highest load voltage and exhibits an average working voltage of about 1.17 V over 6 h, demonstrating a clear advantage in delivering higher operating voltage. In comparison, Zn3B suffers from faster voltage decay due to insufficient zinc loading; Zn5B, although possessing a larger initial zinc reserve, does not show a more stable working voltage than Zn4B, likely because the excessively thick zinc layer leads to non-uniform deposition and local dendrite formation, which aggravate polarization and increase internal resistance.

The load current curves (Fig. 4.13) further reveal the current-output characteristics of the different anodes. Zn5B shows the highest initial current, reaching approximately 5.7 mA, indicating higher initial electrochemical activity and lower internal resistance. However, its current drops rapidly within the first hour and then stabilizes at a lower level, suggesting that the interfacial structure deteriorates quickly during continuous discharge. This deterioration may be associated with locally over-consumed zinc, dendrite formation, and pore blockage within the thick zinc layer. In contrast, although Zn4B exhibits a slightly lower initial current than Zn5B, its current decay is significantly

slower, maintaining a more stable output over 6 h. This indicates that a moderate zinc loading combined with a uniform deposition morphology is beneficial for achieving a balance between reaction kinetics and structural stability.

4.3 Correlation between micro-morphology and electrochemical performance

To elucidate, at the microscopic level, the fundamental reasons why different electrodeposition times affect the performance of zinc–air batteries, the surface morphologies of Zn3, Zn4, and Zn5 were examined by SEM at multiple magnifications, as shown in Figs. 4.14 - 4.16.

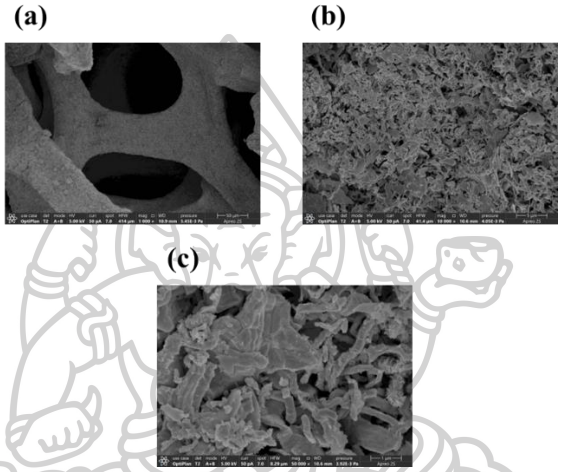

Fig. 4.14 Surface SEM images of sample Zn3: (a) 1000×; (b) 10,000×; (c) 50,000×

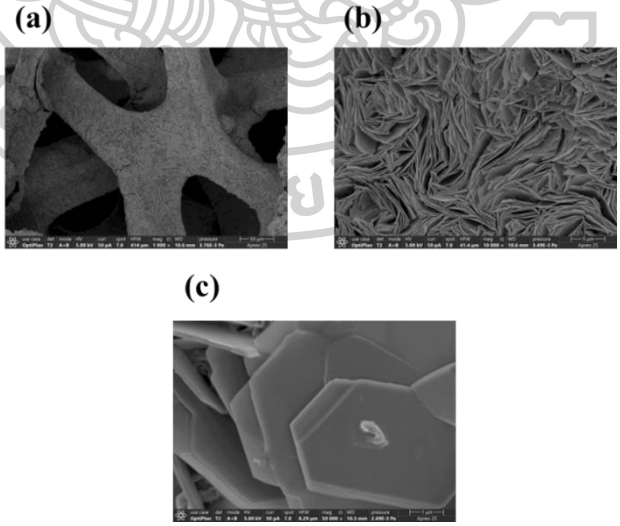

Fig. 4.15 Surface SEM images of sample Zn4: (a) 1000×; (b) 10,000×; (c) 50,000×

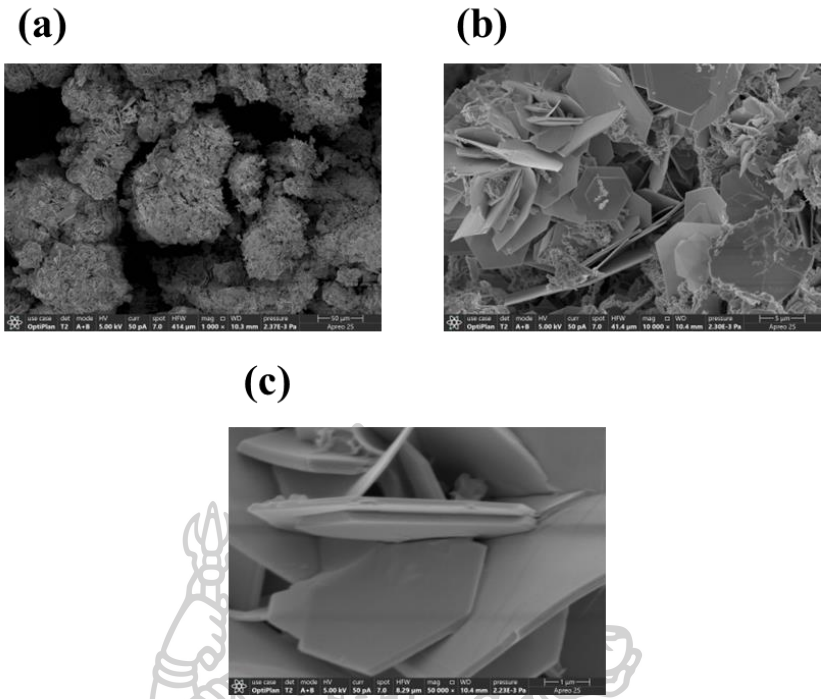

Fig. 4.16 Surface SEM images of sample Zn5: (a) 1000×; (b) 10,000×; (c) 50,000×

As shown in Fig. 4.14, the surface structure of Zn3 is overall relatively loose. The low-magnification image (a) indicates that only part of the electrode surface is covered by zinc, with a large portion of the Ni foam skeleton still exposed. In the medium and high magnification images (b, c), the deposited zinc mainly appears in a flocculent or fine particulate form, with poor interparticle contact. This easily leads to local current concentration and non-uniform electrolyte penetration. Although such a morphology can provide highly active reaction sites at the initial stage, the limited amount of effectively stored zinc and the loose structure tend to cause rapid polarization growth and pronounced decay in both voltage and current during long-term discharge, which is consistent with the battery performance observed for Zn3B.

In contrast, the surface morphology of Zn4 shown in Fig. 4.15 is more uniform and compact. In the low-magnification image (a), the Ni foam skeleton is almost completely covered by a continuous zinc layer, while a certain open pore volume is still preserved inside the channels. The medium-magnification image (b) shows that the zinc layer exhibits a flake-like or flake–particle composite morphology, continuously covering the substrate with good interconnection. In the high-magnification image (c), relatively regular crystal facets and boundaries can be observed, and the interparticle pores appear relatively homogeneous. This moderately dense and uniform zinc layer provides, on the one hand, a sufficient amount of active material and a large electrochemically active surface area, and on the other hand, a continuous electronic conduction network and unobstructed ion-diffusion pathways within the 3D framework. As a result, it helps lower the charge-transfer resistance and concentration

polarization, which is reflected in the higher and more stable working voltage and load current of the Zn4B cell.

By comparison, the morphology of Zn5 in Fig. 4.16 exhibits a pronounced “over-deposition” feature. The low-magnification image (a) shows that many pores are partially or even completely filled by bulky deposits, leading to locally congested structures. The medium-magnification image (b) reveals larger blocky aggregates with blurred boundaries between individual particles. The high-magnification image (c) displays a rough surface with numerous protrusions, where locally intensified electric fields are prone to occur during cycling, thereby promoting preferential dendrite growth and accelerating interfacial degradation. Although the Zn5 anode has a larger initial zinc inventory (higher mass and thickness) and demonstrates a higher initial current output in the cell, its performance decays rapidly under prolonged discharge due to elongated mass-transport paths and localized accumulation of stress and polarization. This observation is consistent with the EIS and load-test results.

Combining the above characterization and electrochemical results, the influence of electrodeposition time on zinc–air battery performance can be mechanistically summarized as follows:

(1) Balance between zinc loading and utilization efficiency

As the deposition time increases, both zinc loading and anode thickness increase monotonically, which is beneficial for enhancing the theoretical capacity and extending discharge time.

However, when the zinc layer becomes excessively thick and non-uniformly distributed, pore blockage and the formation of local “dead zinc” regions become more pronounced, reducing the fraction of zinc that can be effectively utilized and even leading to poorer electrochemical stability during long-term cycling.

(2) Regulation of interfacial kinetics by micro-morphology

The flocculent, loose structure of Zn3 provides a high specific surface area at the early stage, but the poor electrical contact and insufficient mechanical stability of the deposits facilitate rapid interfacial degradation.

The flake-like/flake–particle composite morphology of Zn4 achieves a balance between continuity and openness: it forms a robust conductive framework while still providing sufficient channels for electrolyte penetration and reactant diffusion. This is the optimal morphology in this study in terms of overall performance.

The blocky, aggregated structure of Zn5 increases local thickness but hinders ion transport and stress relaxation, making dendrite growth and pore “clogging” more likely.

(3) Synergistic effect of the 3D porous framework and electrodeposition process**

The three-dimensional Ni foam provides multidirectional electronic pathways and a complex pore network. By optimizing electrodeposition parameters (current density, deposition time, stirring conditions, etc.), a uniform zinc layer can be constructed on the skeleton surface.

With an appropriate deposition time, the 3D framework can effectively disperse local current density and mitigate electric-field concentration, thereby suppressing dendrite growth and enhancing the mechanical adhesion between the zinc layer and the substrate.

Excessively short or excessively long deposition times disrupt this balance: the former leads to insufficient loading, whereas the latter causes over-densified structures and local accumulation.

In summary, a comprehensive comparison of Zn3, Zn4, and Zn5 in terms of structure, composition, electrochemical kinetics, and battery performance clearly indicates that the Zn4 anode obtained with a 4 h electrodeposition time achieves a relatively optimal match among zinc loading, micro-morphology, and interfacial kinetics. Consequently, the Zn4B zinc–air battery exhibits a higher open-circuit voltage, a more stable working voltage, and a more sustained current output. These findings provide important experimental evidence and mechanistic support for the structural optimization of zinc anodes based on three-dimensional porous current collectors.

CHAPTER 5
CONCLUSION

This chapter provides an overall summary of the research presented in Chapters 1–4, highlighting the main conclusions of this work, analyzing the remaining limitations, and proposing possible directions for future research. In addition, a schematic diagram of the structure–performance relationship and a comparative table are presented to help intuitively understand the core findings of this study.

5.1 Conclusions

This dissertation focuses on the construction of high-performance zinc–air battery anodes via electrochemical deposition of zinc on three-dimensional (3D) Ni foam substrates. From theoretical analysis to experimental fabrication and performance evaluation, the main conclusions are as follows.

5.1.1 Advantages of 3D Ni-foam / electrodeposited Zn composite anodes

(1) Mechanistically, Chapter 2 shows that zinc in alkaline electrolytes undergoes a "Zn → $Zn(OH)_4^{2-}$ → ZnO" dissolution–precipitation process, during which ZnO passivation layers and locally high current densities are easily formed, triggering dendrite growth and "dead Zn" accumulation. A three-dimensional current collector can alleviate these issues by increasing the effective surface area and dispersing the local current density.

(2) In Chapter 3, a standardized pre-treatment and electrodeposition procedure based on 1.5 mm-thick, 100 PPI Ni foam was established. Composite anodes Zn3, Zn4, and Zn5 with different deposition times were prepared in 0.5 $mol \cdot L^{-1}$ $ZnSO_4$ solution under a constant current density of 0.11 $A \cdot cm^{-2}$.

(3) Chapter 4 demonstrates, through XRD, EDS, TEM, and XPS, that under optimized conditions zinc uniformly covers the Ni skeleton in a metallic state, forming a 3D "Ni core–Zn shell" composite structure with a Zn mass fraction of about 80–85 wt%. This architecture combines a highly conductive backbone with a large specific surface area, which is beneficial for improving the active utilization and interfacial stability of the zinc anode.

5.1.2 Influence of electrodeposition time on morphology and interfacial kinetics

(1) As the deposition time increases from 3 h to 5 h, both the Zn loading and the electrode thickness increase approximately linearly (from about 0.80 to 0.93 and 1.00 mm), indicating an overall stable deposition process.

(2) Multi-magnification SEM observations show that:

Zn3 exhibits a loose, flocculent Zn layer with incomplete coverage;

Zn4 presents a uniform and continuous flake-like or flake–particle composite Zn layer while the pores remain open;

Zn5 shows pronounced block-like agglomeration and partial pore blockage, with a rough surface and obvious protrusions.

(3) EIS fitting results indicate that the three samples share a similar charge-transfer process, but Zn4 exhibits the lowest solution resistance Rs and charge-transfer resistance Rct (Rs ≈ 0.55 Ω), and thus the most favorable interfacial kinetics. In contrast, Zn3 suffers from insufficient coverage and Zn5 from over-deposition and local blockage, leading to higher resistances than Zn4.

5.1.3 Overall optimal performance of the Zn4/Zn4B system

(1) Structurally, the Zn4 anode achieves a balance between “continuous coverage” and “pore retention”: it provides sufficient Zn loading without causing severe pore clogging. HRTEM images show clear lattice fringes, indicating good crystalline quality.

(2) From a kinetic perspective, Zn4 exhibits the lowest Rs and Rct, suggesting that its anode/electrolyte interface is most favorable for electron and ion transport.

(3) In terms of cell performance, among the cells assembled with Zn3, Zn4, Zn5, and a pure Zn plate as anodes (Zn3B, Zn4B, Zn5B, and StZnB):

all cells show initial open-circuit voltages (OCVs) higher than 1.37 V, with Zn4B exhibiting the highest value (~1.396 V) and the slowest decay within 6 h;

Zn4B delivers the best overall performance, with an average load voltage of about 1.17 V under an LED load;

Zn5B provides the highest initial current (~5.7 mA) but suffers from the fastest current decay, while Zn3B shows generally inferior performance due to insufficient Zn loading.

For ease of comparison, the key structural and performance parameters can be summarized in a comparative table (Table 5.1).

Table 5.1 Summary of key parameters for different Zn anode samples

Sample	StZn	Zn3	Zn4	Zn5
Deposition time / h	/	3h	4h	5h
Thickness / mm	/	0.80	**0.93**	1.00
Typical morphology	/	Loose, flocculent	**Continuous, flake-like**	Block-like agglomeration
Rs(Ω)	/	0.65	**0.55**	0.75
Tct(Ω)	/	0.1	**0.1**	0.1
Initial voltage / V	1.372	1.386	**1.396**	1.392
Average load voltage / V	1.14	1.1	**1.17**	1.14
Average load current / mA	2.9	2.76	**3.52**	3

Overall conclusion: By integrating a three-dimensional Ni foam current collector with a controllable electrodeposition process, the microstructure and interfacial properties of zinc anodes can be significantly optimized. Under the conditions employed in this work, the Zn4 anode obtained with a 4 h electrodeposition time, together with its corresponding Zn4B cell, achieves the best overall balance among structural integrity, interfacial kinetics, and discharge performance.

5.2 Limitations

This work still has several limitations, mainly including:

(1) The electrolyte system is single; all tests were conducted only in 6 mol·L^{-1} KOH, without a systematic comparison of the behavior and stability in neutral or near-neutral electrolytes.

(2) The optimization space of electrodeposition parameters is limited. The study mainly focuses on deposition time, while other factors such as current density, additives, electrolyte concentration, temperature, and current waveform have not yet been systematically explored.

(3) Performance evaluation is primarily based on 6 h discharge tests. Long-term cycling (multiple charge–discharge cycles) and multi-rate tests are lacking, so the lifetime and power characteristics under practical rechargeable zinc–air battery conditions cannot yet be fully assessed.

(4) Most of the characterization is ex situ, without in situ or operando techniques. As a result, the dynamic processes of dendrite formation, ZnO passivation-layer evolution, and “dead zinc” accumulation are still not directly evidenced.

(5) The air electrode and overall cell configuration have not been deeply optimized. The use of Pt/C@carbon plates serves more as a “standardized configuration” and is not sufficient to evaluate the system-level performance limits under low- or non-precious-metal conditions.

5.3 Outlook

Building on the work presented in this dissertation, future studies can be further extended and deepened in the following directions:

(1) Broadening the electrolyte systems

Systematically compare the zinc dissolution–deposition behavior, side-reaction characteristics, and interfacial stability in alkaline, neutral, and near-neutral electrolytes, and explore new electrolyte systems that combine high safety with high efficiency.

(2) Deepening electrodeposition process optimization and morphology control

Introduce pulse electrodeposition, periodic reverse deposition, multi-step current programs, and composite additives to regulate nucleation density, grain size, and crystallographic orientation, thereby achieving more refined morphological design and more effective dendrite suppression.

(3) Constructing a multiscale in situ characterization framework

Combine in situ XRD, in situ electrochemical microscopy, and X-ray computed tomography (X-CT) to track in real time the evolution of zinc morphology and phase structure, and correlate these with electrochemical techniques such as EIS, CV, and GITT to establish cross-scale mechanistic models from the nano- to the electrode scale.

(4) Moving from anode optimization to full-cell design

On the basis of the optimized anode, further design low- or non-precious-metal bifunctional air electrodes for practical rechargeable zinc–air battery applications, optimize the gas diffusion layer and water management, and improve the cell packaging structure to enhance overall energy density and cycle life.

(5) Engineering scale-up and application-oriented evaluation

Carry out module-level testing based on single-cell results to explore the feasibility of applications in portable power supplies, emergency power systems, and distributed energy storage. Combine these studies with cost analysis and life-cycle assessment to provide quantitative guidance for future engineering implementation and industrialization.

REFERENCES

[1] L.-q. Liu, Z.-x. Wang, H.-q. Zhang, and Y.-c. Xue, "Solar energy development in China—A review," (in en), *Renewable and Sustainable Energy Reviews,* vol. 14, no. 1, pp. 301–311, 2010–01–01 2010, doi: 10.1016/j.rser.2009.08.005.

[2] J.-N. Liu, C.-X. Zhao, J. Wang, D. Ren, B.-Q. Li, and Q. Zhang, "A brief history of zinc–air batteries: 140 years of epic adventures," (in en), *Energy & Environmental Science,* vol. 15, no. 11, pp. 4542–4553, 2022 2022, doi: 10.1039/D2EE02440C.

[3] Y. Huang *et al.*, "Atomic Modulation and Structure Design of Carbons for Bifunctional Electrocatalysis in Metal–Air Batteries," (in en), *Advanced Materials,* vol. 31, no. 13, p. 1803800, 2019 2019, doi: 10.1002/adma.201803800.

[4] P. Sapkota and H. Kim, "Zinc–air fuel cell, a potential candidate for alternative energy," (in en), *Journal of Industrial and Engineering Chemistry,* vol. 15, no. 4, pp. 445–450, 7/2009 2009, doi: 10.1016/j.jiec.2009.01.002.

[5] X. Min, G. Xu, B. Xie, P. Guan, M. Sun, and G. Cui, "Challenges of prelithiation strategies for next generation high energy lithium-ion batteries," (in en), *Energy Storage Materials,* vol. 47, pp. 297–318, 05/2022 2022, doi: 10.1016/j.ensm.2022.02.005.

[6] S. Agnew and P. Dargusch, "Effect of residential solar and storage on centralized electricity supply systems," (in en), *Nature Climate Change,* vol. 5, no. 4, pp. 315–318, 4/2015 2015, doi: 10.1038/nclimate2523.

[7] R.-B. Huang, M.-Y. Wang, J.-F. Xiong, H. Zhang, J.-H. Tian, and J.-F. Li, "Anode optimization strategies for zinc–air batteries," (in en), *eScience,* vol. 5, no. 3, p. 100309, 05/2025 2025, doi: 10.1016/j.esci.2024.100309.

[8] J. Fu, Z. P. Cano, M. G. Park, A. Yu, M. Fowler, and Z. Chen, "Electrically Rechargeable Zinc-Air Batteries: Progress, Challenges, and Perspectives," (in en), *Advanced Materials,* vol. 29, no. 7, p. 1604685, 02/2017 2017, doi: 10.1002/adma.201604685.

[9] H. S. Hayajneh and X. Zhang, "Logistics Design for Mobile Battery Energy Storage Systems," (in en), *Energies,* vol. 13, no. 5, p. 1157, 2020/1 2020, doi: 10.3390/en13051157.

[10] K. W. Leong, Y. Wang, M. Ni, W. Pan, S. Luo, and D. Y. C. Leung, "Rechargeable Zn-air batteries: Recent trends and future perspectives," (in en), *Renewable and Sustainable Energy Reviews,* vol. 154, p. 111771, 02/2022 2022, doi: 10.1016/j.rser.2021.111771.

[11] R. Khezri *et al.*, "Stabilizing zinc anodes for different configurations of rechargeable zinc-air batteries," (in en), *Chemical Engineering Journal,* vol. 449, p. 137796, 12/2022 2022, doi: 10.1016/j.cej.2022.137796.

[12] M. Armand and J.-M. Tarascon, "Building better batteries," (in en), *Nature,* vol. 451, no. 7179, pp. 652–657, 2008–02 2008, doi: 10.1038/451652a.

[13] T. Kim, W. Song, D.-Y. Son, L. K. Ono, and Y. Qi, "Lithium-ion batteries: outlook on present, future, and hybridized technologies," (in en), *Journal of Materials Chemistry A,* vol. 7, no. 7, pp. 2942–2964, 2019–02–12 2019, doi: 10.1039/C8TA10513H.

[14] M. Li, J. Lu, Z. Chen, and K. Amine, "30 Years of Lithium-Ion Batteries," (in en), *Advanced Materials,* vol. 30, no. 33, p. 1800561, 2018 2018, doi: 10.1002/adma.201800561.

[15] M. Winter, B. Barnett, and K. Xu, "Before Li Ion Batteries," *Chemical Reviews,* vol. 118, no. 23, pp. 11433–11456, 2018–12–12 2018, doi: 10.1021/acs.chemrev.8b00422.

[16] N. Nitta, F. Wu, J. T. Lee, and G. Yushin, "Li-ion battery materials: present and future," (in en), *Materials Today,* vol. 18, no. 5, pp. 252–264, 2015–06–01 2015, doi: 10.1016/j.mattod.2014.10.040.

[17] J. B. Goodenough and K.-S. Park, "The Li-Ion Rechargeable Battery: A Perspective," (in en), *Journal of the American Chemical Society,* vol. 135, no. 4, pp. 1167–1176, 2013–01–30 2013, doi: 10.1021/ja3091438.

[18] K. Harting, U. Kunz, and T. Turek, "Zinc-air Batteries: Prospects and Challenges for Future Improvement," (in en), *Zeitschrift für Physikalische Chemie,* vol. 226, no. 2, pp. 151–166, 2012–02–01 2012, doi: 10.1524/zpch.2012.0152.

[19] V. Soundharrajan *et al.*, "Aqueous Magnesium Zinc Hybrid Battery: An Advanced High-Voltage and High-Energy $MgMn_2O_4$ Cathode," (in en), *ACS Energy Letters,* vol. 3, no. 8, pp. 1998–2004, 2018–08–10 2018, doi: 10.1021/acsenergylett.8b01105.

[20] G. Fang *et al.*, "Suppressing Manganese Dissolution in Potassium Manganate with Rich Oxygen

Defects Engaged High-Energy-Density and Durable Aqueous Zinc-Ion Battery," (in en), *Advanced Functional Materials,* vol. 29, no. 15, p. 1808375, 04/2019 2019, doi: 10.1002/adfm.201808375.
[21] F. Zhao, J. Xue, W. Shao, H. Yu, W. Huang, and J. Xiao, "Toward high-sulfur-content, high-performance lithium-sulfur batteries: Review of materials and technologies," (in en), *Journal of Energy Chemistry,* vol. 80, pp. 625–657, 05/2023 2023, doi: 10.1016/j.jechem.2023.02.009.
[22] Z. Khan, M. Vagin, and X. Crispin, "Can Hybrid Na–Air Batteries Outperform Nonaqueous Na–O2 Batteries?," (in en), *Advanced Science,* vol. 7, no. 5, p. 1902866, 2020 2020, doi: 10.1002/advs.201902866.
[23] B. Qian *et al.*, "A Dual Photoelectrode Photoassisted Fe–Air Battery: The Photo-Electrocatalysis Mechanism Accounting for the Improved Oxygen Evolution Reaction and Oxygen Reduction Reaction of Air Electrodes," (in en), *Small,* vol. 18, no. 7, p. 2103933, 2022 2022, doi: 10.1002/smll.202103933.
[24] L. Qin, N. Xiao, S. Zhang, X. Chen, and Y. Wu, "From K-O2 to K-Air Batteries: Realizing Superoxide Batteries on the Basis of Dry Ambient Air," (in en), *Angewandte Chemie International Edition,* vol. 59, no. 26, pp. 10498–10501, 2020 2020, doi: 10.1002/anie.202003481.
[25] M. Wei *et al.*, "A high-performance Al-air fuel cell using a mesh-encapsulated anode via Al–Zn energy transfer," (in en), *iScience,* vol. 24, no. 11, 2021 2021, doi: 10.1016/j.isci.2021.103259.
[26] P. Jiang *et al.*, "A micro-alloyed Mg-Zn-Ge alloy as promising anode for primary Mg-air batteries," (in en), *Journal of Magnesium and Alloys,* 2023 2023, doi: 10.1016/j.jma.2023.05.004.
[27] P. Chen *et al.*, "Recent Progress in Electrolytes for Zn–Air Batteries," (in en), *Frontiers in Chemistry,* vol. 8, p. 372, 2020–5–26 2020, doi: 10.3389/fchem.2020.00372.
[28] A. Kraytsberg and Y. Ein-Eli, "Review on Li–air batteries—Opportunities, limitations and perspective," (in en), *Journal of Power Sources,* vol. 196, no. 3, pp. 886–893, 2011–02–01 2011, doi: 10.1016/j.jpowsour.2010.09.031.
[29] C. Shunhong, S. Pullteap, and T. Mao, "Research Progress and Future Expectations in Anode of Secondary Zinc-Air Batteries: A Review," (in en), *Applied Science and Engineering Progress,* 2024–6–21 2024, doi: 10.14416/j.asep.2024.06.006.
[30] J. Goldstein, I. Brown, and B. Koretz, "New developments in the Electric Fuel Ltd. zinc/air system," (in en), *Journal of Power Sources,* vol. 80, no. 1, pp. 171–179, 1999–07–01 1999, doi: 10.1016/S0378-7753(98)00260-2.
[31] J. Yi *et al.*, "Challenges, mitigation strategies and perspectives in development of zinc-electrode materials and fabrication for rechargeable zinc–air batteries," (in en), *Energy & Environmental Science,* vol. 11, no. 11, pp. 3075–3095, 2018–11–07 2018, doi: 10.1039/C8EE01991F.
[32] T. Placke, R. Kloepsch, S. Dühnen, and M. Winter, "Lithium ion, lithium metal, and alternative rechargeable battery technologies: the odyssey for high energy density," (in en), *Journal of Solid State Electrochemistry,* vol. 21, no. 7, pp. 1939–1964, 2017–07–01 2017, doi: 10.1007/s10008-017-3610-7.
[33] M. Wang, F. Zhang, C.-S. Lee, and Y. Tang, "Low-Cost Metallic Anode Materials for High Performance Rechargeable Batteries," *Advanced Energy Materials,* vol. 7, no. 23, p. 1700536, 2017–12 2017, doi: 10.1002/aenm.201700536.
[34] J. F. Parker *et al.*, "Rechargeable nickel–3D zinc batteries: An energy-dense, safer alternative to lithium-ion," (in EN), *Science,* 2017–04–28 2017, doi: 10.1126/science.aak9991.
[35] J. F. Parker, J. S. Ko, D. R. Rolison, and J. W. Long, "Translating Materials-Level Performance into Device-Relevant Metrics for Zinc-Based Batteries," (in en), *Joule,* vol. 2, no. 12, pp. 2519–2527, 2018–12–19 2018, doi: 10.1016/j.joule.2018.11.007.
[36] Y. Li *et al.*, "Advanced zinc-air batteries based on high-performance hybrid electrocatalysts," (in en), *Nature Communications,* vol. 4, no. 1, p. 1805, 2013–05–07 2013, doi: 10.1038/ncomms2812.
[37] G. W. Heise and E. A. Schumacher, "An Air-Depolarized Primary Cell with Caustic Alkali Electrolyte," (in en), *Transactions of The Electrochemical Society,* vol. 62, no. 1, p. 383, 1932–01–01 1932, doi: 10.1149/1.3493794.
[38] R. P. Hamlen, E. C. Jerabek, J. C. Ruzzo, and E. G. Siwek, "Anodes for Refuelable Magnesium-Air Batteries," (in en), *Journal of The Electrochemical Society,* vol. 116, no. 11, p. 1588, 1969–11–01 1969, doi: 10.1149/1.2411622.
[39] C. Mou *et al.*, "Construction of a self-supported dendrite-free zinc anode for high-performance zinc-air batteries," (in en), *Inorganic Chemistry Frontiers,* vol. 10, no. 10, pp. 3082–3090, 2023 2023, doi: 10.1039/d3qi00279a.
[40] J. Zheng *et al.*, "Reversible epitaxial electrodeposition of metals in battery anodes," (in en),

Science, vol. 366, no. 6465, pp. 645–648, 2019–11 2019, doi: 10.1126/science.aax6873.
[41] C. Sparkes and N. K. Lacey, "A study of mercuric oxide and zinc-air battery life in hearing aids," (in en), *The Journal of Laryngology & Otology,* vol. 111, no. 9, pp. 814–819, 1997/09 1997, doi: 10.1017/S002221510013871X.
[42] V. Caramia and B. Bozzini, "Materials science aspects of zinc–air batteries: a review," (in en), *Materials for Renewable and Sustainable Energy,* vol. 3, no. 2, p. 28, 2014–04–03 2014, doi: 10.1007/s40243-014-0028-3.
[43] N.-n. Xu and J. Qiao, "Recent Progress in Bifunctional Catalysts for Zinc-Air Batteries," (in en), *Journal of Electrochemistry,* vol. 26(4), pp. 531–562, 2020.
[44] J. R. Goldstein and B. Koretz, "Tests of a full-sized mechanically rechargeable zinc-air battery in an electric vehicle," (in en), *IEEE Aerospace and Electronic Systems Magazine,* vol. 8, no. 11, pp. 34–38, 1993–11 1993, doi: 10.1109/62.242061.
[45] N. Kadam and A. Sarkar, "A high voltage zinc–air battery with two isolated electrolytes and moving auxiliary electrodes," (in en), *Applied Energy,* vol. 344, p. 121309, 2023–08–15 2023, doi: 10.1016/j.apenergy.2023.121309.
[46] X. Yuan *et al.*, "Inhibition of zinc dendrite growth in zinc-air batteries by alloying the anode with Ce and Yb," (in en), *Journal of Alloys and Compounds,* vol. 970, 2024 2024, doi: 10.1016/j.jallcom.2023.172523.
[47] K. A. J. Dilshad and M. K. Rabinal, "Rationally Designed Zn-Anode and Co3O4-Cathode Nanoelectrocatalysts for an Efficient Zn-Air Battery," (in en), *Energy and Fuels,* vol. 35, no. 15, pp. 12588–12598, 2021 2021, doi: 10.1021/acs.energyfuels.1c01108.
[48] P. Pei, K. Wang, and Z. Ma, "Technologies for extending zinc–air battery's cyclelife: A review," (in en), *Applied Energy,* vol. 128, pp. 315–324, 2014–09–01 2014, doi: 10.1016/j.apenergy.2014.04.095.
[49] X. Chen, Z. Zhou, H. E. Karahan, Q. Shao, L. Wei, and Y. Chen, "Recent Advances in Materials and Design of Electrochemically Rechargeable Zinc–Air Batteries," (in en), *Small,* vol. 14, no. 44, p. 1801929, 2018 2018, doi: 10.1002/smll.201801929.
[50] J. Pan, Y. Y. Xu, H. Yang, Z. Dong, H. Liu, and B. Y. Xia, "Advanced Architectures and Relatives of Air Electrodes in Zn–Air Batteries," (in en), *Advanced Science,* vol. 5, no. 4, p. 1700691, 2018 2018, doi: 10.1002/advs.201700691.
[51] D. Yang, J. Li, C. Liu, J. Ge, W. Xing, and J. Zhu, "Regulating the MXene-Zinc Interfacial Structure toward a Highly Revisable Metal Anode of Zinc-Air Batteries," (in en), *ACS Applied Materials and Interfaces,* vol. 15, no. 8, pp. 10651–10659, 2023 2023, doi: 10.1021/acsami.2c20701.
[52] S. K. Yadav, D. Deckenbach, and J. J. Schneider, "Secondary Zinc–Air Batteries: A View on Rechargeability Aspects," (in en), *Batteries,* vol. 8, no. 11, p. 244, 2022–11–17 2022, doi: 10.3390/batteries8110244.
[53] D. Deckenbach and J. J. Schneider, "A 3D hierarchically porous nanoscale ZnO anode for high-energy rechargeable zinc-air batteries," (in en), *Journal of Power Sources,* vol. 488, 2021 2021, doi: 10.1016/j.jpowsour.2020.229393.
[54] G. Nazir *et al.*, "A Review of Rechargeable Zinc–Air Batteries: Recent Progress and Future Perspectives," (in en), *Nano-Micro Letters,* vol. 16, no. 1, p. 138, 2024–02–29 2024, doi: 10.1007/s40820-024-01328-1.
[55] R. Yuksel, O. Buyukcakir, W. K. Seong, and R. S. Ruoff, "Metal-Organic Framework Integrated Anodes for Aqueous Zinc-Ion Batteries," (in en), *Advanced Energy Materials,* vol. 10, no. 16, p. 1904215, 04/2020 2020, doi: 10.1002/aenm.201904215.
[56] P. Zhang *et al.*, "Bifunctional Single Atom Catalysts for Rechargeable Zinc–Air Batteries: From Dynamic Mechanism to Rational Design," (in en), *Advanced Materials,* p. 2303243, 2023–06–30 2023, doi: 10.1002/adma.202303243.
[57] Y. Zhang *et al.*, "Deeply Rechargeable and Hydrogen-Evolution-Suppressing Zinc Anode in Alkaline Aqueous Electrolyte," (in en), *Nano Letters,* vol. 20, no. 6, pp. 4700–4707, 2020–06–10 2020, doi: 10.1021/acs.nanolett.0c01776.
[58] Q. Zhang *et al.*, "Revealing the role of crystal orientation of protective layers for stable zinc anode," (in en), *Nature Communications,* vol. 11, no. 1, p. 3961, 2020–08–07 2020, doi: 10.1038/s41467-020-17752-x.
[59] S.-B. Wang *et al.*, "Lamella-nanostructured eutectic zinc–aluminum alloys as reversible and dendrite-free anodes for aqueous rechargeable batteries," (in en), *Nature Communications,* vol. 11,

no. 1, p. 1634, 2020–04–02 2020, doi: 10.1038/s41467-020-15478-4.
[60] C. Li *et al.*, "Spatially homogeneous copper foam as surface dendrite-free host for zinc metal anode," (in en), *Chemical Engineering Journal,* vol. 379, p. 122248, 01/2020 2020, doi: 10.1016/j.cej.2019.122248.
[61] S.-M. Lee, Y.-J. Kim, S.-W. Eom, N.-S. Choi, K.-W. Kim, and S.-B. Cho, "Improvement in self-discharge of Zn anode by applying surface modification for Zn–air batteries with high energy density," (in en), *Journal of Power Sources,* vol. 227, pp. 177–184, 04/2013 2013, doi: 10.1016/j.jpowsour.2012.11.046.
[62] A. Wang *et al.*, "Fast-Charging Zn–Air Batteries with Long Lifetime Enabled by Reconstructed Amorphous Multi-Metallic Sulfide," (in en), *Advanced Materials,* vol. 34, no. 49, p. 2204247, 12/2022 2022, doi: 10.1002/adma.202204247.
[63] H.-I. Kim, E.-J. Kim, S.-J. Kim, and H.-C. Shin, "Influence of ZnO precipitation on the cycling stability of rechargeable Zn–air batteries," (in en), *Journal of Applied Electrochemistry,* vol. 45, no. 4, pp. 335–342, 4/2015 2015, doi: 10.1007/s10800-015-0793-4.
[64] M. A. Deyab and G. Mele, "Polyaniline/Zn-phthalocyanines nanocomposite for protecting zinc electrode in Zn-air battery," (in en), *Journal of Power Sources,* vol. 443, p. 227264, 12/2019 2019, doi: 10.1016/j.jpowsour.2019.227264.
[65] C. Yang, Z. Zhang, Z. Tian, K. Zhang, J. Li, and Y. Lai, "Polydopamine-coated nano-ZnO for high-performance rechargeable Zn–Ni battery," (in en), *Materials Letters,* vol. 197, pp. 163–166, 06/2017 2017, doi: 10.1016/j.matlet.2017.03.088.
[66] J. Newman and N. P. Balsara, *Electrochemical Systems*. John Wiley & Sons (in en), 2021, p. 608.
[67] J. F. Parker, E. S. Nelson, M. D. Wattendorf, C. N. Chervin, J. W. Long, and D. R. Rolison, "Retaining the 3D framework of zinc sponge anodes upon deep discharge in Zn-Air cells," (in en), *ACS Applied Materials and Interfaces,* vol. 6, no. 22, pp. 19471–19476, 2014 2014, doi: 10.1021/am505266c.
[68] D. Stock, S. Dongmo, K. Miyazaki, T. Abe, J. Janek, and D. Schröder, "Towards zinc-oxygen batteries with enhanced cycling stability: The benefit of anion-exchange ionomer for zinc sponge anodes," (in en), *Journal of Power Sources,* vol. 395, pp. 195–204, 2018 2018, doi: 10.1016/j.jpowsour.2018.05.079.
[69] M. Al-Abbasi *et al.*, "Challenges and protective strategies on zinc anode toward practical aqueous zinc-ion batteries," (in en), *Carbon Neutralization,* vol. 3, no. 1, pp. 108–141, 2024 2024, doi: 10.1002/cnl2.109.
[70] E. Davari, A. D. Johnson, A. Mittal, M. Xiong, and D. G. Ivey, "Manganese-cobalt mixed oxide film as a bifunctional catalyst for rechargeable zinc-air batteries," *Electrochimica Acta,* vol. 211, pp. 735–743, 2016–09–01 2016, doi: 10.1016/j.electacta.2016.06.085.
[71] K. Wang *et al.*, "Zn–Ni reaction in the alkaline zinc-air battery using a nickel-supported air electrode," (in en), *Materials Today Energy,* vol. 21, p. 100823, 09/2021 2021, doi: 10.1016/j.mtener.2021.100823.
[72] S. Qu *et al.*, "3D Foam Anode and Hydrogel Electrolyte for High-Performance and Stable Flexible Zinc–Air Battery," (in en), *ChemistrySelect,* vol. 5, no. 27, pp. 8305–8310, 2020–07–23 2020, doi: 10.1002/slct.202002573.
[73] K. Xu *et al.*, "A three-dimensional zincophilic nano-copper host enables dendrite-free and anode-free Zn batteries," (in en), *Materials Today Energy,* vol. 34, p. 101284, 06/2023 2023, doi: 10.1016/j.mtener.2023.101284.
[74] M. He *et al.*, "Manipulating the ion-transference and deposition kinetics by regulating the surface chemistry of zinc metal anodes for rechargeable zinc-air batteries," (in en), *Green Energy and Environment,* vol. 8, no. 1, pp. 318–330, 2023 2023, doi: 10.1016/j.gee.2021.04.011.

APPENDICES

Appendix A: Battery Performance Test Data

All data presented in this appendix are derived from the raw measurement results of the open-circuit and load tests of the zinc–air batteries. The original data were continuously recorded at 2 s intervals. For the sake of layout and readability, the tables in this appendix have been uniformly down-sampled to a time step of 90 s, while preserving the representative variation trends of the four cells—StZnB, Zn3B, Zn4B, and Zn5B—throughout the tests. Each worksheet corresponds to specific parameters such as open-circuit voltage, load voltage, and load current. The data are provided solely for archival reference and comparison with the original measurements.

Table A1 Open-circuit voltage test data

Time (s)	StZnB	Zn3B	Zn4B	Zn5B
0	1.372	1.386	1.396	1.392
90	1.372	1.386	1.396	1.392
180	1.372	1.386	1.396	1.392
270	1.372	1.386	1.396	1.392
360	1.372	1.386	1.396	1.392
450	1.372	1.386	1.396	1.392
540	1.372	1.386	1.396	1.392
630	1.372	1.386	1.396	1.392
720	1.372	1.386	1.396	1.392
810	1.372	1.385	1.396	1.391
900	1.372	1.385	1.396	1.391
990	1.372	1.385	1.396	1.391
1080	1.372	1.385	1.396	1.391
1170	1.372	1.385	1.396	1.391
1260	1.372	1.385	1.396	1.391
1350	1.372	1.385	1.396	1.39
1440	1.372	1.384	1.395	1.39
1530	1.372	1.384	1.395	1.39
1620	1.372	1.384	1.395	1.39
1710	1.372	1.384	1.395	1.389
1800	1.371	1.383	1.395	1.389
1890	1.371	1.383	1.395	1.389
1980	1.371	1.383	1.395	1.389
2070	1.371	1.383	1.395	1.388
2160	1.371	1.382	1.395	1.388
2250	1.371	1.382	1.395	1.388
2340	1.371	1.382	1.395	1.387

Time (s)	StZnB	Zn3B	Zn4B	Zn5B
2430	1.371	1.381	1.395	1.387
2520	1.371	1.381	1.394	1.387
2610	1.371	1.381	1.394	1.386
2700	1.371	1.381	1.394	1.386
2790	1.371	1.38	1.394	1.386
2880	1.371	1.38	1.394	1.385
2970	1.371	1.38	1.394	1.385
3060	1.371	1.379	1.394	1.385
3150	1.37	1.379	1.394	1.384
3240	1.37	1.379	1.393	1.384
3330	1.37	1.378	1.393	1.384
3420	1.37	1.378	1.393	1.383
3510	1.37	1.378	1.393	1.383
3600	1.37	1.377	1.393	1.382
3690	1.37	1.377	1.393	1.382
3780	1.37	1.377	1.393	1.382
3870	1.37	1.376	1.393	1.381
3960	1.37	1.376	1.392	1.381
4050	1.37	1.375	1.392	1.381
4140	1.37	1.375	1.392	1.38
4230	1.37	1.375	1.392	1.38
4320	1.369	1.374	1.392	1.379
4410	1.369	1.374	1.392	1.379
4500	1.369	1.374	1.392	1.379
4590	1.369	1.374	1.391	1.378
4680	1.369	1.373	1.391	1.378
4770	1.369	1.373	1.391	1.378
4860	1.369	1.373	1.391	1.377
4950	1.369	1.372	1.391	1.377
5040	1.369	1.372	1.391	1.377
5130	1.369	1.372	1.391	1.376
5220	1.369	1.371	1.391	1.376
5310	1.368	1.371	1.39	1.376
5400	1.368	1.371	1.39	1.376

Time (s)	StZnB	Zn3B	Zn4B	Zn5B
5490	1.368	1.371	1.39	1.375
5580	1.368	1.371	1.39	1.375
5670	1.368	1.37	1.39	1.375
5760	1.368	1.37	1.39	1.375
5850	1.368	1.37	1.39	1.374
5940	1.368	1.37	1.389	1.374
6030	1.368	1.37	1.389	1.374
6120	1.368	1.369	1.389	1.374
6210	1.368	1.369	1.389	1.374
6300	1.368	1.369	1.389	1.374
6390	1.368	1.369	1.389	1.373
6480	1.367	1.369	1.389	1.373
6570	1.367	1.369	1.389	1.373
6660	1.367	1.369	1.389	1.373
6750	1.367	1.369	1.388	1.373
6840	1.367	1.369	1.388	1.373
6930	1.367	1.368	1.388	1.373
7020	1.367	1.368	1.388	1.373
7110	1.367	1.368	1.388	1.373
7200	1.367	1.368	1.388	1.373
7290	1.367	1.368	1.388	1.373
7380	1.367	1.368	1.388	1.373
7470	1.367	1.368	1.388	1.373
7560	1.367	1.368	1.388	1.373
7650	1.367	1.368	1.388	1.373
7740	1.367	1.368	1.388	1.373
7830	1.367	1.368	1.388	1.373
7920	1.367	1.368	1.388	1.373
8010	1.367	1.368	1.387	1.373
8100	1.367	1.368	1.387	1.373
8190	1.367	1.368	1.387	1.373
8280	1.367	1.368	1.387	1.373
8370	1.367	1.368	1.387	1.373
8460	1.367	1.368	1.387	1.373

Time (s)	StZnB	Zn3B	Zn4B	Zn5B
8550	1.367	1.368	1.387	1.373
8640	1.367	1.368	1.387	1.372
8730	1.367	1.368	1.387	1.372
8820	1.367	1.368	1.387	1.372
8910	1.367	1.368	1.387	1.372
9000	1.366	1.368	1.387	1.372
9090	1.366	1.368	1.387	1.372
9180	1.366	1.368	1.387	1.372
9270	1.366	1.368	1.387	1.372
9360	1.366	1.368	1.387	1.372
9450	1.366	1.368	1.387	1.372
9540	1.366	1.367	1.387	1.372
9630	1.366	1.367	1.387	1.372
9720	1.366	1.367	1.387	1.372
9810	1.366	1.367	1.387	1.372
9900	1.366	1.367	1.387	1.372
9990	1.366	1.367	1.387	1.372
10080	1.366	1.367	1.387	1.372
10170	1.366	1.367	1.387	1.372
10260	1.366	1.367	1.387	1.371
10350	1.366	1.367	1.387	1.371
10440	1.366	1.367	1.387	1.371
10530	1.366	1.367	1.387	1.371
10620	1.366	1.366	1.387	1.371
10710	1.366	1.366	1.387	1.371
10800	1.366	1.366	1.387	1.371
10890	1.366	1.366	1.387	1.371
10980	1.366	1.366	1.387	1.371
11070	1.366	1.366	1.386	1.371
11160	1.366	1.366	1.386	1.371
11250	1.366	1.366	1.386	1.37
11340	1.366	1.366	1.386	1.37
11430	1.366	1.366	1.386	1.37
11520	1.366	1.365	1.386	1.37

Time (s)	StZnB	Zn3B	Zn4B	Zn5B
11610	1.366	1.365	1.386	1.37
11700	1.366	1.365	1.386	1.37
11790	1.366	1.365	1.386	1.37
11880	1.366	1.365	1.386	1.37
11970	1.366	1.365	1.386	1.37
12060	1.366	1.365	1.386	1.37
12150	1.366	1.365	1.386	1.369
12240	1.366	1.364	1.385	1.369
12330	1.366	1.364	1.385	1.369
12420	1.366	1.364	1.385	1.369
12510	1.366	1.364	1.385	1.369
12600	1.365	1.364	1.385	1.369
12690	1.365	1.364	1.385	1.369
12780	1.365	1.364	1.385	1.369
12870	1.365	1.364	1.385	1.368
12960	1.365	1.363	1.385	1.368
13050	1.365	1.363	1.385	1.368
13140	1.365	1.363	1.384	1.368
13230	1.365	1.363	1.384	1.368
13320	1.365	1.363	1.384	1.368
13410	1.365	1.363	1.384	1.368
13500	1.365	1.363	1.384	1.368
13590	1.365	1.362	1.384	1.368
13680	1.365	1.362	1.384	1.367
13770	1.365	1.362	1.384	1.367
13860	1.365	1.362	1.384	1.367
13950	1.365	1.362	1.383	1.367
14040	1.365	1.362	1.383	1.367
14130	1.365	1.362	1.383	1.367
14220	1.364	1.361	1.383	1.367
14310	1.364	1.361	1.383	1.367
14400	1.364	1.361	1.383	1.366
14490	1.364	1.361	1.383	1.366
14580	1.364	1.361	1.383	1.366

Time (s)	StZnB	Zn3B	Zn4B	Zn5B
14670	1.364	1.361	1.382	1.366
14760	1.364	1.361	1.382	1.366
14850	1.364	1.36	1.382	1.366
14940	1.364	1.36	1.382	1.366
15030	1.364	1.36	1.382	1.366
15120	1.364	1.36	1.382	1.365
15210	1.364	1.36	1.382	1.365
15300	1.364	1.36	1.382	1.365
15390	1.364	1.36	1.381	1.365
15480	1.364	1.36	1.381	1.365
15570	1.364	1.359	1.381	1.365
15660	1.364	1.359	1.381	1.365
15750	1.363	1.359	1.381	1.365
15840	1.363	1.359	1.381	1.364
15930	1.363	1.359	1.381	1.364
16020	1.363	1.359	1.381	1.364
16110	1.363	1.359	1.38	1.364
16200	1.363	1.358	1.38	1.364
16290	1.363	1.358	1.38	1.364
16380	1.363	1.358	1.38	1.364
16470	1.363	1.358	1.38	1.364
16560	1.363	1.358	1.38	1.363
16650	1.363	1.358	1.38	1.363
16740	1.363	1.358	1.38	1.363
16830	1.363	1.358	1.38	1.363
16920	1.363	1.357	1.379	1.363
17010	1.363	1.357	1.379	1.363
17100	1.363	1.357	1.379	1.363
17190	1.363	1.357	1.379	1.363
17280	1.362	1.357	1.379	1.363
17370	1.362	1.357	1.379	1.363
17460	1.362	1.357	1.379	1.362
17550	1.362	1.357	1.379	1.362
17640	1.362	1.357	1.379	1.362

Time (s)	StZnB	Zn3B	Zn4B	Zn5B
17730	1.362	1.356	1.378	1.362
17820	1.362	1.356	1.378	1.362
17910	1.362	1.356	1.378	1.362
18000	1.362	1.356	1.378	1.362
18090	1.362	1.356	1.378	1.362
18180	1.362	1.356	1.378	1.362
18270	1.362	1.356	1.378	1.362
18360	1.362	1.356	1.378	1.362
18450	1.362	1.356	1.378	1.361
18540	1.362	1.356	1.378	1.361
18630	1.362	1.355	1.377	1.361
18720	1.362	1.355	1.377	1.361
18810	1.362	1.355	1.377	1.361
18900	1.362	1.355	1.377	1.361
18990	1.362	1.355	1.377	1.361
19080	1.362	1.355	1.377	1.361
19170	1.361	1.355	1.377	1.361
19260	1.361	1.355	1.377	1.361
19350	1.361	1.355	1.377	1.361
19440	1.361	1.355	1.377	1.361
19530	1.361	1.355	1.377	1.361
19620	1.361	1.355	1.377	1.361
19710	1.361	1.355	1.377	1.361
19800	1.361	1.355	1.377	1.36
19890	1.361	1.354	1.377	1.36
19980	1.361	1.354	1.376	1.36
20070	1.361	1.354	1.376	1.36
20160	1.361	1.354	1.376	1.36
20250	1.361	1.354	1.376	1.36
20340	1.361	1.354	1.376	1.36
20430	1.361	1.354	1.376	1.36
20520	1.361	1.354	1.376	1.36
20610	1.361	1.354	1.376	1.36
20700	1.361	1.354	1.376	1.36

Time (s)	StZnB	Zn3B	Zn4B	Zn5B
20790	1.361	1.354	1.376	1.36
20880	1.361	1.354	1.376	1.36
20970	1.361	1.354	1.376	1.36
21060	1.361	1.354	1.376	1.36
21150	1.361	1.354	1.376	1.36
21240	1.361	1.354	1.376	1.36
21330	1.361	1.354	1.376	1.36
21420	1.361	1.354	1.376	1.36
21510	1.361	1.354	1.376	1.36

Table A2 Load voltage test data

Time (s)	StZnB	Zn3B	Zn4B	Zn5B
0	1.191	1.167	1.213	1.196
90	1.191	1.167	1.213	1.196
180	1.191	1.167	1.213	1.196
270	1.191	1.167	1.213	1.196
360	1.191	1.167	1.213	1.196
450	1.191	1.166	1.213	1.196
540	1.191	1.166	1.213	1.195
630	1.191	1.166	1.213	1.195
720	1.19	1.165	1.212	1.195
810	1.19	1.165	1.212	1.195
900	1.19	1.165	1.212	1.194
990	1.19	1.164	1.212	1.194
1080	1.19	1.164	1.212	1.194
1170	1.189	1.163	1.211	1.193
1260	1.189	1.162	1.211	1.193
1350	1.189	1.162	1.211	1.193
1440	1.189	1.161	1.211	1.192
1530	1.188	1.16	1.21	1.192
1620	1.188	1.16	1.21	1.191
1710	1.188	1.159	1.21	1.191
1800	1.187	1.158	1.209	1.19
1890	1.187	1.157	1.209	1.19

Time (s)	StZnB	Zn3B	Zn4B	Zn5B
1980	1.187	1.156	1.209	1.189
2070	1.186	1.155	1.208	1.188
2160	1.186	1.154	1.208	1.188
2250	1.185	1.153	1.207	1.187
2340	1.185	1.152	1.207	1.186
2430	1.184	1.151	1.207	1.186
2520	1.184	1.15	1.206	1.185
2610	1.184	1.149	1.206	1.184
2700	1.183	1.148	1.205	1.184
2790	1.183	1.147	1.205	1.183
2880	1.182	1.146	1.204	1.182
2970	1.182	1.145	1.204	1.181
3060	1.181	1.144	1.203	1.181
3150	1.18	1.142	1.203	1.18
3240	1.18	1.141	1.202	1.179
3330	1.179	1.14	1.202	1.178
3420	1.179	1.139	1.201	1.177
3510	1.178	1.138	1.2	1.177
3600	1.178	1.136	1.2	1.176
3690	1.177	1.135	1.199	1.175
3780	1.176	1.134	1.199	1.174
3870	1.176	1.133	1.198	1.173
3960	1.175	1.132	1.198	1.172
4050	1.175	1.131	1.197	1.172
4140	1.174	1.129	1.196	1.171
4230	1.173	1.128	1.196	1.17
4320	1.173	1.127	1.195	1.169
4410	1.172	1.126	1.195	1.168
4500	1.171	1.125	1.194	1.168
4590	1.171	1.124	1.193	1.167
4680	1.17	1.123	1.193	1.166
4770	1.169	1.122	1.192	1.165
4860	1.169	1.121	1.192	1.164
4950	1.168	1.12	1.191	1.164

Time (s)	StZnB	Zn3B	Zn4B	Zn5B
5040	1.167	1.119	1.19	1.163
5130	1.167	1.118	1.19	1.162
5220	1.166	1.117	1.189	1.162
5310	1.166	1.116	1.189	1.161
5400	1.165	1.115	1.188	1.16
5490	1.164	1.114	1.188	1.16
5580	1.164	1.113	1.187	1.159
5670	1.163	1.113	1.186	1.158
5760	1.162	1.112	1.186	1.158
5850	1.162	1.111	1.185	1.157
5940	1.161	1.11	1.185	1.157
6030	1.161	1.11	1.184	1.156
6120	1.16	1.109	1.184	1.156
6210	1.159	1.109	1.183	1.155
6300	1.159	1.108	1.183	1.155
6390	1.158	1.108	1.182	1.154
6480	1.158	1.107	1.182	1.154
6570	1.157	1.107	1.181	1.153
6660	1.157	1.107	1.181	1.153
6750	1.156	1.107	1.181	1.153
6840	1.155	1.106	1.18	1.153
6930	1.155	1.106	1.18	1.152
7020	1.154	1.106	1.179	1.152
7110	1.154	1.106	1.179	1.152
7200	1.153	1.106	1.179	1.152
7290	1.153	1.106	1.178	1.152
7380	1.153	1.106	1.178	1.151
7470	1.152	1.106	1.178	1.151
7560	1.152	1.106	1.177	1.151
7650	1.151	1.106	1.177	1.151
7740	1.151	1.106	1.177	1.151
7830	1.151	1.106	1.177	1.151
7920	1.15	1.106	1.176	1.151
8010	1.15	1.106	1.176	1.151

Time (s)	StZnB	Zn3B	Zn4B	Zn5B
8100	1.149	1.105	1.176	1.151
8190	1.149	1.105	1.176	1.151
8280	1.149	1.105	1.176	1.151
8370	1.149	1.105	1.175	1.151
8460	1.148	1.105	1.175	1.151
8550	1.148	1.105	1.175	1.151
8640	1.148	1.105	1.175	1.15
8730	1.148	1.105	1.175	1.15
8820	1.147	1.104	1.175	1.15
8910	1.147	1.104	1.175	1.15
9000	1.147	1.104	1.175	1.15
9090	1.147	1.104	1.175	1.15
9180	1.147	1.104	1.175	1.149
9270	1.147	1.103	1.175	1.149
9360	1.147	1.103	1.175	1.149
9450	1.147	1.103	1.175	1.149
9540	1.147	1.103	1.175	1.148
9630	1.147	1.103	1.175	1.148
9720	1.146	1.102	1.175	1.148
9810	1.146	1.102	1.175	1.148
9900	1.146	1.102	1.175	1.147
9990	1.146	1.101	1.174	1.147
10080	1.146	1.101	1.174	1.147
10170	1.146	1.101	1.174	1.146
10260	1.146	1.101	1.174	1.146
10350	1.146	1.1	1.174	1.145
10440	1.146	1.1	1.174	1.145
10530	1.146	1.1	1.174	1.145
10620	1.146	1.099	1.173	1.144
10710	1.146	1.099	1.173	1.144
10800	1.146	1.099	1.173	1.143
10890	1.145	1.098	1.173	1.143
10980	1.145	1.098	1.173	1.143
11070	1.145	1.098	1.173	1.142

Time (s)	StZnB	Zn3B	Zn4B	Zn5B
11160	1.145	1.097	1.172	1.142
11250	1.145	1.097	1.172	1.141
11340	1.144	1.096	1.172	1.141
11430	1.144	1.096	1.172	1.14
11520	1.144	1.096	1.171	1.14
11610	1.144	1.095	1.171	1.139
11700	1.144	1.095	1.171	1.139
11790	1.143	1.094	1.171	1.138
11880	1.143	1.094	1.17	1.138
11970	1.143	1.094	1.17	1.137
12060	1.142	1.093	1.17	1.136
12150	1.142	1.093	1.169	1.136
12240	1.142	1.092	1.169	1.135
12330	1.141	1.092	1.169	1.135
12420	1.141	1.091	1.168	1.134
12510	1.141	1.091	1.168	1.134
12600	1.14	1.091	1.168	1.133
12690	1.14	1.09	1.168	1.132
12780	1.14	1.09	1.167	1.132
12870	1.139	1.089	1.167	1.131
12960	1.139	1.089	1.166	1.131
13050	1.138	1.088	1.166	1.13
13140	1.138	1.088	1.166	1.129
13230	1.138	1.087	1.165	1.129
13320	1.137	1.087	1.165	1.128
13410	1.137	1.086	1.165	1.127
13500	1.136	1.086	1.164	1.127
13590	1.136	1.085	1.164	1.126
13680	1.135	1.085	1.163	1.126
13770	1.135	1.084	1.163	1.125
13860	1.134	1.084	1.163	1.124
13950	1.134	1.083	1.162	1.124
14040	1.133	1.083	1.162	1.123
14130	1.133	1.082	1.161	1.122

Time (s)	StZnB	Zn3B	Zn4B	Zn5B
14220	1.133	1.082	1.161	1.122
14310	1.132	1.081	1.161	1.121
14400	1.132	1.081	1.16	1.12
14490	1.131	1.08	1.16	1.12
14580	1.131	1.08	1.159	1.119
14670	1.13	1.08	1.159	1.118
14760	1.129	1.079	1.159	1.118
14850	1.129	1.079	1.158	1.117
14940	1.128	1.078	1.158	1.116
15030	1.128	1.078	1.157	1.116
15120	1.127	1.077	1.157	1.115
15210	1.127	1.077	1.156	1.114
15300	1.126	1.076	1.156	1.114
15390	1.126	1.076	1.156	1.113
15480	1.125	1.075	1.155	1.112
15570	1.125	1.075	1.155	1.112
15660	1.124	1.074	1.154	1.111
15750	1.124	1.074	1.154	1.11
15840	1.123	1.073	1.153	1.11
15930	1.123	1.073	1.153	1.109
16020	1.122	1.072	1.153	1.109
16110	1.122	1.072	1.152	1.108
16200	1.121	1.071	1.152	1.107
16290	1.121	1.071	1.151	1.107
16380	1.12	1.071	1.151	1.106
16470	1.12	1.07	1.151	1.105
16560	1.119	1.07	1.15	1.105
16650	1.118	1.069	1.15	1.104
16740	1.118	1.069	1.149	1.104
16830	1.117	1.068	1.149	1.103
16920	1.117	1.068	1.149	1.103
17010	1.116	1.068	1.148	1.102
17100	1.116	1.067	1.148	1.101
17190	1.115	1.067	1.147	1.101

Time (s)	StZnB	Zn3B	Zn4B	Zn5B
17280	1.115	1.066	1.147	1.1
17370	1.115	1.066	1.147	1.1
17460	1.114	1.066	1.146	1.099
17550	1.114	1.065	1.146	1.099
17640	1.113	1.065	1.146	1.098
17730	1.113	1.064	1.145	1.098
17820	1.112	1.064	1.145	1.097
17910	1.112	1.064	1.144	1.097
18000	1.111	1.063	1.144	1.096
18090	1.111	1.063	1.144	1.096
18180	1.11	1.063	1.144	1.095
18270	1.11	1.062	1.143	1.095
18360	1.11	1.062	1.143	1.094
18450	1.109	1.062	1.143	1.094
18540	1.109	1.061	1.142	1.093
18630	1.109	1.061	1.142	1.093
18720	1.108	1.061	1.142	1.093
18810	1.108	1.06	1.141	1.092
18900	1.107	1.06	1.141	1.092
18990	1.107	1.06	1.141	1.091
19080	1.107	1.06	1.141	1.091
19170	1.106	1.059	1.14	1.091
19260	1.106	1.059	1.14	1.09
19350	1.106	1.059	1.14	1.09
19440	1.106	1.059	1.14	1.09
19530	1.105	1.059	1.139	1.089
19620	1.105	1.058	1.139	1.089
19710	1.105	1.058	1.139	1.089
19800	1.104	1.058	1.139	1.089
19890	1.104	1.058	1.139	1.088
19980	1.104	1.058	1.139	1.088
20070	1.104	1.057	1.138	1.088
20160	1.104	1.057	1.138	1.088
20250	1.103	1.057	1.138	1.087

Time (s)	StZnB	Zn3B	Zn4B	Zn5B
20340	1.103	1.057	1.138	1.087
20430	1.103	1.057	1.138	1.087
20520	1.103	1.057	1.138	1.087
20610	1.103	1.057	1.138	1.087
20700	1.103	1.056	1.137	1.087
20790	1.103	1.056	1.137	1.087
20880	1.102	1.056	1.137	1.086
20970	1.102	1.056	1.137	1.086
21060	1.102	1.056	1.137	1.086
21150	1.102	1.056	1.137	1.086
21240	1.102	1.056	1.137	1.086
21330	1.102	1.056	1.137	1.086
21420	1.102	1.056	1.137	1.086
21510	1.102	1.056	1.137	1.086

Table 3 Load current test data

Time(s)	StZnB	Zn3B	Zn4B	Zn5B
0	5.004	4.437	5.367	5.668
90	4.897	4.42	5.342	5.503
180	4.795	4.404	5.317	5.348
270	4.697	4.387	5.293	5.202
360	4.603	4.37	5.268	5.064
450	4.514	4.353	5.244	4.935
540	4.43	4.336	5.219	4.815
630	4.349	4.319	5.195	4.701
720	4.273	4.301	5.171	4.595
810	4.201	4.284	5.148	4.496
900	4.132	4.267	5.124	4.404
990	4.068	4.249	5.1	4.318
1080	4.007	4.231	5.077	4.239
1170	3.95	4.214	5.054	4.165
1260	3.896	4.196	5.031	4.097
1350	3.846	4.178	5.008	4.034
1440	3.799	4.16	4.985	3.977

Time(s)	StZnB	Zn3B	Zn4B	Zn5B
1530	3.756	4.142	4.963	3.925
1620	3.716	4.124	4.94	3.878
1710	3.679	4.106	4.918	3.835
1800	3.645	4.088	4.896	3.796
1890	3.614	4.07	4.874	3.761
1980	3.586	4.051	4.852	3.729
2070	3.56	4.033	4.831	3.7
2160	3.536	4.014	4.809	3.674
2250	3.514	3.996	4.788	3.65
2340	3.494	3.977	4.767	3.629
2430	3.476	3.958	4.746	3.61
2520	3.46	3.939	4.725	3.593
2610	3.445	3.921	4.704	3.578
2700	3.431	3.902	4.683	3.565
2790	3.419	3.883	4.663	3.553
2880	3.408	3.864	4.643	3.543
2970	3.398	3.845	4.623	3.534
3060	3.389	3.826	4.603	3.526
3150	3.381	3.807	4.583	3.519
3240	3.374	3.788	4.564	3.513
3330	3.368	3.768	4.544	3.508
3420	3.363	3.749	4.525	3.503
3510	3.358	3.73	4.506	3.499
3600	3.354	3.711	4.487	3.496
3690	3.35	3.692	4.468	3.493
3780	3.347	3.673	4.449	3.49
3870	3.344	3.653	4.43	3.487
3960	3.342	3.634	4.412	3.484
4050	3.34	3.615	4.394	3.482
4140	3.338	3.596	4.375	3.479
4230	3.336	3.577	4.357	3.475
4320	3.334	3.558	4.339	3.472
4410	3.332	3.539	4.322	3.468
4500	3.33	3.52	4.304	3.463

Time(s)	StZnB	Zn3B	Zn4B	Zn5B
4590	3.328	3.501	4.286	3.458
4680	3.326	3.482	4.269	3.452
4770	3.323	3.463	4.251	3.446
4860	3.32	3.444	4.234	3.44
4950	3.317	3.425	4.217	3.433
5040	3.313	3.407	4.2	3.426
5130	3.309	3.388	4.183	3.419
5220	3.305	3.369	4.166	3.411
5310	3.301	3.351	4.15	3.403
5400	3.296	3.332	4.133	3.395
5490	3.291	3.314	4.117	3.387
5580	3.286	3.296	4.101	3.378
5670	3.28	3.278	4.084	3.369
5760	3.274	3.26	4.068	3.36
5850	3.268	3.242	4.052	3.351
5940	3.262	3.225	4.037	3.341
6030	3.256	3.207	4.021	3.332
6120	3.249	3.19	4.005	3.323
6210	3.243	3.173	3.99	3.313
6300	3.236	3.156	3.974	3.303
6390	3.228	3.139	3.959	3.294
6480	3.221	3.123	3.944	3.284
6570	3.214	3.107	3.929	3.274
6660	3.206	3.09	3.914	3.265
6750	3.199	3.074	3.899	3.255
6840	3.191	3.059	3.884	3.246
6930	3.183	3.043	3.869	3.236
7020	3.175	3.028	3.854	3.227
7110	3.167	3.013	3.84	3.218
7200	3.159	2.998	3.826	3.208
7290	3.151	2.984	3.811	3.199
7380	3.142	2.969	3.797	3.19
7470	3.134	2.955	3.783	3.182
7560	3.126	2.94	3.769	3.173

Time(s)	StZnB	Zn3B	Zn4B	Zn5B
7650	3.117	2.926	3.755	3.164
7740	3.109	2.912	3.741	3.156
7830	3.1	2.897	3.727	3.148
7920	3.092	2.883	3.714	3.139
8010	3.083	2.87	3.7	3.131
8100	3.075	2.856	3.687	3.122
8190	3.066	2.842	3.673	3.114
8280	3.058	2.828	3.66	3.105
8370	3.049	2.815	3.647	3.097
8460	3.041	2.802	3.633	3.089
8550	3.032	2.788	3.62	3.08
8640	3.024	2.775	3.607	3.072
8730	3.016	2.762	3.594	3.064
8820	3.007	2.749	3.582	3.055
8910	2.999	2.737	3.569	3.047
9000	2.99	2.724	3.556	3.039
9090	2.982	2.711	3.544	3.03
9180	2.974	2.699	3.531	3.022
9270	2.966	2.687	3.518	3.014
9360	2.958	2.675	3.506	3.006
9450	2.949	2.663	3.493	2.998
9540	2.941	2.651	3.48	2.989
9630	2.933	2.639	3.468	2.981
9720	2.925	2.628	3.455	2.973
9810	2.917	2.616	3.443	2.965
9900	2.909	2.605	3.43	2.957
9990	2.901	2.594	3.417	2.949
10080	2.893	2.583	3.405	2.941
10170	2.885	2.572	3.393	2.933
10260	2.877	2.561	3.38	2.925
10350	2.869	2.551	3.368	2.917
10440	2.861	2.54	3.356	2.909
10530	2.853	2.53	3.344	2.901
10620	2.844	2.52	3.331	2.893

Time(s)	StZnB	Zn3B	Zn4B	Zn5B
10710	2.836	2.51	3.319	2.885
10800	2.828	2.5	3.307	2.877
10890	2.82	2.49	3.296	2.87
10980	2.812	2.48	3.284	2.862
11070	2.804	2.471	3.272	2.854
11160	2.796	2.462	3.26	2.846
11250	2.787	2.452	3.249	2.839
11340	2.779	2.443	3.237	2.831
11430	2.771	2.434	3.226	2.823
11520	2.763	2.426	3.215	2.816
11610	2.755	2.417	3.203	2.808
11700	2.747	2.409	3.192	2.801
11790	2.739	2.4	3.181	2.793
11880	2.731	2.392	3.17	2.786
11970	2.723	2.384	3.16	2.779
12060	2.715	2.376	3.149	2.771
12150	2.707	2.368	3.139	2.764
12240	2.699	2.36	3.128	2.757
12330	2.691	2.352	3.118	2.749
12420	2.683	2.345	3.108	2.742
12510	2.676	2.338	3.098	2.735
12600	2.668	2.33	3.088	2.728
12690	2.66	2.323	3.078	2.721
12780	2.652	2.316	3.068	2.714
12870	2.645	2.309	3.059	2.707
12960	2.637	2.303	3.049	2.7
13050	2.63	2.296	3.04	2.693
13140	2.622	2.29	3.031	2.686
13230	2.615	2.283	3.022	2.679
13320	2.607	2.277	3.013	2.673
13410	2.6	2.271	3.004	2.666
13500	2.593	2.265	2.996	2.659
13590	2.585	2.259	2.987	2.653
13680	2.578	2.253	2.979	2.646

Time(s)	StZnB	Zn3B	Zn4B	Zn5B
13770	2.571	2.248	2.971	2.64
13860	2.564	2.242	2.963	2.633
13950	2.557	2.237	2.955	2.627
14040	2.55	2.232	2.947	2.621
14130	2.543	2.226	2.94	2.614
14220	2.536	2.221	2.932	2.608
14310	2.529	2.216	2.925	2.602
14400	2.523	2.211	2.918	2.596
14490	2.516	2.207	2.911	2.59
14580	2.51	2.202	2.904	2.584
14670	2.503	2.197	2.898	2.578
14760	2.497	2.193	2.891	2.572
14850	2.49	2.188	2.885	2.566
14940	2.484	2.184	2.878	2.56
15030	2.478	2.179	2.872	2.554
15120	2.472	2.175	2.866	2.549
15210	2.466	2.171	2.86	2.543
15300	2.46	2.167	2.854	2.537
15390	2.454	2.162	2.848	2.532
15480	2.448	2.158	2.842	2.526
15570	2.442	2.154	2.837	2.521
15660	2.436	2.15	2.831	2.516
15750	2.431	2.146	2.825	2.51
15840	2.425	2.142	2.82	2.505
15930	2.42	2.138	2.814	2.5
16020	2.414	2.134	2.809	2.494
16110	2.409	2.13	2.804	2.489
16200	2.403	2.127	2.799	2.484
16290	2.398	2.123	2.793	2.479
16380	2.393	2.119	2.788	2.474
16470	2.388	2.115	2.783	2.469
16560	2.383	2.111	2.778	2.464
16650	2.378	2.108	2.773	2.46
16740	2.373	2.104	2.768	2.455

Time(s)	StZnB	Zn3B	Zn4B	Zn5B
16830	2.368	2.1	2.763	2.45
16920	2.363	2.096	2.758	2.445
17010	2.358	2.093	2.753	2.441
17100	2.353	2.089	2.748	2.436
17190	2.349	2.085	2.743	2.432
17280	2.344	2.081	2.738	2.427
17370	2.339	2.077	2.733	2.423
17460	2.335	2.074	2.728	2.418
17550	2.33	2.07	2.723	2.414
17640	2.326	2.066	2.718	2.41
17730	2.322	2.062	2.714	2.405
17820	2.317	2.058	2.709	2.401
17910	2.313	2.054	2.704	2.397
18000	2.309	2.05	2.699	2.393
18090	2.305	2.046	2.694	2.389
18180	2.301	2.043	2.689	2.385
18270	2.297	2.038	2.684	2.381
18360	2.293	2.034	2.679	2.377
18450	2.289	2.03	2.674	2.373
18540	2.285	2.026	2.669	2.369
18630	2.281	2.022	2.664	2.365
18720	2.277	2.018	2.658	2.361
18810	2.273	2.014	2.653	2.358
18900	2.27	2.01	2.648	2.354
18990	2.266	2.005	2.643	2.35
19080	2.262	2.001	2.637	2.347
19170	2.259	1.997	2.632	2.343
19260	2.255	1.993	2.627	2.34
19350	2.252	1.989	2.621	2.336
19440	2.248	1.984	2.616	2.333
19530	2.245	1.98	2.61	2.329
19620	2.241	1.976	2.605	2.326
19710	2.238	1.972	2.599	2.323
19800	2.235	1.967	2.593	2.319

Time(s)	StZnB	Zn3B	Zn4B	Zn5B
19890	2.232	1.963	2.588	2.316
19980	2.229	1.959	2.582	2.313
20070	2.225	1.955	2.577	2.31
20160	2.222	1.95	2.571	2.307
20250	2.219	1.946	2.565	2.304
20340	2.216	1.942	2.56	2.301
20430	2.213	1.938	2.554	2.298
20520	2.21	1.934	2.548	2.295
20610	2.207	1.93	2.543	2.292
20700	2.205	1.925	2.537	2.289
20790	2.202	1.921	2.532	2.286
20880	2.199	1.917	2.526	2.283
20970	2.196	1.913	2.52	2.281
21060	2.193	1.909	2.515	2.278
21150	2.191	1.905	2.509	2.275
21240	2.188	1.901	2.504	2.273
21330	2.185	1.897	2.498	2.27
21420	2.183	1.893	2.493	2.267
21510	2.18	1.889	2.488	2.265

Appendix B: The publication papers

Applied Science and Engineering Progress, Vol. 17, No. 3, 2024, 7410 1

Review Article

Research Progress and Future Expectations in Anode of Secondary Zinc-Air Batteries: A Review

Chen Shunhong and Saroj Pullteap*
Department of Mechanical Engineering, Faculty of Engineering and Industrial Technology, Silpakorn University (Sanam Chandra Palace Campus), Nakhon Pathom, Thailand

Tang Mao
School of Mechanical Engineering, Chengdu University, Sichuan, China

* Corresponding author. E-mail: saroj@su.ac.th
DOI: 10.14416/j.asep.2024.06.006
Received: 29 February 2024; Revised: 4 April 2024; Accepted: 11 April 2024; Published online: 21 June 2024

Abstract
Zinc-air batteries have attracted widespread attention due to their advantages, including high safety, high theoretical energy density (1086 W·h/kg), low cost, etc. A zinc-air battery primarily consists of a metal anode, electrolyte, and air cathode. However, the anode, as the core component of zinc-air batteries, faces various challenges at the present stage, such as dendritic growth, anode deformation, surface passivation, hydrogen evolution corrosion, etc. These challenges limit the development of secondary zinc-air batteries. To address the challenges faced by the anode, researchers are committed to developing anode materials with long cycle life and high capacity. However, this is achieved through methods like alloying, surface coating, 3D structures, surface modification, and the addition of additives. Therefore, this article provides a comprehensive review of recent breakthroughs and progress in the research on zinc-based battery anodes in recent years. Furthermore, it offers a certain outlook on the future development direction of secondary zinc-air batteries.

Keywords: Secondary zinc-air batteries, Zinc anode, Dendritic growth, Alloying, Coating, 3D structure

1 Introduction

Nowadays, the increasing demand for energy and the consumption of non-renewable fossil fuels put tremendous pressure on humans [1]. This forces our human beings to be concerned, and also turn to the development of clean energy, such as wind energy, solar energy, hydro energy, tidal energy, fuel cells, biomass power, etc. [2]–[5]. However, clean energy sources are often unstable, therefore, the development of energy storage systems (ESSs) will help balance the production and demand of intermittent energy. At this stage, there are energy storage systems such as battery energy storage, thermal energy storage, pumped hydro energy storage, and chemical energy storage. Battery energy storage systems have been widely used in recent years because of their high power and ease of use [6], [7]. The escalating demand for energy storage is driving advancements in battery technology [2], [8], [9]. However, lithium-ion battery is a type of battery that has good characteristics such as high voltage, high energy density, high coulomb efficiency, low self-discharge, cycling stability, etc. [8], [10], [11]. Focus on such result, lithium-ion batteries have becoming to be the most commercially viable energy storage solution in recent decades [12]. Unfortunately, the high costs and unsafety issues contribute to their lack of competitiveness in a part of secondary energy storage applications [13], [14]. To eliminate a such problem, a series of metal-air batteries such as Li-air batteries, Na-air batteries, K-air batteries, Zn-air batteries, Mg-air batteries, Al-air batteries, and Iron-air batteries [15]–[21] have emerged. However, the metal-air batteries utilize oxygen from the air as the cathode,

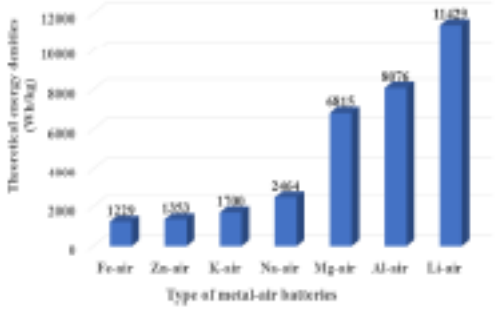

Figure 1: Theoretical energy densities of various types of metal-air batteries [23].

which not only reduces the weight of the battery but also enhances its energy density. This contributes largely to the improvement of battery energy density [22]. Among all of these batteries, the lithium-air battery has the highest theoretical energy density [23], as shown in Figure 1.

However, it also faces many challenges, for example, discharge by-products cause clogging of the cathode, resulting in incomplete discharge, etc. [15]. The charging over-point is much higher than the discharging over-point, resulting in low efficiency [24]. Thus, these issues make it difficult to apply. Comparably, the lower reduction potentials of magnesium and aluminium-air batteries result in severe self-discharge for both. Iron-air batteries have lower energy density (763 W·h/kg) and open circuit voltage (1.28 V). Such problems led to zinc-air batteries gaining widespread attention. Owing to their higher energy density (1086 W·h/kg) and high volumetric capacity (6163 W·h/L) [2].

As mentioned before, zinc-air batteries can be divided into two main types: primary zinc-air batteries and secondary zinc-air batteries, respectively [25]. After the commercialization of the first zinc-air battery in 1932, its influence rapidly expanded because of its high capacity. Currently, the primary zinc-air batteries are mainly used for powering hearing aids and cochlear implants [26]. In the late 20th century, it was, continuously, applied to electric Mercedes-Benz trucks [27] also the electric bus of Electric Fuel Ltd. [28], propelling the development of secondary zinc-air batteries to climax. Nevertheless, the flourishing trend of secondary zinc-air batteries was terminated by the emergence of lithium-ion batteries [29]. Until the 2010s, lithium-ion batteries faced limitations in capacity, expensive raw materials, and safety concerns. This created an opportunity for the development of secondary zinc-air batteries again. For secondary zinc-air batteries, the cathode material is unlimited atmospheric oxygen, therefore the actual energy density is normally related to the discharge capacity of the zinc anode [30]. However, there are many issues with the anode itself, i.e. dendrite growth, deformation, surface passivation, and hydrogen evolution. However, there are several researchers have conducted extensive studies on the aforementioned problems with the anode. By the way, Kadam *et al*. [31] use two anodes to improve the ability of anode. Dilshid et al. improve the anode through the adoption of a 3D structure [32]. Besides, Yuan *et al*. enhance the anode using the properties of alloying techniques [33]. Consequently, Mou *et al*. enhance the anode by employing surface coating [34]. All these methods did some improvement of the anode of zinc-air batteries.

In this work, the development of zinc-air batteries was first explored to highlight the importance of the development of the anode of the zinc-air batteries. Subsequently, through a summary of recent years' research, various methods for improving the energy density of zinc-air batteries by enhancing the anode are reviewed. The primary approaches for anode enhancement include alloying of the anode metal, addition of anode additives, improvement of the anode's 3D structure, and surface treatment and modification of the anode. Finally, viewpoints and suggestions regarding the future development of secondary zinc-air batteries are proposed. With the development of contemporary advanced technology and its application in the development of zinc air batteries, the development of high-capacity anode zinc air batteries is both necessary and possible. This will be an important part of the battery development history. Summarizing the development process of zinc-air batteries can further clarify the developmental direction of zinc-air batteries, aiding researchers in the expedited development of high-performance zinc-air batteries. At the same time, the cost of lithium-ion batteries is 3 times of zinc-air batteries. This means zinc-air batteries have high economic value for the application of battery energy storage technology.

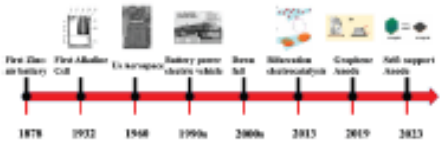

Figure 2: Development history of zinc-air batteries [35]–[39].

2 Brief History of Zinc-Air Battery

The development of zinc-air batteries is not like other batteries. It has undergone a prolonged period of development to date. The combination of metallic zinc and oxygen from the air to form a battery represents the arrival of the first milestone that belongs to the zinc-air battery era, as shown in Figure 2.

In 1878, the French engineer L. Maiche [40] disclosed a battery design featuring a porous air cathode, indicating the vast potential of zinc-air batteries and paving the way for the development of novel zinc-air batteries. In 1932, Heise and Schumacher [37] pioneered the first alkaline zinc-air battery using sodium hydroxide as the electrolyte, which weighed 116 kg and had an open-circuit voltage of 1.4–1.45V. The military demands of the 1960s became a significant driving force in the development of zinc-air batteries. Following the creation of magnesium-air (1960s) [38], lithium-air (1970s) [41], and aluminum-air (1970s) [42] batteries, the energy density of zinc-air batteries was elevated to 200Wh/kg in the 1980s [29]. Nonetheless, progress invariably experiences fluctuations. Starting in the late 1970s, with the introduction of the rocking chair concept for lithium batteries, the development of lithium-ion batteries faced certain constraints [43]. Particularly in the 1980s, the proposal of Li_xCoO_2 as a cathode material for lithium-ion batteries [44], incorporated with a theoretical energy density of up to 1100Wh/kg, greatly advanced the development of lithium-based energy storage technology. Electrode materials introduced in the late 1990s, such as $LiFePO_4$ [45] and $LiMn_2O_4$ [46], brought the energy density of lithium-based batteries to 300Wh/kg, far surpassing that of zinc-air batteries. Lithium-based energy storage technology gradually took the developmental lead during this period. Meanwhile, zinc-air batteries were primarily utilized in simple devices such as hearing aids and pagers [35].

Entering the 21st century, lithium-ion batteries have become the mainstay of development with diversified applications in everyday life. According to the International Energy Agency's data from 2020, lithium-ion batteries accounted for 93% of the new battery storage capacity added in that year, indicating their extensive development and application [29]. However, when the energy density of lithium-ion batteries reaches 400Wh/kg [47], they pose a risk of spontaneous combustion [48]. Furthermore, the high cost of lithium resources presents challenges for industrial production [49]. Additionally, the toxicity of the electrolyte leads to difficulties in subsequent processing [50]. This has led to a recognition of the need to develop an alternative to lithium-ion batteries. Zinc-air batteries have once again come to the forefront of development.

In 2013, Li *et al.* [36] achieved an increase in the energy density of zinc-air batteries to 700Wh/kg through the development of an innovative catalyst. A developed bifunctional oxygen electrocatalyst with a ΔE of approximately 0.63 V achieved 3,600 and 650 charge-discharge cycles at current densities of 10 mA/cm² and 50 mA/cm² respectively [51]. However, as the ability of ORR/OER catalysts continues to improve, a decline in battery performance has been observed. Given that the oxygen reactant for zinc-air batteries is sourced from the limitless atmosphere, the actual energy density is also related to the discharge capacity of the zinc anode [30]. The zinc anode faces complex challenges such as zinc stripping/deposition, dendrite growth, hydrogen evolution, and deformation. In 2019, Zheng *et al.* [39] developed a graphene-coated electrode, which showed superior performance through thousands of cycles with an epitaxial zinc anode. In 2023, Mou *et al.* [34] developed a highly ordered zinc anode array structure, achieving a capacity of 995.77 mAh for zinc-air batteries, with 1,200 effective cycles at a current density of 10 mA/cm². These developments have laid a solid foundation for the further advancement of zinc anodes.

From the aforementioned developmental history, we can observe that early zinc-air batteries had large volumes, low energy densities, and also low discharge efficiencies, etc. With the advancement of smart technology, the volume of zinc-air batteries is gradually decreasing, while their energy density, on the opposite ways, increased leading to increasingly widespread applications.

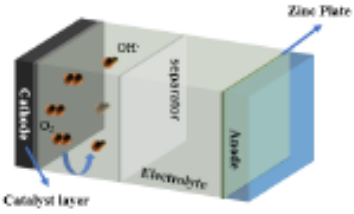

Figure 3: Schematic structural diagram of secondary zinc-air batteries.

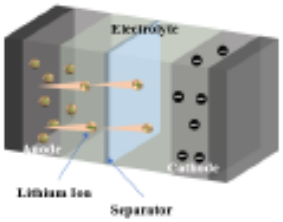

Figure 4: Schematic structural diagram of lithium-ion battery.

3 Structure of Rechargeable Zinc-Air Battery

The structure of a rechargeable zinc-air battery is illustrated in Figure 3 [52], which comprises primarily a zinc anode, an air cathode, an electrolyte, and also a separator. Moreover, the chemical reactions during the charge and discharge processes of the rechargeable zinc-air battery are as follows Equations (1)–(4):

Zinc Anode:

$$Zn + 4OH^- \rightleftarrows Zn(OH)_4^{2-} + 2e \quad (1)$$

$$Zn(OH)_4^{2-} \rightleftarrows ZnO + 2OH^- + H_2O \quad (2)$$

Air Cathode:

$$O_2 + H_2O + 4e \rightleftarrows 4OH^- \quad (3)$$

Overall Reaction:

$$2Zn + O_2 \rightleftarrows 2ZnO \quad (4)$$

From the above reaction equations, it can be observed that during discharge, zinc at the anode is initially oxidized to $Zn(OH)_4^{2-}$. Also, when $Zn(OH)_4^{2-}$ reaches a certain saturation concentration in the electrolyte, it further undergoes deposition to form ZnO. Meanwhile, oxygen at the cathode is reduced to generate OH– ions. During charging, $Zn(OH)_4^{2-}$ in the electrolyte is reduced back to zinc, redepositing on the surface of the zinc anode.

The structure of Lithium-ion batteries is shown in Figure 4 [53]. As shown in Figures 3 and 4, the huge difference between zinc-air batteries and lithium batteries is that the cathode of zinc-air batteries is derived from oxygen in the air. This means that there is a constant supply of the cathode of zinc-air batteries. This is also one of the reasons why zinc-air batteries have the great potential to replace lithium-ion batteries.

4 Challenges for Anode of Zinc-Air Batteries

Currently, the widely used anode material in large-scale applications of rechargeable zinc-air batteries is a paste-like substance made from zinc powder [54]. This type of anode material has the advantage of ensuring sufficient contact between the active material and the electrolyte. However, its rechargeability is lacking, which hinders its broad use in rechargeable zinc-air batteries. For the rechargeable zinc-air batteries, the theoretical voltage should be 1.6V, but the actual discharge voltage is generally below 1.2V, and the charging voltage needs to be above 2V. This directly results in the lower Coulombic efficiency of rechargeable zinc-air batteries. These issues are mainly caused by dendritic growth, deformation, surface passivation, and hydrogen evolution corrosion in rechargeable zinc-air batteries [54], as illustrated in Figure 5.

In ideal circumstances, the $Zn(OH)_4^{2-}$ on the surface of the anode should be uniformly distributed. However, in reality, due to various factors, $Zn(OH)_4^{2-}$ on the anode surface is rarely distributed uniformly. This uneven distribution leads to an uneven distribution of the deposited substances on the anode surface, forming a rough and uneven surface. Dendritic growth is inevitable because it is caused by the uneven distribution of ions near the zinc electrode, especially during repeated cycles, as given in detail in Figure 5(a) [34]. With repeated cycling, the extent of unevenness intensifies, ultimately causing continuous growth and

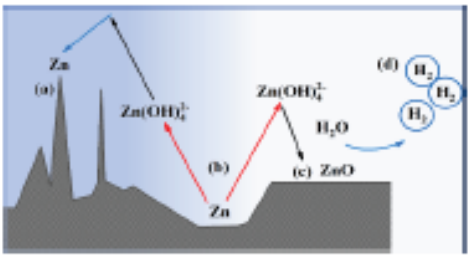

Figure 5: Possible phenomena in zinc anodes; (a) Dendrite growth; (b) Shape change; (c) Passivation; and (d) Hydrogen evolution.

extension of dendrites, resulting in dead zinc that cannot participate in the reaction. In extreme cases, large dendrites may pierce through the battery's separator, causing a short circuit and destroying the battery.

The deformation of the anode occurs because the zinc salt products obtained in reaction 1) are insufficient/ do not participate in a reaction 2), failing to form ZnO but instead depositing directly on the anode surface. After repeated charge and discharge cycles, a large amount of zinc salt accumulates leading to the deformation of the battery and a significant reduction in capacity, as shown in Figure 5(b). Besides the passivation of the anode surface is due to the formation of a dense layer of non-reactive ZnO during repeated charge and discharge cycles as displayed in Figure 5(c). By the way, this not only increases the internal resistance of the battery but also hinders direct contact between the anode and the electrolyte. With increased internal resistance, the battery requires a higher voltage during the charging process, while in the discharging process, it can only maintain a lower voltage. The lack of direct contact between the anode and the electrolyte leads to capacity decay in the battery. Furthermore, The hydrogen evolution reaction at the anode occurs in a battery during open-circuit conditions because the reduction potential of hydrogen is more positive than the reduction potential of zinc as addressed in Figure 5(d). Therefore, in the reaction process, a side reaction will take place first as shown in the calculation below:

$$Zn + H_2O \rightleftarrows Zn(OH)_2 + H_2 \quad (5)$$

Besides, this reaction results in the unnecessary consumption of zinc, reducing the battery capacity,

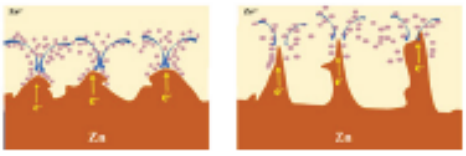

(a) (b)

Figure 6: Volume change and formation of dendrite of bare Zn [50].

while the generated $Zn(OH)_2$ also increases the internal resistance of the battery, further decreasing its capacity.

The four mentioned situations interact and correlate with each other during the reaction process. A large amount of active material at the zinc anode is consumed, leading to a significant disparity between the actual capacity and theoretical capacity of the zinc-air batteries.

5 Modification Methods for Anode of Zinc-Air Secondary Batteries

To achieve better performance for the anode of zinc-air secondary batteries, researchers have developed various methods to enhance the anode. These methods, based on the extent of their application, mainly include 1) Alloying of the anode 2) Surface coating and treatment of the anode 3) Addition of the anode additives properties and 4) 3D structuring of the anode, respectively.

5.1 *Alloying of anode*

For the zinc metal anode, the single zinc metal anode exhibits a significant number of cracks and defects due to the substantial volume changes during the de-zincing and zinc plating processes, as illustrated in Figure 6 [55]. For Figure 6(a), during the plating or stripping of zinc, Zinc ions exhibit a preference for nucleation at dislocated sites, leading to the development of initial protuberances on the surface of zinc. Figure 6(b) displays the protuberances have higher potentials and consist of high-density low-coordination steps. Both of these contribute to the growth of dendrites. Alloying zinc with other metals can greatly improve the performance of zinc-air batteries. For example, conductivity is one of the important indicators of zinc-air batteries. The selected metal should possess a higher overpotential of the

evolution of hydrogen compared to zinc, effectively mitigating the corrosion caused by hydrogen evolution on the zinc anode altering its shape, and increasing its utilization. Commonly used metals for alloying include lead (Pb), cadmium (Cd), indium (In), tin (Sn), aluminum (Al), bismuth (Bi), nickel (Ni), etc [56]. Research has displayed that incorporating metals with zinc not only enhances the conductivity of the zinc anode but also serves as a substrate for the deposition of zinc during charging deeds, effectively improving the coulombic efficiency of zinc-air batteries. Due to the simplicity of the alloying process and its favorable outcomes, this method has been widely applied in past research studies.

Recently, Ning *et al*. [57] identified through orthogonal experimental methods that an alloy with the composition Zn-0.1% In-0.1% Bi-0.01 Ca exhibited optimal performance as an anode. The maximum power density of the anode was 169.7 mW/cm^2, and it could maintain a stable constant current discharge of 0.93V at 100mA/cm^2 for over 200 min. The addition of alloying elements increased the resistance of the anode's corrosion reaction, suppressing intermediate products and reducing zinc corrosion, enhancing the anode's performance. Peng *et al*. [58] prepared an integrated, dense Zn-Sn alloy plate electrode using powder sintering technology. Further, this alloy electrode significantly improved the electrochemical performance of zinc-air batteries. Besides, the fabricated alloy-based battery maintained excellent dendrite-free zinc peeling and plating performance even after 400 h of cycling. Yuan *et al*. [33] proposed a method to alloy the zinc anode with rare earth metal Ce and alkaline earth metal Yb to alleviate dendrite growth. This was achieved by changing the anisotropic modulus and strength at the zinc anode interface. However, the results indicate that an uniaxial modulus of six could achieve a 35% suppression of anisotropic modulus. The most effective way to inhibit dendrite growth was to use zinc anodes composed of Zn98%-Mg2% or Zn93.5%-Yb6.5%, and the addition of Ce expand the anode interface's anisotropic modulus, changing the direction of dendrite growth and reducing its height, while the addition of the Yb reduced the anisotropic strength of the interface, hindering dendrite growth. According to the above three methods, the anode performance of zinc-air batteries can indeed be improved through alloying.

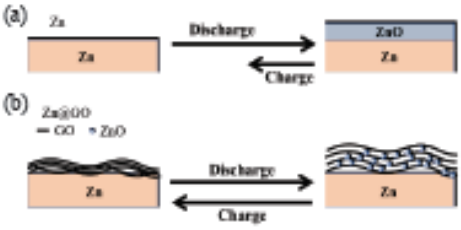

Figure 7: Schematic diagram of morphological changes of zinc anodes during electrochemical cycling [28].

5.2 *Surface coating and treatment of anode*

Surface coating of the anode can also play a significant role in improving the performance of the battery. Coating materials can isolate the electrolyte from the zinc anode, and confine $Zn(OH)_4$ ions within the anode, not only inhibiting hydrogen evolution corrosion and dendrite formation but also reducing the consumption of active material. The combination of these effects can enhance the battery's performance. Additionally, depending on the properties of the coating material, this can truly enhance conductivity, contributing to the improvement of the anode's performance. Common coating materials include Al_2O_3, TiO_2, SiO_2, $Ca(OH)_2$, carbon, etc. [59]–[62]. With further research, new types of coating materials are also being developed.

Zhou *et al*. [63] coated zinc mesh with graphene oxide, and after 200 cycles of testing, they found that the cumulative discharge capacity was about 128% of that of pure zinc. This is because graphene oxide can prevent zincate ions from passing through, while H_2O and OH- can pass through. During the decomposition of zincate into ZnO, graphene oxide wraps around it, reducing the loss of active material, as shown in Figure 7. Focusing on Figure 7(a), it express that the ZnO passivation layer leads to low utilization of the Zn mesh anode. In addition, graphene oxide on the Zn surface makes it possible for electrons to move freely across the insulating ZnO and slows down the dissolution of Zn species. This concept has been illustrated in Figure 7(b). In addition, Ismail *et al*. [64] proposed a novel technique by coating cassava starch onto the surface of the zinc anode and found that the conductivity increased by 30% compared to a pure zinc anode. This improved conductivity resulted in better performance of the zinc anode. Sun *et al*. [65]

coated ZnO nanorods uniformly dispersed on three-dimensional graphene oxide as a chemical buffer layer on the zinc metal (CBL@Zn) anode. Due to the synergistic effect of the crystallization of ZnO nanorods and the adsorption affinity of graphene oxide, the assembled battery achieved an unusually long cycling performance of 450 h. On the other hand, surface modification treatment of the anode can also improve the battery's capability to a certain extent. For example, Wang *et al*. [66] used laser irradiation on the surface of the zinc anode to remove the surface oxide layer, increasing the contact area of the anode and thereby inhibiting dendrite growth. Han *et al*. [67] decorated the surface of zinc with dual-functional indium metal, serving as both a corrosion inhibitor and a nucleating agent. This effectively prevented corrosion and dendrite growth, and the assembled battery maintained over 1500 hours of electroplating/stripping cycles. The above literature shows that both coating and surface treatment of anodes can increase the surface area or remove the oxide layer to improve anode performance.

5.3 *Anode additives*

When the anode in zinc-air batteries is pure zinc, the discharge product ZnO has a larger volume, 1.6 times that of pure Zn [68] This directly leads to severe electrode deformation during the cycling process. Additionally, because ZnO is a semiconductor, it can also lower the battery's performance. Adding additives to the anode can to some extent address these issues. Lee *et al*. [69] by using zinc and ZnO as or with the anode, found that the stability of the mixed anode was significantly improved compared to a pure zinc anode. This improvement was attributed to the smaller expansion coefficient, suppressing the deformation of the mixed anode. Stamm *et al*. [61] found that adding ZnO to the mixed anode, while reducing the initial discharge capacity, increased the rechargeable capacity and the cycle life of the zinc anode. This is because the added ZnO in pure zinc becomes a nucleating crystal, promoting the uniform deposition and dissolution of ZnO, thereby improving the capacity retention of zinc-air batteries. Park *et al*. [62] achieved a discharge capacity of 160 mAh/g by refining the size of added ZnO to the nanoscale. This makes the nano ZnO have a higher surface area, allowing for a faster reaction

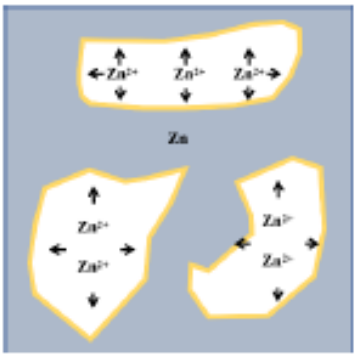

Figure 8: Employing a high surface area porous zinc structure [64].

with KOH solution, leading to quicker generation of zincate ions and thus enhancing battery performance.

If conductive agents, metal hydroxides, metal oxides, and other types of additives are introduced into the anode, the conductivity and cycling performance of the battery can be markedly improved. The addition of conductive agents such as graphite and carbon black facilitates rapid electron transfer between pure zinc and ZnO. This arises from these conductive additives enhancing the conductivity of the anode, slowing down the passivation of the anode, and improving battery performance. Masir *et al*. [60] by adding Super P carbon black to the zinc anode as an additive, achieved a 27% increase in the utilization of active materials compared to a pure zinc anode. However, this is attributed to Super P carbon black providing a pathway for electron transfer, allowing more active materials to participate in the cycling process. Both additives and conductive agents can enhance the cycling life of zinc-air batteries on one hand, while improving the performance of the negative electrode on the other hand.

5.4 *3D structure of anode*

Zinc materials with a 3D porous structure can not only increase the anode's specific surface area but also enhance the utilization of zinc, playing a beneficial role in promoting the complete reaction of zinc-air batteries. As shown in Figure 8 [70]. Moreover, the large surface area of a 3D porous structure allows for a uniform distribution of current across the entire

electrode during the effective reduction of zincate concentration. The porous structure also restricts the dissolution/precipitation process, effectively reducing dendrite growth in secondary zinc-air batteries [59], [64] thereby contributing to the improvement of the battery's performance.

Dilshad *et al.* [32] grew 3D zinc nanosheets with a high surface area on the surface of zinc through molecular modification. The assembled electrode with the modified material exhibited over 500 cycles of cycling performance under a condition of 5 mA/cm², with an operating time exceeding 83 h. This improvement is attributed to the increased contact area, promoting more complete reactions. Qu *et al.* [65] obtained a 3D structured zinc-coated foam anode by plating zinc on a copper foam substrate and assembled with a plated anode, PVA-TEAOH-KOH hydrogel, and carbon cloth, they created a flexible zinc-air battery that can bend at large angles without mechanical fracture. The fabricated battery achieved a high specific capacity of 566.7 mAh/g and completed 48 cycles, making significant contributions to the development of flexible zinc-air batteries. The 3D structure mainly improves anode performance by increasing the specific surface area. As mentioned, this manuscript summarises the main anode treatment methods and also their effects in Table 1.

Table 1: Different strategies and impacts of anode improvement

Modification to Zinc Anode	Effects	Details of Methods/Technology	Result	Ref
Alloys with Sn, Bi, Ce, Yb, Mg, Al, etc.	Improve battery performance, reduce dendrite growth height, and inhibit hydrogen evolution corrosion	Sn	0.5 mA/cm² current density for 400 h	[33]
		Zn-0.1% In-0.1% Bi-0.01% Ca	100 mA/cm² current density for 200 min	[57]
		Ce and Yb	35% inhibition efficiency of dendrite growth	[58]
Surface Coating with Garphen and Zno. The laser irradiates the anode surface.	Improve discharge capacity and achieve ultra-long cycle performance. Increase the anode contact area	Graphene oxide-modified	Improve its lifetime accumulated capacity by 28%	[63]
		Femtosecond Laser Processing Structural Surfaces	The first discharge time of zinc anodes with surface structures of zinc-air batteries is about 10 times that of without processing.	[66]
		Decorating the Zn surface with a dual-functional metallic indium (In) layer	2A/g current density for 5000 cycle times	[67]
		Chemical Buffer Layer of ZnO and grisphene oxide	Symmetric coin cells could realize over 100 cycles	[71]
		Cassava Starch Layer	Increment 30% of conductivity values from the original conductivity	[72]
Adding zinc oxide as an additive and refining the zinc oxide grain size Conductive agents, metal oxides, and hydroxides	Improve stability and battery capacity Enhance conductivity and improve battery performance	Carbon black as an additive	High specific discharge capacity (776 mAh/g)	[60]
		ZnO as an additive	Improve the rechargeable capacity	[61]
		The particle size of micronized ZnO was changed to nanosized ZnO	Nanosized ZnO showed a higher cycle capacity than microsized ZnO	[62]
Generate 3D nano-zinc flakes and three-dimensional structured Zn coatings	Increasing the contact area makes the reaction more complete, improving battery performance and cycle times. Successful development of flexible zinc-air batteries	Grow high-surface-area three-dimensional (3D) Zn nanoflakes on molecularly modified Zn surface	0.5 mA/cm² current density for 100 cycles	[32]
		Novel Cu foam substrate with uniform Ag nanoparticles deposited on the surface as a three-dimensional (3D) anode	High specific capacity of 676 mAh/g	[56]
		A three-dimensional (3D) fibrous structure with a highly active surface and conductive pathway	Significantly reduce the charge transfer resistance after 200 cycles	[64]
		Zn-coated foam anode with three-dimensional (3D) architecture	Specific capacity of 566.7 mAh/g	[65]

6 Conclusions

This article gives a summary of the ways to modify the anode of a zinc-air battery. First, it introduces the importance of energy storage systems (ESSs). Due to the unstable of clean energy, ESSs are important not only in the industry but still also in our daily lives. Then, from a business perspective, we conclude that a zinc-air battery is a good choice for building ESSs. However, from a technical point of view, zinc-air batteries truly meet some problems. Additionally, the researchers did find some solutions to solve those problems. They are also listed in this manuscript. In summary, one of the main reasons why zinc-air batteries cannot be commercialized at the current stage and face slow development is the poor reversibility of the zinc anode. This is mainly attributed to the dendritic growth, deformation, passivation, and also hydrogen evolution corrosion of the zinc anode. To address this issue, researchers have taken various measures such as 1) alloying of the anode; 2) surface coating and treatment of the anode; 3) anode additives; and 4) 3D structure of the anode. These measures can to some extent increase the conductivity of the electrode, improve the utilization of active materials, reduce self-corrosion of the anode, and promote the uniform distribution of electronic currents on the electrode surface. However, on the other hand, other issues in the commercialization of secondary zinc-air batteries need to be considered, such as the electrode design and preparation process. The electrode design and preparation process directly settles the electrode's specific surface area, density, porosity, 3D structure, etc., which greatly influences the electrode's ability. Furthermore, the anode materials affect the ability of zinc-air batteries at the same time. So it is necessary to explore new materials or composites with enhanced electrochemical capabilities, reduced dendrite growth, and resistance to self-corrosion. Finally, a complete understanding of the reaction pathway of zinc-air batteries is required. After completing an exhaustive process, understanding the anode's reaction scheme, reaction kinetics, transport phenomena, developing more accurate models to predict and optimize ability, can enhance research efficiency. This manuscript sums up those methods in Table 2.

Table 2: Existing and prospective methods to improve the performance of zinc-air batteries

Aspects	Methods
Anode	Alloying of the anode
	Surface coating and treatment
	Anode additives
	3D structure of the anode
Electrode	Electrode design and preparation
	Exploration of new materials
Reaction mechanism	Comprehensive understanding

Acknowledgments

This research has received funding and support from the Silpakorn University Research, Innovation, and Creative Fund.

Author Contributions

Writing original draft preparation, C.SH.; Writing review and editing, S.P. All authors have read and agreed to the published version of the manuscript.

Conflicts of Interest

The authors declare no conflict of interest.

References

[1] L. Liu, Z. Wang, H. Zhang, and Y. Xue, "Solar energy development in China-A review," *Renewable and Sustainable Energy Reviews*, vol. 14, no. 1, 301–311, Jan. 2010.

[2] Y. Huang, Y. Wang, C. Tang, J. Wang, Q. Zhang, Y. Wang, and J. Zhang, "Atomic Modulation and structure design of carbons for bifunctional electrocatalysis in metal-air batteries," *Advanced Materials*, vol. 31, no. 13, 2019, Art. no. 1803800.

[3] P. Sapkota and H. Kim, "Zinc-air fuel cell, a potential candidate for alternative energy," *Journal of Industrial and Engineering Chemistry*, vol. 15, no. 4, 445–450, Jul. 2009.

[4] F. M. Guangul and G. T. Chala, "A comparative study between the seven types of fuel cells," *Applied Science and Engineering Progress*, vol. 13, no. 3, pp. 185–194, Apr. 2020, doi: 10.14416/j.asep.2020.04.007.

[5] A. Martsri, N. Yodpijit, M. Jongprasithporn, and

S. Junsupasan, "Energy, economic, and environmental (3E) analysis for sustainable development: A case study of a 9.9 MW biomass power plant in Thailand," *Applied Science and Engineering Progress*, vol. 14, no. 3, pp. 378–386, 2020, doi: 10.14416/j.asep.2020.07.002.

[6] J. Mitali, S. Dhinakaran, and A. A. Mohamad, "Energy storage systems: A review," *Energy Storage and Saving*, vol. 1, no. 3, pp. 166–216, Sep. 2022, doi: 10.1016/j.enss.2022.07.002.

[7] A. Z. A. Shaqsi, K. Sopian, and A. Al-Hinai, "Review of energy storage services, applications, limitations, and benefits," *Energy Reports*, vol. 6, pp. 288–306, Dec. 2020, doi: 10.1016/j.egyr.2020.07.028.

[8] X. Min, G. Xu, B. Xie, P. Guan, M. Sun, and G. Cui, "Challenges of prelithiation strategies for next generation high energy lithium-ion batteries," *Energy Storage Materials*, vol. 47, pp. 297–318, May 2022, doi: 10.1016/j.ensm.2022. 02.005.

[9] S. Agnew and P. Dargusch, "Effect of residential solar and storage on centralized electricity supply systems," *Nature Clim Change*, vol. 5, no. 4, pp. 315–318, Apr. 2015, doi: 10.1038/nclimate2523.

[10] T. Kim, W. Song, D.-Y. Son, L. K. Ono, and Y. Qi, "Lithium-ion batteries: outlook on present, future, and hybridized technologies," *Journal of Materials Chemistry A*, vol. 7, no. 7, pp. 2942–2964, Feb. 2019, doi: 10.1039/C8TA10513H.

[11] M. Armand and J.-M. Tarascon, "Building better batteries," *Nature*, vol. 451, pp. 652–657, Feb. 2008, doi: 10.1038/451652a.

[12] F. Zhao, J. Xue, W. Shao, H. Yu, W. Huang, and J. Xiao, "Toward high-sulfur-content, high-performance lithium-sulfur batteries: Review of materials and technologies," *Journal of Energy Chemistry*, vol. 80, pp. 625–657, May 2023, doi: 10.1016/j.jechem.2023.02.009.

[13] V. Soundharrajan, B. Sambandam, S. Kim, V. Mathew, J. Jo, S. Kim, J. Lee, S. Islam, K. Kim, Y.-K. Sun, and J. Kim, "Aqueous magnesium zinc hybrid battery: An advanced high-voltage and high-energy $MgMn_2O_4$ cathode," *ACS Energy Letters*, vol. 3, no. 8, pp. 1998–2004, Aug. 2018, doi: 10.1021/acsenergylett.8b01105.

[14] G. Fang, C. Zhu, M. Chen, J. Zhou, B. Tang, X. Cao, X. Zheng, A. Pan, and S. Liang, "Suppressing manganese dissolution in potassium manganate with rich oxygen defects engaged high-energy-density and durable aqueous zinc-ion battery," *Advanced Functional Materials*, vol. 29, no. 15, Apr. 2019, Art. no. 1808375, doi: 10.1002/adfm.201808375.

[15] A. Kraytsberg and Y. Ein-Eli, "Review on Li-air batteries-opportunities, limitations, and perspective," *Journal of Power Sources*, vol. 196, no. 3, pp. 886–893, Feb. 2011, doi: 10.1016/j.jpowsour.2010.09.031.

[16] Z. Khan, M. Vagin, and X. Crispin, "Can hybrid Na–air batteries outperform nonaqueous Na-O_2 batteries?," *Advanced Science*, vol. 7, no. 5, 2020, Art. no. 1902866, doi: 10.1002/advs.201902866.

[17] L. Qin, N. Xiao, S. Zhang, X. Chen, and Y. Wu, "From K-O2 to K-Air batteries: Realizing superoxide batteries on the basis of dry ambient air," *Angewandte Chemie International Edition*, vol. 59, no. 26, pp. 10498–10501, 2020, doi: 10.1002/anie.202003481.

[18] P. Chen, K. Zhang, D. Tang, W. Liu, F. Meng, Q. Huang, and J. Liu, "Recent progress in electrolytes for Zn–Air batteries," *Frontiers in Chemistry*, vol. 8, p. 372, 2020, doi: 10.3389/fchem.2020.00372.

[19] P. Jiang, D. Li, R. Hou, H. Yang, J. Yang, S. Zhu, L. Wang, and S. Guan, "A micro-alloyed Mg-Zn-Ge alloy as promising anode for primary Mg-air batteries," *Journal of Magnesium and Alloys*, 2023, doi: 10.1016/j.jma.2023.05.004.

[20] M. Wei, K. Wang, Y. Zuo, J. Liu, P. Zhang, P. Pei, S. Zhao, Y. Li, and J. Chen, "A high-performance Al-air fuel cell using a mesh-encapsulated anode via Al–Zn energy transfer," *iScience*, vol. 24, no. 11, 2021, doi: 10.1016/j.isci.2021.103259.

[21] B. Qian, Y. Zhang, X. Hou, D. Bu, K. Zhang, Y. Lan, Y. Li, S. Li, T. Ma, and X.-M. Song, "A dual photoelectrode photoassisted Fe–Air battery: The photo-electrocatalysis mechanism accounting for the improved oxygen evolution reaction and oxygen reduction reaction of air electrodes," *Small*, vol. 18, no. 7, 2022, Art. no. 2103933, doi: 10.1002/smll.202103933.

[22] Md. A. Rahman, X. Wang, and C. Wen, "High energy density metal-air batteries: A review," *Journal of The Electrochemical Society*, vol. 160, no. 10, pp. A1759–A1771,

2013, doi: 10.1149/2.062310jes.
[23] D. Ahuja, V. Kalpna, and P. K. Varshney, "Metal air battery: A sustainable and low-cost material for energy storage," *Journal of Physics: Conference Series*, vol. 1913, no. 1, May 2021, Art. no. 012065, doi: 10.1088/1742-6596/1913/1/012065.
[24] T. Zhang, N. Imanishi, Y. Shimonishi, A. Hirano, Y. Takeda, O. Yamamoto, and N. Sammes, "A novel high energy density rechargeable lithium/air battery," *Chemical Communications*, vol. 46, no. 10, pp. 1661–1663, 2010, doi: 10.1039/B920012F.
[25] V. Caramia and B. Bozzini, "Materials science aspects of zinc-air batteries: A review," *Materials for Renewable and Sustainable Energy*, vol. 3, no. 2, p. 28, Apr. 2014, doi: 10.1007/s40243-014-0028-3.
[26] X. U. Neng-neng and Q. I. A. O. Jin-li, "Recent Progress in bifunctional catalysts for zinc-air," *Journal of Electrochemistry*, vol. 26, no. 4, pp. 531–562, 2020.
[27] J. R. Goldstein and B. Koretz, "Tests of a full-sized mechanically rechargeable zinc-air battery in an electric vehicle," *IEEE Aerospace and Electronic Systems Magazine*, vol. 8, no. 11, pp. 34–38, Nov. 1993, doi: 10.1109/62.242061.
[28] J. Goldstein, I. Brown, and B. Koretz, "New developments in the Electric Fuel Ltd. zinc/air system," *Journal of Power Sources*, vol. 80, no. 1, pp. 171–179, Jul. 1999, doi: 10.1016/S0378-7753(98)00260-2.
[29] J.-N. Liu, C.-X. Zhao, J. Wang, D. Ren, B.-Q. Li, and Q. Zhang, "A brief history of zinc–air batteries: 140 years of epic adventures," *Energy & Environmental Science*, vol. 15, no. 11, pp. 4542–4553, 2022, doi: 10.1039/D2EE02440C.
[30] P. Pei, K. Wang, and Z. Ma, "Technologies for extending zinc–air battery's cyclelife: A review," *Applied Energy*, vol. 128, pp. 315–324, Sep. 2014, doi: 10.1016/j.apenergy.2014.04.095.
[31] N. Kadam and A. Sarkar, "A high voltage zinc–air battery with two isolated electrolytes and moving auxiliary electrodes," *Applied Energy*, vol. 344, Aug. 2023, Art. no. 121309, doi: 10.1016/j.apenergy.2023.121309.
[32] K. A. J. Dilshad and M. K. Rabinal, "Rationally designed Zn-Anode and Co_3O_4-Cathode nanoelectrocatalysts for an efficient Zn-Air battery," *Energy and Fuels*, vol. 35, no. 15, pp. 12588–12598, 2021, doi: 10.1021/acs.energyfuels.1c01108.
[33] X. Yuan, C. He, J. Wang, X. You, Y. Chen, Q. Gou, N. Yang, G. Xie, Y. Hou, "Inhibition of zinc dendrite growth in zinc-air batteries by alloying the anode with Ce and Yb," *Journal of Alloys and Compounds*, vol. 970, 2024, doi: 10.1016/j.jallcom.2023.172523.
[34] C. Mou, Y. Bai, C. Zhao, G. Wang, Y. Ren, Y. Liu, X. Wu, H. Wang, Y. Sun, "Construction of a self-supported dendrite-free zinc anode for high-performance zinc-air batteries," *Inorganic Chemistry Frontiers*, vol. 10, no. 10, pp. 3082–3090, 2023, doi: 10.1039/d3qi00279a.
[35] C. Sparkes and N. K. Lacey, "A study of mercuric oxide and zinc-air battery life in hearing aids," *The Journal of Laryngology & Otology*, vol. 111, no. 9, pp. 814–819, Sep. 1997, doi: 10.1017/S002221510013871X.
[36] Y. Li, M. Gong, Y. Liang, J. Feng, J.-E. Kim, H. Wang, G. Hong, B. Zhang, and H. Dai, "Advanced zinc-air batteries based on high-performance hybrid electrocatalysts," *Nature Communications*, vol. 4, no. 1, May 2013, Art. no. 1805, doi: 10.1038/ncomms2812.
[37] G. W. Heise and E. A. Schumacher, "An air-depolarized primary cell with caustic alkali electrolyte," *Transactions of The Electrochemical Society*, vol. 62, no. 1, p. 383, Jan. 1932, doi: 10.1149/1.3493794.
[38] R. P. Hamlen, E. C. Jenbek, J. C. Ruzzo, and E. G. Siwek, "Anodes for refuelable magnesium-air batteries," *Journal of the Electrochemical Society*, vol. 116, no. 11, p. 1588, Nov. 1969, doi: 10.1149/1.2411622.
[39] J. Zheng, Q. Zhao, T. Tang, J. Yin, C. D. Quilty, G. D. Renderos, X. Liu, Y. Deng, L. Wang, D. C. Bock, C. Jaye, D. Zhang, E. S. Takeuchi, K. J. Takeuchi, A. C. Marschilok, and L. A. Archer, "Reversible epitaxial electrodeposition of metals in battery anodes," *Science*, vol. 366, no. 6465, pp. 645–648, Nov. 2019, doi: 10.1126/science.aax6873.
[40] L. Maiche, French Patent 127069, 1878.
[41] J. Kolesar and S. Edward, "Thermoelectric cooling: Review and application. Aeromedical

review," Defense Technical Information Center, Fort Belvoir, VA, 1981.
[42] G. D. Brabson, J. Fannin, L. A. King, and D. W. Seegmiller, "Prototype high-power density aluminum-chlorine battery," in *Electrochemical Society*, May 1973, vol. 120, no. 3, Art. no. 7029560.
[43] B. Scrosati, "Lithium rocking chair batteries: An old concept?," *Journal of The Electrochemical Society*, vol. 139, no. 10, Oct. 1992, Art. no. 2776, doi: 10.1149/1.2068978.
[44] K. Mizushima, P. C. Jones, P. J. Wiseman, and J. B. Goodenough, "Li_xCoO_2 ($0 < x < -1$): A new cathode material for batteries of high energy density," *Materials Research Bulletin*, vol. 15, no. 6, pp. 783–789, Jun. 1980, doi: 10.1016/ 0025-5408(80)90012-4.
[45] A. K. Padhi, K. S. Nanjundaswamy, and J. B. Goodenough, "Phospho-olivines as positive-electrode materials for rechargeable lithium batteries," *Journal of The Electrochemical Society*, vol. 144, no. 4, Apr. 1997, Art. no. 1188, doi: 10.1149/1.1837571.
[46] M. M. Thackeray, "Manganese oxides for lithium batteries," *Progress in Solid State Chemistry*, vol. 25, no. 1, pp. 1–71, Jan. 1997, doi: 10.1016/ S0079-6786(97)81003-5.
[47] M. Armand, P. Axmann, D. Bresser, M. Copley, K. Edström, C. Ekberg, D. Guyomard, B. Lestriez, P. Novák, M. Petranikova, W. Porcher, S. Trabesinger, M. Wohlfahrt-Mehrens, and H. Zhang, "Lithium-ion batteries – Current state of the art and anticipated developments," *Journal of Power Sources*, vol. 479, Dec. 2020, Art. no. 228708, doi: 10.1016/j.jpowsour.2020.228708.
[48] J. Duan, J. Zhao, X. Li, S. Panchal, J. Yuan, R. Fraser, and M. Fowler, "Modeling and analysis of heat dissipation for liquid cooling lithium-ion batteries," *Energies*, vol. 14, no. 14, Jul. 2021, Art. no. 4187, doi: 10.3390/en14144187.
[49] H. Tian, P. Qin, K. Li, and Z. Zhao, "A review of the state of health for lithium-ion batteries: Research status and suggestions," *Journal of Cleaner Production*, vol. 261, Jul. 2020, Art. no. 120813, doi: 10.1016/j.jclepro.2020.120813.
[50] M. S. H. Lipu, M. A. Hannan, A. Hussain, A. Ayob, M. H. M. Saad, T. F. Karim, and D. N. T. How, "Data-driven state of charge estimation of lithium-ion batteries: Algorithms, implementation factors, limitations and future trends," *Journal of Cleaner Production*, vol. 277, Dec. 2020, Art. no. 124110, doi: 10.1016/ j.jclepro.2020.124110.
[51] C.-X. Zhao, J.-N. Liu, J. Wang, D. Ren, J. Yu, X. Chen, B.-Q. Li, and Q. Zhang, "A $\Delta E = 0.63$ V bifunctional oxygen electrocatalyst enables high-rate and long-cycling zinc–air batteries," *Advanced Materials*, vol. 33, no. 15, 2021, Art. no. 2008606, doi: 10.1002/adma.202008606.
[52] X. Chen, Z. Zhou, H. E. Karahan, Q. Shao, L. Wei, and Y. Chen, "Recent advances in materials and design of electrochemically rechargeable zinc–air batteries," *Small*, vol. 14, no. 44, 2018, Art. no. 1801929, doi: 10.1002/smll. 201801929.
[53] J. B. Goodenough and K.-S. Park, "The Li-Ion rechargeable battery: A perspective," *Journal of the American Chemical Society*, vol. 135, no. 4, pp. 1167–1176, Jan. 2013, doi: 10.1021/ ja3091438.
[54] J. Pan, Y. Y. Xu, H. Yang, Z. Dong, H. Liu, and B. Y. Xia, "Advanced architectures and relatives of air electrodes in Zn–Air batteries," *Advanced Science*, vol. 5, no. 4, 2018, Art. no. 1700691, doi: 10.1002/advs.201700691.
[55] S.-B. Wang, Q. Ran, R.-Q. Yao, H. Shi, Z. Wen, M. Zhao, X.-Y. Lang, and Q. Jiang, "Lamella-nanostructured eutectic zinc–aluminum alloys as reversible and dendrite-free anodes for aqueous rechargeable batteries," *Nature Communications*, vol. 11, no. 1, Apr. 2020, Art. no. 1634, doi: 10.1038/s41467-020-15478-4.
[56] Y. Li and H. Dai, "Recent advances in zinc–air batteries," *Chemical Society Reviews*, vol. 43, no. 15, pp. 5257–5275, 2014, doi: 10.1039/C4CS000 15C.
[57] Q. Ning, L. He, X. Wang, H. Liu, and S. Gao, "Effects of alloying elements on electrochemical performance of zinc-air battery anode," *Journal of Central South University (Science and Technology)*, vol. 52, no. 10, pp. 3389–3396, 2021, doi: 10.11817/j.issn.1672-7207.2021.10.002.
[58] Y. Peng, C. Lai, M. Zhang, X. Liu, Y. Yin, Y. Li, and Z. Wu, "Zn–Sn alloy anode with repressible dendrite grown and meliorative corrosion resistance for Zn-air battery," *Journal of Power Sources*, vol. 526, 2022, Art. no. 231173, doi: 10.1016/j.jpowsour.2022.231173.

[59] J. Yu, F. Chen, Q. Tang, T. T. Gebremariam, J. Wang, X. Gong, and X. Wang, "Ag-modified Cu foams as three-dimensional anodes for rechargeable zinc-air batteries," *ACS Applied Nano Materials*, vol. 2, no. 5, pp. 2679–2688, 2019, doi: 10.1021/acsanm.9b00156.

[60] M. N. Masri and A. A. Mohamad, "Effect of adding carbon black to a porous zinc anode in a zinc-air battery," *Journal of the Electrochemical Society*, vol. 160, no. 4, pp. A715–A721, 2013, doi: 10.1149/2.007306jes.

[61] J. Stamm, A. Varzi, A. Latz, and B. Horstmann, "Modeling nucleation and growth of zinc oxide during discharge of primary zinc-air batteries," *Journal of Power Sources*, vol. 360, pp. 136–149, 2017, doi: 10.1016/j.jpowsour.2017.05.073.

[62] D. J. Park, W. G. Yang, H. W. Jeong, and K. S. Ryu, "Study of zinc compounds for improving the reversibility of the zinc anode in zinc–air secondary batteries," *Bulletin of the Korean Chemical Society*, vol. 38, no. 7, pp. 706–710, 2017, doi: 10.1002/bkcs.11157.

[63] Z. Zhou, Y. Zhang, P. Chen, Y. Wu, H. Yang, H. Ding, Y. Zhang, Z. Wang, X. Du, and N. Liu, "Graphene oxide-modified zinc anode for rechargeable aqueous batteries," *Chemical Engineering Science*, vol. 194, pp. 142–147, 2019, doi: 10.1016/j.ces. 2018.06.048.

[64] R. Khezri, K. Jirasattayaporn, A. Abbasi, T. Maiyalagan, A. Mohamad, and S. Kheawhom, "Three-dimensional fibrous iron as anode current collector for rechargeable zinc-air batteries," *Energies*, vol. 13, no. 6, Mar. 2020, Art. no. 1429, doi: 10.3390/en13061429.

[65] S. Qu, B. Liu, X. Fan, X. Liu, J. Liu, J. Ding, X. Han, Y. Deng, W. Hu, and C. Zhong, "3D foam anode and hydrogel electrolyte for high-performance and stable flexible zinc–air battery," *ChemistrySelect*, vol. 5, no. 27, pp. 8305–8310, 2020, doi: 10.1002/ slct.202002573.

[66] C. Wang, Y. Yuan, J. Chen, D. Li, J. Wu, and K. Zhang, "Femtosecond laser processing structural surfaces of zinc anodes for rechargeable zinc-air battery," in *E3S Web of Conferences*, 2021, vol. 261, Art. no. 02078, doi: 10.1051/e3sconf/202126102078.

[67] D. Han, S. Wu, S. Zhang, Y. Deng, C. Cui, L. Zhang, Y. Long, H. Li, Y. Tao, Z. Weng, Q.-H. Yang, and F. Kang, "A corrosion-resistant and dendrite-free zinc metal anode in aqueous systems," *Small*, vol. 16, no. 29, Jul. 2020, Art. no. e2001736, doi: 10.1002/smll.202001736.

[68] T. Arlt, D. Schröder, U. Krewer, and I. Manke, "In operando monitoring of the state of charge and species distribution in zinc air batteries using X-ray tomography and model-based simulations," *Physical Chemistry Chemical Physics*, vol. 16, no. 40, pp. 22273–22280, 2014, doi: 10.1039/C4CP02878C.

[69] C. W. Lee, S. W. Eom, K. Sathiyanarayanan, and M. S. Yun, "Preliminary comparative studies of zinc and zinc oxide electrodes on corrosion reaction and reversible reaction for zinc/air fuel cells," *Electrochimica Acta*, vol. 52, no. 4, pp. 1588–1591, Dec. 2006, doi: 10.1016/j.electacta.2006.02.063.

[70] J. Fu, R. Liang, G. Liu, A. Yu, Z. Bai, L. Yang, and Z. Chen, "Recent progress in electrically rechargeable zinc–air batteries," *Advanced Materials*, vol. 31, no. 31, doi: 10.1002/adma.201805230, Art. no. 1805230, 2019.

[71] W. Sun, M. Ma, M. Zhu, K. Xu, T. Xu, Y. Zhu, and Y. Qian, "Chemical buffer layer enabled highly reversible Zn anode for deeply discharging and long-life Zn–air battery," *Small*, vol. 18, no. 9, 2022, doi: 10.1002/ smll.202106604.

[72] W. M. I. W. Ismail, M. N. Masri, and H. K. Adli, "Study of cassava starch layer on zinc anode by electrochemistry method for zinc-air fuel cell system," in *IOP Conference Series: Earth and Environmental Science*, 2020, vol. 596, Art. no. 012004, doi: 10.1088/1755-1315/596/1/012004.

Journal of Applied Science and Engineering, Vol. 29, No 5, Page 1239-1247 1239

Electrodeposited Zinc Anodes On Nickel Foam For Enhanced Zinc-Air Battery Performance

Chen Shunhong, Teerasak Hudakorn, and Saroj Pullteap*

Department of Mechanical Engineering, Faculty of Engineering and Industrial Technology, Silpakorn University, Nakhon Pathom, Thailand

** Corresponding author. E-mail: saroj@su.ac.th*

Received: Aug. 10, 2025; Accepted: Oct. 1, 2025

The uneven deposition of zinc on the electrode surface leads to inadequate durability and stability of zinc-air batteries, hindering their widespread application. This study systematically investigates the fabrication of zinc anodes by electrochemical deposition onto nickel foam substrates and evaluates their performance in zinc-air batteries. Zinc was deposited for varying durations ($3-5$ hours), and the resulting electrodes were characterized using Scanning Electron Microscopy coupled with Energy-Dispersive X-ray Spectroscopy (SEMEDS), X-ray Diffraction (XRD), X-ray Photoelectron Spectroscopy (XPS) and Transmission Electron Microscopy (TEM). Electrochemical measurements show that the sample deposited for 4 hours delivers the best overall performance, with an average discharge voltage of 1.17 V and a load current of 3.52 mA which is 21% higher than cells with pure- Zn anodes. Microstructural analysis further confirms that 4 hours affords the optimal balance between zinc loading (84.01wt%) and deposition uniformity. This study delineates the structureperformance correlation among electrodeposition time, zinc loading, microstructural features, and electrochemical behavior, offering vital theoretical guidance and process reference for the optimized fabrication of metal-air battery anodes.

Keywords: Zinc anode; electrochemical deposition; nickel foam; zinc-air battery

http://dx.doi.org/10.6180/jase.202605_29(5).0019

1. Introduction

With the continuous growth of global energy demand and the escalating severity of environmental issues, the massive consumption of fossil fuels has led to serious greenhouse effects and environmental pollution, making the development of clean energy a key pathway to address these problems [1–3]. However, the inherent intermittency and unpredictability of clean renewable energies such as solar and wind power severely hinder their large-scale application; therefore, the development of efficient and reliable energy storage systems is urgently needed [4, 5]. Among various energy storage technologies, lithium-ion batteries dominate the market, yet their energy density is limited (< 350 Wh kg^{-1}), the cost remains relatively high (about 150USD kW h^{-1}), and potential safety risks have not been fundamentally resolved [6–10]. In contrast, zinc-based batteries are regarded as highly promising nextgeneration energy storage technologies due to their high theoretical energy density, low cost, and intrinsic safety [11–13].

As the anode material in the first voltaic cell invented by Alessandro Volta, zinc has shown great potential in the history of secondary battery development and continues to attract research attention [14–16]. Zinc is abundant and environmentally friendly, possesses a high theoretical capacity (820mAh g^{-1}), and exhibits a relatively low hydrogen evolution overpotential in aqueous electrolytes, making it an ideal choice for constructing safe and low-cost energy storage systems [17–21]. In commercial applications, zinc has been successfully used in alkaline nickel-zinc batter-

ies to replace precious metal hydrides, or combined with air cathodes to achieve practical specific energies up to 400 Wh kg^{-1} [13, 22–26]. However, current zincbased batteries, such as alkaline zinc-nickel and zinc-manganese cells, require high areal capacity and deep discharge depth (DoD) to compete with lithium-ion batteries. Due to limited electrolyte volume, these batteries struggle to maintain long-term stable operation [13, 27]. Among zinc-based batteries, zinc-air batteries have garnered particular attention for their unique performance advantages and ultra-high theoretical energy density (1,353 Wh kg^{-1}, excluding oxygen mass). Despite their high theoretical energy density, the practical energy density and cycle life of zinc-air batteries remain limited. This is mainly owing to dendrite growth and morphological deformation of the zinc anode, as well as performance degradation of the air cathode [7]. Failure of the air electrode is closely related to the loss of active area, electrode flooding, catalyst deactivation, and pore blockage [28]. Therefore, developing highperformance zinc anodes (e.g., suppressing dendrite growth and improving electrochemical reversibility) is one of the core challenges to promote the commercial application of zinc-air batteries [29–32].

This study focuses on optimization strategies for zinc-air battery anodes by electrochemically depositing zinc onto nickel foam substrates, aiming to enlarge the anode reaction area and optimize the microstructure, thereby significantly enhancing the overall performance of the zinc-air battery. We employed advanced techniques, including X-ray diffraction (XRD), scanning electron microscopy (SEM), transmission electron microscopy (TEM), X-ray photoelectron spectroscopy (XPS), and electrochemical impedance spectroscopy (EIS), to systematically evaluate the effects of the electrochemical deposition process and its impact on battery performance. This work provides important experimental data and theoretical guidance for the design and fabrication of efficient and stable metal-air battery anode materials.

2. Materials and methods

2.1. Materials

All commercially available reagents were of analytical grade and used as received without further purification. Deionized water (resistivity $>$ 18.2M$\Omega \cdot$ cm) was used throughout the experiments. Commercial nickel foam (thickness 1.5 mm , pore density 100 PPI , Kunshan Xingzhenghong Battery Materials Co., Ltd.) was used as the substrate. All experiments were conducted at room temperature.

2.2. Pretreatment of Nickel Foam Substrate

Commercial nickel foam was cut to the required size (35 $\times$ 60 mm) and subjected to the following surface treatment steps: First, the samples were immersed in a mixed solution of hydrochloric acid (35wt%) and deionized water at a volume ratio of 1 : 2 and ultrasonically cleaned for 15 min to remove surface oxides and impurities. Subsequently, the samples were rinsed sequentially in three deionized water baths (5 min for each) to remove residual acid and ultrasonically in anhydrous ethanol (99.8% purity) for 15 minutes to remove organic contaminants. Finally, the pretreated substrates were dried in an oven at 60°C for 12 hours and the mass change was recorded using a precision balance.

2.3. Electrochemical Deposition of Zinc Anode

A CS350 electrochemical workstation (Wuhan Corrtest Instrument Co., Ltd) was used to electrodeposit zinc particles onto the three-dimensional porous nickel foam substrate via chronopotentiometry (CP). An aqueous solution of 0.5 mol L^{-1} zinc sulfate heptahydrate ($ZnSO_4 \cdot 7H_2O$, analytical grade, purity $\geq$ 98.5%) served as the electrolyte in a two-electrode configuration: nickel foam as the working electrode and pure zinc as the counter electrode. Electrodeposition was carried out at a constant current density of 0.11 A cm^{-2} using the electrochemical workstation.

To maintain uniform ionic concentration in the electrolyte and effectively remove bubbles generated at the electrode interface, magnetic stirring at 60 rpm was applied throughout the experiment. Deposition times were set to 3 hours, 4 hours, and 5 hours, with the corresponding samples designated as Zn3, Zn4, and Zn5 , respectively. Six parallel samples were prepared for each condition to ensure statistical reliability of the data. After electrodeposition, the samples were rinsed with deionized water and then dried at 60°C for 12 hours in a vacuum oven to obtain composite electrodes with uniform zinc coatings. The deposition efficiency was calculated gravimetrically, and the results showed an average efficiency of 89 $\pm$ 3%.

2.4. Assembly of Zinc-Air Batteries

The Zn3, Zn4, Zn5 were used as the anodes, and a high-surface area carbon plate (10 $\times$ 60 mm, 99% purity) loaded with platinum catalyst was used as the air cathodes. KOH aqueous solution (A 6 mol L^{-1}) served as the electrolyte, and a glass fiber filter (GF/C, 47 mm diameter) which is prewetted with electrolyte was employed as the separator. The cell housing consisted of three custom acrylic plates (60 $\times$ 70 $\times$ 15 mm) with 0.5 mm -thick silicone gaskets to ensure good sealing. The assembled batteries were designated

consequently, the energy storage capacity of the electrode. This loading level suggests optimal utilization of the three-dimensional nickel framework while avoiding excessive zinc accumulation that could compromise the structural advantages of the foam architecture. In addition, the retained nickel fraction of 15.99% is particularly significant from both structural and electrochemical perspectives. This proportion ensures that the nickel foam maintains its mechanical integrity and continues to function as an effective current collector throughout the electrode volume.

Moreover, transmission electron microscopy analysis was utilized to verify the structure and interface quality by resolving the zinc coating at nanoscale resolution in Fig. 4. Concretely, Figs. 4(a)-(b) show TEM images of Zn4, which exhibits a lamellar structure. In Fig. 4(c), the lattice spacings of 0.250 nm and 0.204 nm correspond to the Zn(002) and Ni(111) planes, respectively, indicating that Zn was successfully electroplated onto the Ni substrate, consistent with the XRD and EDS results.

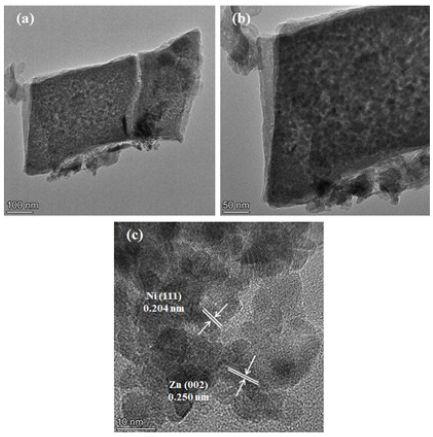

Fig. 4. TEM images of sample electrodeposited for 4 hours and its interplanar spacing; (a)-(b) TEM images of zinc in Zn4, (c) HRTEM image of Zn4.

Figs. 4(a)-(b) show TEM images of Zn4, which exhibits a lamellar structure. In Fig. 4(c), the lattice spacings of 0.250 nm and 0.204 nm correspond to the Zn (002) and Ni (111) planes, respectively, indicating that Zn was successfully electroplated onto the Ni substrate, consistent with the XRD and EDS results.

To assess surface composition and chemical states with the aim of verifying coating quality and establishing a baseline for structure-property correlation, comprehensive high-resolution X-ray photoelectron spectroscopy (XPS) was conducted on the zinc-coated nickel foam, as detailed in Fig. 5.

Fig. 5(a) presents the high-resolution Zn2 p spectra, where Zn3, Zn4, and Zn5 exhibit characteristic peaks near 1022.4 eV and 1045.4 eV , corresponding to $Zn2p_{3/2}$ and $Zn2p_{1/2}$, respectively, indicating that zinc is in the zero-valent state. In Fig. 5(b), the high-resolution O 1s spectra shows characteristic peaks near 531.8 eV for Zn3, Zn4, and Zn5 , corresponding to adsorbed oxygen, further suggesting that zinc remains in a good metallic state during preparation.

3.2. Influence of Deposition Time on Electrochemical Performance and Mechanism Analysis

To systematically investigate the effect of electrodeposition time on zinc loading and electrode structure, the mass of all samples before and after electrodeposition was measured, as shown in Table S1. Additionally, the thickness of the electrodeposited samples was measured, as illustrated in Figure S1. In Table S1, the average thicknesses of the samples were calculated to be 0.8 mm, 0.93 mm, and 1.0 mm , respectively. These results indicate a monotonic increase in both the mass and thickness of the samples with increasing electrodeposition time, suggesting that longer deposition times facilitate the deposition of more zinc onto the nickel foam substrate, thereby enhancing the zinc loading and electrode volume.

Fig. 6 shows the impedance curves of the three samples in a 6 mol/LKOH solution at room temperature. The corrosion of the electrode in the electrolyte is divided into two parts. The high-frequency region corresponds to the loss of electrons from zinc, forming ZnO_2^{2-} or $Zn(OH)4^{2-}$, while the low-frequency region represents the diffusion of ZnO_2^{2-} or $Zn(OH)4^{2-}$ from the electrode surface into the electrolyte solution. The EIS results indicate that all three samples exhibit similar charge transfer impedances, but Zn4 shows the lowest internal resistance (0.55Ω), suggesting better electrochemical kinetics.

Performance evaluation of the zinc-air batteries encompassed two aspects: open-circuit voltage and load performance. First, the open-circuit voltage variations of StZnB, Zn3B, Zn4B, and Zn5B were measured over 6 hours using an open-circuit test. A data logger was connected directly to the two terminals of the tested batteries to record voltage in real time and transmit the data to a computer for processing and plotting. The specific testing scheme and implementation are shown in Fig. S2.

The open-circuit voltage test scheme and setup are

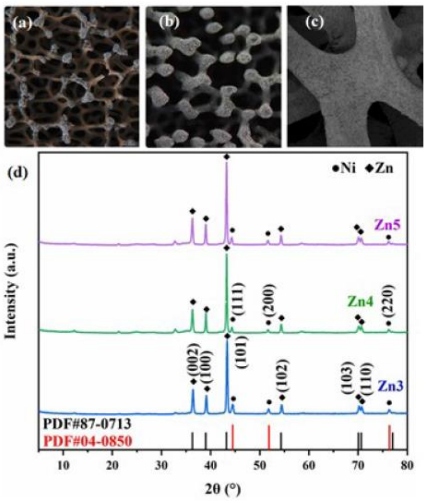

Fig. 2. Results of zinc electrodeposition on nickel foam; (a) Magnified image after 1 hour of electrodeposition, (b) Magnified image after 4 hours of electrodeposition, (c) SEM image of Zn4, (d) XRD patterns of Zn3, Zn4, and Zn5

Fig. 2(d) shows the XRD patterns of the samples with 3 h, 4 h , and 5 h of plating. Characteristic peaks appear at 36.4°, 39.1°, 43.4°, 54.4°, 70.2°, and 70.6°, corresponding to the Zn (002), (100), (101), (102), (103), and (110) planes (PDF#87-0713). Diffraction peaks related to the Ni (111), (200), and (220) planes are also observed at 44.5°, 51.2°, and 76.3° (PDF#04-0850). No characteristic peaks of ZnO are detected, indicating that zinc remains in a good metallic state during preparation.

In addition, the Energy Dispersive Spectroscopy analysis validates the electrodeposition methodology by providing quantitative evidence of zinc distribution uniformity and coverage on the three-dimensional nickel foam substrate. Elemental mapping confirms successful material integration while maintaining the structural integrity of the underlying nickel framework. The spatial analysis reveals comprehensive zinc penetration throughout the internal pore network and complete surface coverage across all accessible substrate areas, establishing the correlation between processing parameters and resulting electrode architecture that influences electrochemical performance, as demonstrated in Fig. 3.

Fig. 3 shows the EDS elemental distribution maps of the 4-hours electrodeposited sample. Fig. 3(a) is an overlay of

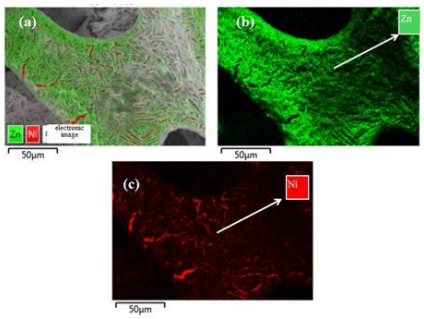

Fig. 3. EDS image of sample electrodeposited for 4 hours; (a) EDS overlay image, (b) EDS map of zinc, (c) EDS map of nickel

the SEM morphology and elemental maps. Fig. 3(b) shows the distribution of zinc, indicating a uniform distribution over the nickel foam framework. Fig. 3(c) presents the distribution of nickel, mainly concentrated in the substrate framework. Fig. 3 discloses that zinc has been successfully deposited onto the nickel foam surface with a uniform distribution.

Furthermore, the energy-dispersive X-ray spectroscopy analysis establishes quantitative baselines for the Zn4 sample by determining mass fractions of the electrodeposited layer. The technique quantifies zinc and nickel mass fractions, enabling precise evaluation of electrodeposition effectiveness, as illustrated in Table 1.

Table 1. Mass fractions of elements in Zn4

Total distribution map of spectrograms			
Element	Signal type	Wt%	Wt% Sigma
Ni	EDS	15.99	0.12
Zn	EDS	84.01	0.12
Total		100.00	

The quantitative elemental analysis presented in Table 1 provides crucial validation of the electrodeposition methodology and offers significant insights into the composite electrode architecture achieved in the Zn4 sample. The EDS results reveal a well-balanced composition with zinc constituting 84.01% and nickel comprising 15.99% of the total mass fraction, demonstrating successful zinc deposition while maintaining substantial nickel foam substrate integrity. The relatively high zinc content of 84.01% indicates that the electrodeposition process achieved substantial zinc loading on the nickel foam substrate, which is essential for maximizing the active material content and,

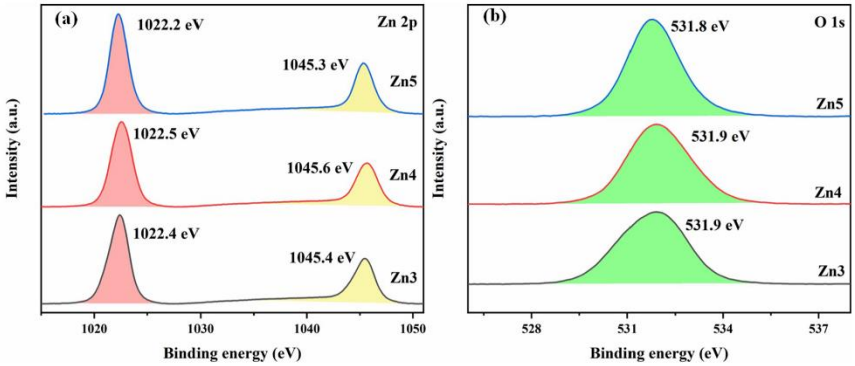

Fig. 5. XPS spectra of samples; (a) High-resolution Zn2p spectra, (b) High-resolution O 1s spectra.

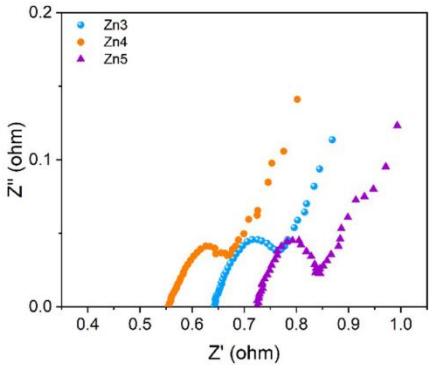

Fig. 6. EIS spectra of the samples.

shown in Figs. S2(a) and S2(b). Subsequently, by connecting the tested batteries to an LED load, the variations in load voltage and load current over 6 hours were measured. The data logger recorded voltage and current separately and plotted the corresponding curves. The load test scheme and setup are shown in Figs. S2(c) and S2(d).

After each battery group was tested, the datasets were gathered, organized, and subjected to routine post-processing to improve clarity and interpretability. Records were checked for consistency, artifacts mitigated, and traces formatted uniformly. From these harmonized data, performance-comparison curves were generated to summarize outcomes and highlight trends, as shown in Fig. 7.

The test results are shown in Figs. 7(a)-(c). As seen in Fig. 7(a), the initial open-circuit voltages of all tested batteries exceed 1.37 V , among which Zn4 B exhibits the highest value at 1.396 V, while the pure zinc plate battery StZnB shows a relatively lower open-circuit voltage. After 6 hours, Zn3 B shows the most pronounced decrease in open-circuit voltage, which can be attributed to that Zn3 sample has a smaller amount of deposited zinc. Spontaneous anode reactions increase internal resistance, leading to a significant drop in open-circuit voltage. From the load voltage results in Fig. 7(b), all batteries exhibit a noticeable drop in initial voltage upon loading; however, Zn4 B maintains the highest voltage, and after 6 hours it still shows a clear advantage, with an average load voltage of 1.17 V . This may be attributed to the favorable electrodeposition in Zn4B: a uniformly distributed zinc layer without obvious dendrite formation. In contrast, Zn3 B may suffer from insufficient deposited zinc, accelerating reactions that further increase internal resistance and reduce output voltage. The load current results in Fig. 7(c) indicate that Zn5 B has the largest initial current, approximately 5.7 mA , however the current decreases sharply within the first hour. This may stem from the large amount of zinc deposited on the Zn5 surface; due to non-uniform deposition, dendrites may form internally during operation, hindering further reactions, increasing internal resistance, and ultimately causing the current to decline.

3.3. Correlation Between Micromorphology and Performance

Scanning electron microscopy analysis assesses surface morphology and coating uniformity through secondary-

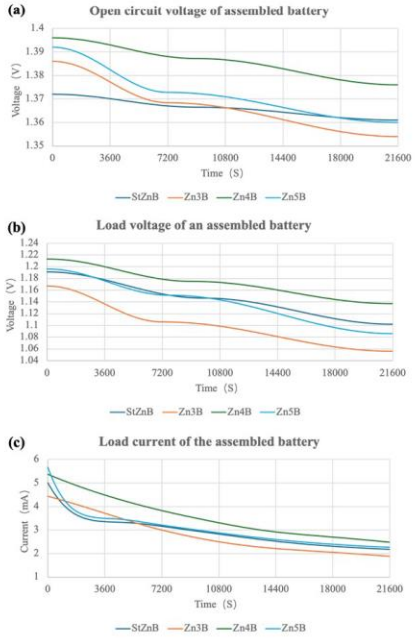

Fig. 7. Battery performance test results; (a) Open-circuit voltage of assembled batteries, (b) Load voltage of assembled batteries, (c) Load current of assembled batteries

electron imaging at multiple magnifications. Low-magnification views reveal pore architecture while high-magnification imaging characterizes grain features. Tilted and cross-sectional observations of ligament and junction regions evaluate zinc coverage continuity, thickness uniformity, and adhesion quality by identifying potential cracks, gaps, or delamination, as shown in Fig. 8.

Fig. 8 shows the surface micro morphologies of Zn3, Zn4, and Zn5 with different electrodeposition times, clearly revealing how deposition affects the performance of zinc-air batteries. Figs. 8(a)-(c) depict the surface morphology of Zn3 . Owing to the insufficient deposition time, a loose flocculent structure forms on the surface with limited reactive area, which may cause pronounced decreases in load voltage and current after cell assembly due to inadequate anode active material. Figs. 8(d)-(f) show the surface morphology of Zn4. With a moderate deposition time, a

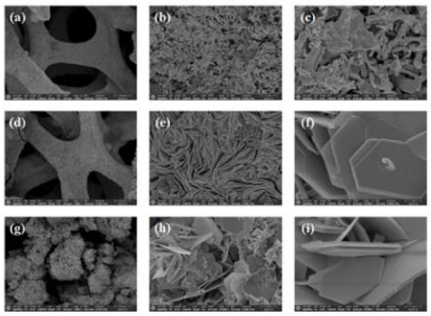

Fig. 8. SEM images of sample; (a)-(c) SEM images of Zn3 at $1,000\times$, $10,000\times$, and $50,000\times$, (d)-(f) SEM images of Zn4 at $1,000\times$, $10,000\times$, and $50,000\times$, (g)-(j) SEM images of Zn5 at $1,000\times$, $10,000\times$, and $50,000\times$

relatively uniform lamellar structure forms, which enlarges the electrochemical reaction area and provides sufficient active material, thereby yielding better stability in both load voltage and current. Figs. 8(g)-(j) present the surface morphology of Zn5. Due to the longer deposition time, more blocky aggregated structures form; these irregular blocks may impede ion transport during operation, hinder further electrochemical reactions, and thus degrade load voltage and current performance.

4. Conclusion

This work systematically elucidates how electrodeposition time influences the performance and underlying mechanism of zinc anodes on nickel foam. The experimental results reveal that the 4 hours deposited sample achieves the optimal balance between zinc loading (84.01wt%) and deposition uniformity, delivering the best overall performance with an average load voltage of 1.17 V , load current of 3.52 mA , and a 21% improvement over purezinc anodes. The superior performance arises from two synergistic factors: i) sufficient zinc deposition ensures ample reactive material, ii)moderate plating time promotes uniform zinc layers that suppress dendrite growth and optimize the reaction environment. We establish a multi-level "deposition time-zinc loading-microstructure-electrochemical performance" correlation model, providing a clear process window for zinc-air anode fabrication (recommended 4 h plating) and theoretical guidance, as well as methodological reference for other metal-air battery electrodes. Future work will focus on enhancing current output and further improving overall performance via electrolyte formulation

[21] R. Khezri, S. R. Motlagh, M. Etesami, P. Pakawanit, S. Olaru, A. Somwangthanaroj, and S. Kheawhom, (2024) *"Balancing current density and electrolyte flow for improved zinc-air battery cyclability"* **Applied Energy** ***376***: 124239. DOI: 10.1016/j.apenergy.2024.124239.

[22] T. Placke, R. Kloepsch, S. Dühnen, and M. Winter, (2017) *"Lithium ion, lithium metal, and alternative rechargeable battery technologies: the odyssey for high energy density"* **Journal of Solid State Electrochemistry** ***21***(7): 1939–1964. DOI: 10.1007/s10008-017-3610-7.

[23] J. F. Parker, C. N. Chervin, I. R. Pala, M. Machler, M. F. Burz, J. W. Long, and D. R. Rolison, (2017) *"Rechargeable nickel–3D zinc batteries: An energy-dense, safer alternative to lithium-ion"* **Science**: DOI: 10.1126/science.aak9991.

[24] M. Wang, F. Zhang, C.-S. Lee, and Y. Tang, (2017) *"Low-Cost Metallic Anode Materials for High Performance Rechargeable Batteries"* **Advanced Energy Materials** **7**(23): 1700536. DOI: 10.1002/aenm.201700536.

[25] J. Yi, P. Liang, X. Liu, K. Wu, Y. Liu, Y. Wang, Y. Xia, and J. Zhang, (2018) *"Challenges, mitigation strategies and perspectives in development of zinc-electrode materials and fabrication for rechargeable zinc–air batteries"* **Energy & Environmental Science** ***11***(11): 3075–3095. DOI: 10.1039/C8EE01991F.

[26] J. F. Parker, J. S. Ko, D. R. Rolison, and J. W. Long, (2018) *"Translating Materials-Level Performance into Device-Relevant Metrics for Zinc-Based Batteries"* **Joule** **2**(12): 2519–2527. DOI: 10.1016/j.joule.2018.11.007.

[27] D. E. Turney, J. W. Gallaway, G. G. Yadav, R. Ramirez, M. Nyce, S. Banerjee, Y.-c. K. Chen-Wiegart, J. Wang, M. J. D'Ambrose, S. Kolhekar, J. Huang, and X. Wei, (2017) *"Rechargeable Zinc Alkaline Anodes for Long-Cycle Energy Storage"* **Chemistry of Materials** **29**(11): 4819–4832. DOI: 10.1021/acs.chemmater.7b00754.

[28] J. Pan, Y. Y. Xu, H. Yang, Z. Dong, H. Liu, and B. Y. Xia, (2018) *"Advanced Architectures and Relatives of Air Electrodes in Zn–Air Batteries"* **Advanced Science** 5(4): 1700691. DOI: 10.1002/advs.201700691.

[29] K. Wang, Y. Zuo, P. Pei, X. Liu, M. Wei, Y. Xiao, J. Xiong, and P. Zhang, (2021) *"Zn–Ni reaction in the alkaline zinc-air battery using a nickel-supported air electrode"* **Materials Today Energy** ***21***: 100823. DOI: 10.1016/j.mtener.2021.100823.

[30] K. Wang, P. Pei, Y. Wang, C. Liao, W. Wang, and S. Huang, (2018) *"Advanced rechargeable zinc-air battery with parameter optimization"* **Applied Energy** 225: 848–856. DOI: 10.1016/j.apenergy.2018.05.071.

[31] Y.-P. Deng, Y. Jiang, R. Liang, S.-J. Zhang, D. Luo, Y. Hu, X. Wang, J.-T. Li, A. Yu, and Z. Chen, (2020) *"Dynamic electrocatalyst with current-driven oxyhydroxide shell for rechargeable zinc-air battery"* **Nature Communications** ***11***(1): 1952. DOI: 10.1038/s41467-020-15853-1.

[32] H. Pan, Y. Shao, P. Yan, Y. Cheng, K. S. Han, Z. Nie, C. Wang, J. Yang, X. Li, P. Bhattacharya, K. T. Mueller, and J. Liu, (2016) *"Reversible aqueous zinc/manganese oxide energy storage from conversion reactions"* **Nature Energy** ***1***(5): 16039. DOI: 10.1038/nenergy.2016.39.

optimization and stresscontrol strategies.

Acknowledgements

This research has received funding and support from the Silpakorn University Research, Innovation, and Creative Fund.

References

[1] H. S. Hayajneh and X. Zhang, (2020) *"Logistics Design for Mobile Battery Energy Storage Systems"* **Energies** ***13***(5): 1157. DOI: 10.3390/en13051157.

[2] Z. Zhu, T. Jiang, M. Ali, Y. Meng, Y. Jin, Y. Cui, and W. Chen, (2022) *"Rechargeable Batteries for Grid Scale Energy Storage"* **Chemical Reviews** ***122***(22): 16610–16751. DOI: 10.1021/acs.chemrev.2c00289.

[3] R.-B. Huang, M.-Y. Wang, J.-F. Xiong, H. Zhang, J.-H. Tian, and J.-F. Li, (2025) *"Anode optimization strategies for zinc–air batteries"* **eScience** *5*(3): 100309. DOI: 10.1016/j.esci.2024.100309.

[4] J. Fu, Z. P. Cano, M. G. Park, A. Yu, M. Fowler, and Z. Chen, (2017) *"Electrically Rechargeable Zinc-Air Batteries: Progress, Challenges, and Perspectives"* **Advanced Materials** *29*(7): 1604685. DOI: 10.1002/adma.201604685.

[5] R. Khezri, S. Rezaei Motlagh, M. Etesami, A. A. Mohamad, F. Mahlendorf, A. Somwangthanaroj, and S. Kheawhom, (2022) *"Stabilizing zinc anodes for different configurations of rechargeable zinc-air batteries"* **Chemical Engineering Journal** ***449***: DOI: 10.1016/j.cej.2022.137796.

[6] J. B. Goodenough and K.-S. Park, (2013) *"The Li-Ion Rechargeable Battery: A Perspective"* **Journal of the American Chemical Society** ***135***(4): 1167–1176. DOI: 10.1021/ja3091438.

[7] J. Zhang, Q. Zhou, Y. Tang, L. Zhang, and Y. Li, (2019) *"Zinc–air batteries: are they ready for prime time?"* **Chemical Science** ***10***(39): 8924–8929. DOI: 10.1039/C9SC04221K.

[8] N. Nitta, F. Wu, J. T. Lee, and G. Yushin, (2015) *"Li-ion battery materials: present and future"* **Materials Today** ***18***(5): 252–264. DOI: 10.1016/j.mattod.2014.10.040.

[9] M. Winter, B. Barnett, and K. Xu, (2018) *"Before Li Ion Batteries"* **Chemical Reviews** ***118***(23): 11433–11456. DOI: 10.1021/acs.chemrev.8b00422.

[10] M. Li, J. Lu, Z. Chen, and K. Amine, (2018) *"30 Years of Lithium-Ion Batteries"* **Advanced Materials** ***30***(33): 1800561. DOI: 10.1002/adma.201800561.

[11] P. Gu, M. Zheng, Q. Zhao, X. Xiao, H. Xue, and H. Pang, (2017) *"Rechargeable zinc–air batteries: a promising way to green energy"* **Journal of Materials Chemistry A** *5*(17): 7651–7666. DOI: 10.1039/C7TA01693J.

[12] C. Shunhong, S. Pullteap, and T. Mao, (2024) *"Research Progress and Future Expectations in Anode of Secondary Zinc-Air Batteries: A Review"* **Applied Science and Engineering Progress**: DOI: 10.14416/j.asep.2024.06.006.

[13] L. Li, Y. C. A. Tsang, D. Xiao, G. Zhu, C. Zhi, and Q. Chen, (2022) *"Phase-transition tailored nanoporous zinc metal electrodes for rechargeable alkaline zinc-nickel oxide hydroxide and zinc-air batteries"* **Nature Communications** ***13***(1): 2870. DOI: 10.1038/s41467-022-30616-w.

[14] K. Harting, U. Kunz, and T. Turek, (2012) *"Zinc-air Batteries: Prospects and Challenges for Future Improvement"* **Zeitschrift für Physikalische Chemie** *226*(2): 151–166. DOI: 10.1524/zpch.2012.0152.

[15] X. Chen, Z. Zhou, H. E. Karahan, Q. Shao, L. Wei, and Y. Chen, (2018) *"Recent Advances in Materials and Design of Electrochemically Rechargeable Zinc–Air Batteries"* **Small** ***14***(44): 1801929. DOI: 10.1002/smll.201801929.

[16] O. Haas, F. Holzer, K. Müller, and S. Müller. "Metal/air batteries: the zinc/air case". en. In: *Handbook of Fuel Cells*. 2010. DOI: 10.1002/9780470974001.f104022.

[17] E. Davari, A. D. Johnson, A. Mittal, M. Xiong, and D. G. Ivey, (2016) *"Manganese-cobalt mixed oxide film as a bifunctional catalyst for rechargeable zinc-air batteries"* **Electrochimica Acta** ***211***: 735–743. DOI: 10.1016/j.electacta.2016.06.085.

[18] D. Liu, Y. Tong, X. Yan, J. Liang, and S. X. Dou, (2019) *"Recent Advances in Carbon-Based Bifunctional Oxygen Catalysts for Zinc-Air Batteries"* **Batteries & Supercaps** *2*(9): 743–765. DOI: 10.1002/batt.201900052.

[19] M. Wu, G. Zhang, Y. Hu, J. Wang, T. Sun, T. Regier, J. Qiao, and S. Sun, (2021) *"Graphitic-shell encapsulated FeNi alloy/nitride nanocrystals on biomass-derived N-doped carbon as an efficient electrocatalyst for rechargeable Zn-air battery"* **Carbon Energy** *3*(1): 176–187. DOI: 10.1002/cey2.52.

[20] J. Ding, P. Wang, S. Ji, H. Wang, V. Linkov, and R. Wang, (2019) *"N-doped mesoporous FeNx/carbon as ORR and OER bifunctional electrocatalyst for rechargeable zinc-air batteries"* **Electrochimica Acta** *296*: 653–661. DOI: 10.1016/j.electacta.2018.11.105.

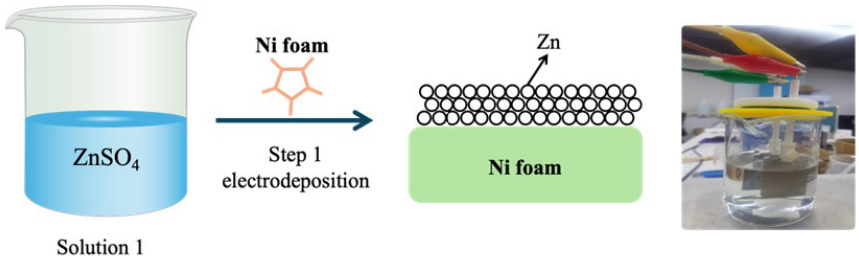

Fig. 1. Schematic illustration of electrodeposition process of zinc on nickel foam

Zn3 B, Zn4 B, and Zn5 B , respectively. Meanwhile, a pure zinc plate (35 × 60 mm, 2 mm thick) was used as a control anode, with all other components unchanged, to assemble a standard zinc-air battery for comparison, designated StZnB . After assembly, all batteries were allowed to stand for 10 min to ensure full electrolyte infiltration and stabilization of the electrode/electrolyte interface before performance testing.

2.5. Physical Characterization and Electrochemical Performance Testing

The phase composition and crystal structure of the zinc coating were characterized by X ray diffraction (XRD, Rigaku Ultima IV) using Cu Kα radiation ($\lambda = 1.5406$ Å), with a scanning range of 5° – 80° and a scan rate of 8°/min. A scanning electron microscope (SEM, Thermo Scientific Apreo2) equipped with an energy-dispersive X-ray spectrometer (EDS) and a transmission electron microscope (TEM, Talos F200S) were used to examine the micromorphology and elemental distribution of the zinc coating, operated at 5 kV accelerating voltage and 50 pA beam current. X-ray photoelectron spectroscopy (XPS, Thermo Scientific K-Alpha) was employed to analyze the valence states of surface elements, with all binding energies calibrated to the C 1s peak (adventitious carbon on the sample surface) at 284.8 eV . Electrochemical performance was evaluated using a digital multimeter and a data acquisition system to measure the open-circuit voltage, load voltage, and load current of both the control cell with a pure zinc plate anode and the zinc-plated nickel foam anode cells. Voltage decay and current fluctuations were continuously recorded over 6 hours, with a light-emitting diode (LED) serving as the external load.

3. Results and discussion

3.1. Physical Characterization

To provide a clear understanding of the experimental methodology and to visually present the basic preparation process of the zinc anode, a schematic diagram of the electrochemical deposition process is shown in Fig. 1. This diagram offers the necessary background for the system approach used in this study. Uniform zinc-coated nickel foam composites were successfully fabricated through electrochemical deposition, with zinc evenly deposited onto the three-dimensional porous nickel foam structure, exhibiting strong adhesion.

To demonstrate the temporal evolution and effectiveness of zinc electrodeposition on nickel foam substrates, systematic documentation of morphological transformations throughout different deposition stages establishes the correlation between processing parameters and electrode architecture, as illustrated in Fig. 2.

The morphologies of the Zn serial samples are observed by SEM as showed in Fig. 2a-c. Obviously, the morphology of nickel foam after 1 hour of electrodeposition (Fig. 2(a)), exhibits that there a small amount of zinc was deposited initially at the tips and edges of the nickel foam. Fig. 2(b) shows that after 4 hours of electrodeposition, a large amount of zinc is uniformly deposited on the nickel foam framework, forming a continuous layer that fully covers the surface, demonstrating the effectiveness of the deposition process. Fig. 2(c) presents an SEM image of the 4-hour electrodeposited sample, where the zinc layer is observed to adhere relatively uniformly to the nickel foam surface, forming a comparatively dense coating. This indicates that under optimized electrodeposition conditions, the deposited zinc layer can effectively suppress the formation of large particles, which is beneficial for the subsequent performance of zinc-air batteries.

VITA

NAME Chen Shunhong

PUBLICATION

C. Shunhong, S. Pullteap, and T. Mao, (2024) “Research Progress and Future Expectations in Anode of Secondary Zinc-Air Batteries: A Review" Applied Science and Engineering Progress: DOI: 10.14416/j .asep. 2024.06.006.

C. Shunhong, T. Hudakorn, and S. Pullteap, (2026) Electrodeposited Zinc Anodes On Nickel Foam For Enhanced Zinc-Air Battery Performance. Journal of Applied Science and Engineering 29 : 1239–1247 . DOI: 10.6180/jase.202605_29(5).0019